



HAL
open science

Secondary microseisme Love wave generation

Shipra Sethi

► **To cite this version:**

Shipra Sethi. Secondary microseisme Love wave generation. Earth Sciences. Université Paris Cité, 2019. English. NNT: 2019UNIP7164 . tel-03139966

HAL Id: tel-03139966

<https://theses.hal.science/tel-03139966v1>

Submitted on 12 Feb 2021

HAL is a multi-disciplinary open access archive for the deposit and dissemination of scientific research documents, whether they are published or not. The documents may come from teaching and research institutions in France or abroad, or from public or private research centers.

L'archive ouverte pluridisciplinaire **HAL**, est destinée au dépôt et à la diffusion de documents scientifiques de niveau recherche, publiés ou non, émanant des établissements d'enseignement et de recherche français ou étrangers, des laboratoires publics ou privés.

UNIVERSITÉ DE PARIS



université
PARIS
DIDEROT
PARIS 7



École Doctorale STEP'UP – ED 560
Institut de Physique du Globe de Paris – Équipe de Sismologie

Secondary microseism Love wave generation

par
Shipra Sethi

Thèse de doctorat de Sciences de la Terre et de l'Environnement

dirigée par Eléonore Stutzmann
et par Yann Capdeville

présentée et soutenue publiquement le
22 novembre 2019

devant un jury composé de

Heiner Igel	Professeur (LMU Munich, Munich, Allemagne)	Rapporteur
Eric Beucler	Professeur (Université de Nantes, France)	Rapporteur
Jean-Paul Montagner	Professeur (IPGP, Paris, France)	Examineur
Mickaël Bonnin	Physicien (Université de Nantes, France)	Examineur

Résumé

Le bruit sismique est l'oscillation continue de la Terre enregistrée à chaque station en l'absence de tremblement de terre. Il résulte de l'interaction entre l'atmosphère, les océans et la terre solide. Le signal dominant, appelé microséismes secondaires dans la bande de fréquences 0,1-0,3 Hz, a pour origine l'interaction non linéaire entre des ondes de gravité océaniques de même fréquence et de directions opposées. Les fluctuations de pression qui en résultent près de la surface de l'océan génèrent un signal sismique. Le signal dominant est constitué d'ondes de Rayleigh (R). Plusieurs études montrent également l'existence d'ondes de Love (L) mais le rapport d'amplitude L/R entre les ondes de Love et de Rayleigh varie en fonction de la zone étudiée. Le mécanisme de génération des ondes de Rayleigh dues à l'interaction de ces sources de bruit avec le fond marin est bien compris et modélisé. Cependant, le mécanisme de génération des ondes de Love reste mystérieux car une source dans l'océan ne peut pas générer de mouvement de cisaillement. Dans ce travail, nous montrons l'existence d'ondes de Rayleigh et Love enregistrées par le réseau de l'Alaska et de la Californie. Nous étudions ensuite l'effet de la pente océan-continentale sur l'amplitude du bruit sismique des microséismes secondaires et quantifions la conversion des ondes de Rayleigh et de Love. Pour ce faire, nous utilisons la méthode des éléments spectraux pour simuler numériquement le champ d'ondes sismiques dans les milieux 3D. L'objectif est de déterminer les facteurs qui ont une influence sur l'amplitude des ondes de Love enregistrées sur le continent dans la bande de fréquences 0,1-1 Hz. Ces facteurs sont a) l'épaisseur de l'océan, b) l'effet de site à la source, c) la présence d'une couche sédimentaire sous le fond océanique et d) l'angle de la pente océan-continent. Nous observons que des ondes de Love peuvent être générées à la frontière océan-continentale, et que la variation de leur amplitude dépend de la fréquence. La plus forte amplitude des ondes de Love est enregistrée dans un modèle avec 6 km d'océan, 6 km de croûte et 10 km de manteau à des fréquences de résonance dans l'océan lorsque la source est loin de la côte. Cependant, à d'autres fréquences, les océans peu profonds et les sources proches de la frontière de la océan-continent génèrent des ondes de Love d'amplitude maximale. En présence de sédiments, l'amplification de Love est plus élevée à des périodes plus courtes pour les deux sources. La réduction de l'angle de pente diminue l'amplitude de l'onde de Love. Pour les sources proches et éloignées de la frontière océan-continent, le rapport d'amplitude L/R varie fortement selon la fréquence et l'épaisseur de l'océan. Parmi tous les facteurs, les rapports d'amplitude L/R les plus élevés sont générés dans les sédiments lorsque la source est proche de la frontière.

Summary

Seismic noise is the continuous oscillation of the Earth recorded at every station in the absence of earthquakes. The interaction of atmosphere, ocean waves and earth creates them. The dominant signal, called secondary microseisms in the frequency band 0.1-0.3 Hz have known to be formed due to the non-linear interaction between two oppositely traveling ocean gravity waves. The resulting pressure fluctuations close to the ocean surface generates a seismic signal which is dominantly Rayleigh waves (R). Many authors reported the observations of Love wave content (L) in the seismic signal. However the L/R amplitude ratio is shown to vary depending on the area investigated. The generation mechanism of Rayleigh waves due to these noise sources interacting with the sea-bottom is well understood and modeled. The explanation why Love waves are generated is unclear because the source in the ocean cannot generate shear motion. We have shown the existence of Rayleigh and Love waves recorded by the Alaska and California network. We then investigate the effect of ocean-continental slope boundary on the seismic noise amplitude of secondary microseism and quantify the Rayleigh-to-Love wave conversion. In order to do that, we use the spectral element method to numerically simulate the seismic wave field in 3D media. The primary focus of this study is on investigating several factors that can influence the seismic noise amplitude recorded on the continent in the frequency band 0.1-1 Hz. Those factors are a) the ocean-thickness, b) the source-site effect i.e., source close to the boundary and far from the boundary, c) the sedimentary layer beneath the sea-bottom and d) the effect of ocean-continental slope angle. We observe that Love waves can be generated at the ocean-continental boundary, however the amplitude change is frequency dependent. We observe energy in the transverse direction in a model that cannot generate Love waves as a result of conversion at the ocean-continental slope boundary. The strongest Love wave amplitude is recorded in a model with 6 km deep ocean at resonant frequencies in the ocean when the source is far from the coast. However at other frequencies, shallow oceans and source close to the boundary generates highest Love wave amplitude. In the presence of sediments, the amplification of Love waves is higher at shorter periods for both sources. The reduction in slope angle diminishes the Love wave amplitude. For both source close and far from the boundary, the L/R amplitude ratio vary strongly with frequency and ocean thickness. Among all the factors, highest L/R amplitude ratios are generated due to sediments when the source is close to the boundary.

Contents

Résumé	4
Summary	6
Table of Contents	8
List of figures	12
1 Introduction	13
1.1 Seismic Noise	14
1.2 Brief introduction to Secondary Microseisms	15
1.3 Behavior of microseisms	17
1.4 Observation of Love waves	19
1.5 Methodology	22
1.5.1 Spectral Element method	22
1.5.2 Mesh generation	29
1.5.3 Green's function	30
1.5.4 Computation of Rotational component	30
1.5.5 Calculation of slope at the ocean-continental boundary	31
2 Data Analysis	35
2.1 Observations of Love waves in Data	36
2.2 Data and Methodology	36
2.2.1 Data	36
2.2.2 Beamforming	36
2.3 Results and Discussion	37
3 1D Synthetic Seismograms using Hermann's Code	43
3.1 Group and phase velocities for 1-D Earth models	44
3.1.1 Oceanic model: 1 km ocean and 16 km crust & Continental model: 17 km crust	44
3.1.2 Oceanic model: 1 km ocean, 6 km crust and 10 km mantle & Continental model: 7 km crust and 10 km mantle	45
3.1.3 Oceanic model: 3 km ocean, 6 km crust and 10 km mantle & Continental model: 9 km crust and 10 km mantle	48
3.1.4 Oceanic model: 6 km ocean, 6 km crust and 10 km mantle & Continental model: 12 km crust and 10 km mantle	50
3.1.5 Oceanic model: 6 km ocean, 3 km sediments, 6 km crust and 7 km mantle	51

4	Modeling the effect of ocean-continental slope on Secondary microseisms	61
4.1	Effect of ocean thickness	62
4.1.1	Models Setup	62
4.1.2	Seismic wavefield for model I (1 km ocean, crust)	64
4.1.3	Seismic wavefield for model II (1 km ocean, crust and mantle)	72
4.1.4	Seismic wavefield for model III (3 km ocean, crust and mantle).....	80
4.1.5	Seismic wavefield for model IV (6 km ocean, crust and mantle)	82
4.2	Effect of sediments	85
4.2.1	Seismic wavefield for model V (6 km ocean, sediments, crust, mantle) .	85
4.3	Effect of the ocean-continent slope	91
4.3.1	Seismic wavefield for model VI (3 km ocean, crust, mantle) slope 10° ..	91
4.4	Results summary.....	95
5	Conclusions and future perspectives	101
	References	104

List of Figures

1.1	Station TAM power spectral density of seismic noise.....	15
1.2	Wave motion representation in 2D. \bar{P}_h is pressure variation at depth h . η is the second order surface elevation.....	16
1.3	Schematic of wave conditions in noise-generating situations.	18
1.4	Frequency–slowness spectra on the radial, transverse and vertical component. ...	20
1.5	Energy ratio of Love to Rayleigh waves as a function of frequency.	21
1.6	Comparison among the transverse acceleration from the rotation measurements (red), the vertical acceleration from STS-2, and the horizontal acceleration from the vertical acceleration plus theoretical surface ellipticity.....	22
1.7	Beamforming results for the three components using seismic array data in Pilbara for Z, R and T components at $f_1 = 0.35 \pm 0.0175$ Hz.	23
1.8	Azimuth variability of power ratio between Z and T components.....	24
1.9	Two realizations of a random medium with different correlation lengths.....	24
1.10	L/R ratio as a function of distance, for varying fluctuation strength σ	25
1.11	L/R ratio as a function of distance with varying correlation length a . (Ziane and Hadziioannou 2019)	25
1.12	L/R ratio as a function of distance for three models with varying layering types.	26
1.13	Topographic map of a) Japan b) Germany c) Australia showing the profiles according to which slopes were calculated (black lines) at each point.	33
1.14	Value of the slope (in percentage) calculated at each source point of the model using the topography data from ETOPO1.	34
1.15	Histogram showing the distribution of the slopes determined in figure 1.14.....	34
2.1	Observed beam PSD for the two-components using seismic noise array data showing the sources of Rayleigh waves on the vertical component and Love wave on the T component.....	38
2.2	Pressure PSD on 09 December 2014 for a period at (a) 3h and (b)9h respectively.	39
2.3	Pressure PSD on 09 December 2014 for a period at (a)18h and (b)mid night respectively.	40
2.4	Pressure PSD on 10 December 2014 for a period at (a) 9h and (b) 21h respectively.	41
3.1	Phase and group velocity for oceanic model: 1 km ocean and 16 km crust	44
3.2	Phase and group velocity for continent model: 17 km crust	45
3.3	Z and R component synthetic seismograms for oceanic model: 1 km ocean and 16 km crust	46

3.4	Phase and group velocity for oceanic model: 1 km ocean, 6 km crust and 10 km mantle	47
3.5	Phase and group velocity for continent model: 7 km crust and 10 km mantle ...	48
3.6	Z and R component synthetic seismograms for oceanic model: 1 km ocean, 6 km crust and 10 km mantle	49
3.7	Z and R component synthetic seismograms for continent model: 7 km crust and 10 km mantle	50
3.8	Phase and group velocity for the oceanic model: 3 km ocean, 6 km crust and 10 km mantle	51
3.9	Phase and group velocity for continent model: 9 km crust and 10 km mantle ...	52
3.10	Z and R component synthetic seismograms for the oceanic model 3 km ocean, 6 km crust and 10 km mantle	53
3.11	Z and R component synthetic seismograms for the continent model: 9 km crust and 10 km mantle	54
3.12	Phase and group velocity for the oceanic model: 6 km ocean, 6 km crust and 10 km mantle	55
3.13	Phase and group velocity for the continent model: 12 km crust and 10 km mantle	55
3.14	Z and R component synthetic seismograms for the oceanic model: 6 km ocean, 6 km crust and 10 km mantle	56
3.15	Z and R component synthetic seismograms for the continent model: 12 km ocean and 10 km mantle	57
3.16	Phase and group velocity for the oceanic model: 6 km ocean, 3 km sediments, 6 km crust and 7 km mantle	58
3.17	Z and R component synthetic seismograms for the oceanic model: 6 km ocean, 3 km sediments, 6 km crust and 7 km mantle	59
4.1	3D representation of the model I with 1 km ocean and 16 km crust on the oceanic side and 17 km crust on the continent side.	65
4.2	3D representation of the model II with 1 km ocean, 6 km crust and 10 km mantle on the oceanic side, 7 km crust and 10 km mantle on the continent side.	66
4.3	Three-component synthetic seismic velocity for model I and the source S2 located close to the ocean-continent boundary.	67
4.4	Particle motion in the Z-R plane.	68
4.5	Amplitude spectrum of the seismic velocity recorded at stations for model I.	69
4.6	Particle motion in the R-T plane for model I and source S2 close to the ocean-continent boundary in the frequency band 0.1-0.15 Hz.	69
4.7	Particle motion in the R-T plane for model I and source S2 close to the ocean-continent boundary in the frequency band 0.1-1 Hz.	70
4.8	Rayleigh vs SH/Love wave amplitude spectrum adjacent to vertical rotational rate * 2c (c: the local phase velocity computed as $v_{Tmax}/2\omega_{Zmax}$) fundamental Love wave velocity from 1-D synthetics) vs transverse velocity as a function of frequency in model I (1 km ocean, without mantle) and source close to the ocean-continent boundary	71
4.9	Three-component synthetic seismic velocity for model II and the source S2 located close to the ocean-continent boundary.	73

4.10	Amplitude spectrum of the seismic velocity recorded at stations for model II and source S2 close to the ocean-continent boundary.	74
4.11	Particle motion in the R-T plane for model II and source S2 close to the ocean-continent boundary in the frequency band 0.1-0.15 Hz.	74
4.12	Particle motion in the R-T plane for model II and source S2 close to the ocean-continent boundary in the frequency band 0.1-1 Hz.	75
4.13	Rayleigh vs SH/Love wave amplitude spectrum adjacent to vertical rotational rate * 2c (c: fundamental Love wave velocity from 1-D synthetics) vs transverse velocity as a function of frequency in model II (1 km ocean, with mantle) and source close to the ocean-continent boundary.	76
4.14	Three-component synthetic seismic velocity for model II and the source S1 located far from the ocean-continent boundary.	78
4.15	Amplitude spectrum of the seismic velocity recorded at stations for model II and source S1 far from the ocean-continent boundary.	79
4.16	Particle motion in the R-T plane for model II and source S1 far from the ocean-continent boundary in the frequency band 0.1-0.15 Hz.	79
4.17	Particle motion in the R-T plane for model II and source S1 far from the ocean-continent boundary in the frequency band 0.1-1 Hz.	80
4.18	Rayleigh vs SH/Love wave amplitude spectrum adjacent to vertical rotational rate * 2c (c: fundamental Love wave velocity from 1-D synthetics) vs transverse velocity as a function of frequency in model II (1 km ocean, with mantle) and source far from the ocean-continent boundary.	81
4.19	Rayleigh vs SH/Love wave amplitude spectrum adjacent to vertical rotational rate * 2c (c: fundamental Love wave velocity from 1-D synthetics) vs transverse seismic velocity as a function of frequency in model III (3 km ocean, with mantle) for a source close to the ocean-continent boundary.	83
4.20	Rayleigh vs SH/Love wave amplitude spectrum adjacent to vertical rotational rate * 2c (c: fundamental Love wave velocity from 1-D synthetics) vs transverse seismic velocity as a function of frequency in model III (3 km ocean, with mantle) for a source far-away from the ocean-continent boundary.	84
4.21	Rayleigh vs SH/Love wave amplitude spectrum adjacent to vertical rotational rate * 2c (c: fundamental Love wave velocity from 1-D synthetics) vs transverse velocity as a function of frequency in model IV (6 km ocean, with mantle) when the source is placed close to the boundary.	86
4.22	Rayleigh vs SH/Love wave amplitude spectrum adjacent to vertical rotational rate * 2c (c: fundamental Love wave velocity from 1-D synthetics) vs transverse velocity as a function in model IV (6 km ocean, with mantle) when the source is placed far-away from the boundary.	87
4.23	3D representation of the model with 6 km ocean, 3 km sediments, 6 km crust and 7 km mantle on the oceanic side, 15 km crust and 7 km mantle on the continent side.	88
4.24	Three-component synthetic seismic velocity for model V and the source S2 located close to the ocean-continent boundary.	89

4.25	Rayleigh vs SH/Love wave amplitude spectrum adjacent to vertical rotational rate * 2c (c: fundamental Love wave velocity from 1-D synthetics) vs transverse velocity as a function of frequency for model with 6 km ocean, 3 km sediments, 6 km crust and 7 km mantle (figure 3.24) with source close to the ocean-continent boundary.....	90
4.26	Three-component synthetic seismic velocity for model V and the source S1 far from the ocean-continent boundary.	92
4.27	Rayleigh vs SH/Love wave amplitude spectrum adjacent to vertical rotational rate * 2c (c: fundamental Love wave velocity from 1-D synthetics) vs transverse velocity as a function of frequency for model with 6 km ocean, 3 km sediments, 6 km crust and 7 km mantle (figure 3.24) with source far-away from the ocean-continent boundary.....	93
4.28	Three-component synthetic seismic velocity for model VI and the source S2 close to the ocean-continent boundary.	94
4.29	Rayleigh vs SH/Love wave amplitude spectrum adjacent to vertical rotational rate * 2c (c: fundamental Love wave velocity from 1-D synthetics) vs transverse velocity as a function of frequency in 3 km ocean model, slope 10° when the source is placed close to the boundary.	95
4.30	Rayleigh vs SH/Love wave amplitude spectrum adjacent to vertical rotational rate * 2c (c: fundamental Love wave velocity from 1-D synthetics) vs transverse velocity as a function of frequency for stations A, B, C, D, E & F in 3 km ocean model, slope 10° when the source is placed far from the boundary.	96
4.31	Rayleigh and Love wave amplitude as a function of frequency at station E obtained for source close to the ocean-continent boundary and far from it in the frequency band 0.1-1 Hz.	98
4.32	Rayleigh and Love wave amplitude as a function of frequency at station E for source close and far from the ocean-continent boundary in the frequency band 0.1-0.3 Hz.	99
4.33	Comparison of L/R ratio at station E for all the models without sediments for source both close and far from the ocean-continent boundary.....	100

Chapter 1

Introduction

1.1	Seismic Noise	14
1.2	Brief introduction to Secondary Microseisms	15
1.3	Behavior of microseisms	17
1.4	Observation of Love waves	19
1.5	Methodology	22
1.5.1	Spectral Element method	22
1.5.2	Mesh generation	29
1.5.3	Green's function	30
1.5.4	Computation of Rotational component	30
1.5.5	Calculation of slope at the ocean-continental boundary	31

A quick overview of the chapter In this chapter, we introduce the concepts of continuously recorded signals called, seismic noise and microseisms in section 1.1. The theory behind the origin of secondary microseisms that constitute the large part of seismic noise signal is briefly introduced in section 1.2. The seismic signal generated is mostly recorded as Rayleigh waves but many evidences showing the propagation of Love waves are present. In section 1.3, we start by giving an overview of the history of observation of Love waves to understand the context of this study. Section 1.5 is entirely focused on describing elaborately the methods applied during the execution of this thesis. We first discuss how can we use spectral element method to determine seismic wave field propagation in detail. Section 1.4 is dedicated to describe the method and the necessary steps for the execution of method are included in sections 1.5.2 and 1.5.3. One of the methods that is useful for interpretation of seismic wave field is computation of rotational component that helps in distinguishing the Love wave component in the wave field is discussed in section 1.5.4. Lastly, since our study focuses on measuring the effect of ocean-continental slope on the amplitude of seismic wave field, we compute the different slopes using ocean topography in section 1.5.5.

1.1 Seismic Noise

What does a seismograph record? Earthquake signal contaminated with some background noise that is not useful. Years of intensive study and development of new techniques opened a new sphere of research in which noise has a significant role in exploring the internal structure of the Earth ([Shapiro et al. \(2005\)](#), [Nishida et al. \(2009\)](#), [Schimmel et al. \(2011\)](#)) and also in various other applications. Seismic noise, generally termed as microseisms is an omnipresent signal recorded by the seismometers even in the absence of an earthquake activity. Microseisms are the continuous oscillations of the ground within the frequency band of 0.05 Hz and 1 Hz, produced by the interaction of atmosphere, ocean waves and the Earth. Storms, ocean waves and microseisms have well-established correlation ([Gutenberg \(1931\)](#), [Bernard and Martel \(1990\)](#)). Seismic spectra shows two major peaks centered at 0.07 Hz and 0.14 Hz s, which are denoted as the primary and secondary microseisms respectively. To understand the nature of the spectra and their origin, the sources have been tremendously studied and numerous papers have succeeded in explaining their generation mechanism ([Longuet-Higgins \(1950\)](#), [Hasselmann \(1963\)](#), [Haubrich et al. \(1963\)](#))

Let's take an example of the seismic noise spectra recorded at one station from the GEO-SCOPE network ([Stutzmann et al. 2000](#)).

Figure 1.1 shows the power spectral density estimated at station TAM for the three components: vertical, north–south, and east–west as a function of period [[Stutzmann et. al 2000](#)]. We clearly observe the dominance of the two characteristic peaks of the seismic noise, namely primary and secondary microseisms ([Webb 1998](#)), . Primary microseisms originate due to coupling of ocean wave at the shallow ocean bottom and have the same frequency as the ocean waves ([Hasselmann 1963](#)). Secondary microseisms are the result of non-linear interaction of two ocean waves traveling in the opposite direction [[Longuet-Higgins \(1950\)](#), [Hasselmann \(1963\)](#), [Kedar et al. \(2008\)](#), [Ardhuin et al. \(2011\)](#), [Gerstoft](#)

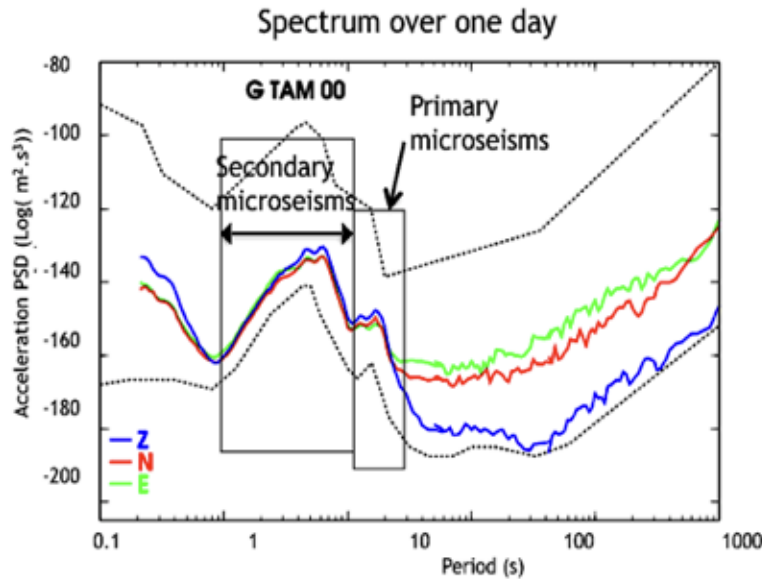


Figure 1.1 – Station TAM power spectral density of seismic noise estimated over data from one day for the three components, vertical (Z) in blue solid line, north–south (N) in red, and east–west (E) in green. [Source: Stutzmann et al. (2000)]

and Tanimoto (2007), Bromirski (2002), Bromirski (2009)]. The resulting pressure fluctuates with twice the frequency of ocean waves, hence called double-frequency. For periods $20 \text{ s} < T < 100 \text{ s}$, seismic hum dominates the power spectra. The conversion of oceanic infragravity waves that interact with shallow to intermediate depth seafloor topography generates hum [Nawa et al. (1998), Suda et al. (1998), Tanimoto et al. (1998), Rhie and Romanowicz (2004), Ardhuin et al. (2015), Nishida (2013), Nishida (2014)].

1.2 Brief introduction to Secondary Microseisms

When the microseisms first were studied, several authors attempted to explain its cause which were proved insufficient. For instance, Gherzi (1932) proposed microseisms were caused by pumping of the atmosphere similar to what is sometimes observed on a barograph near the center of intense tropical cyclone. Scholte (1943) demonstrated that microseisms may be generated by oscillating atmospheric pressure on the surface of the sea and that the amplitude of the compression waves is as great as 10^{-4} times the amplitude of the gravity waves. Gutenberg (1958) proposed that microseisms were caused by the impact of waves breaking against a steep coast, which was later proved one plausible mechanism with certain limitations on the reflected energy. When secondary microseisms were proposed to originate due to the pressure variation in the ocean, it was well-doubted because of two observed phenomena 1. the exponential decay of pressure variation due to ocean waves with depth, and 2. the double-frequency of the microseisms. However, it was not until Miche (1944) discovered that the pressure variation fluctuates with an amplitude independent of depth, the theory could explain the generation mechanism, which was later shown by Longuet-Higgins (1950).

Let us look at the equations governing ocean wave-wave interaction, leading to generation of microseisms (Longuet-Higgins (1950), Hasselmann (1963)); Mangeney, PhD course 2012; Farra, PhD course 2014; Stutzmann, TIDE workshop course, 2016). The particle motion in the fluid is described by the Euler equation:

$$\rho \left[\frac{\partial \vec{u}}{\partial t} + (\vec{u} \cdot \vec{\nabla}) \vec{u} \right] = -\vec{\nabla} P + \rho \vec{g} \quad (1.1)$$

where ρ is the density, t the time, \vec{u} the fluid particle velocity, P the pressure, g the acceleration of gravity. Considering the expansion to the second order, the position of the sea surface elevation is represented as $\eta = \eta_0 + \epsilon \eta_1 + \epsilon^2 \eta_2$ (as shown in figure 1.2), fluid particle velocity $\vec{u} = \vec{u}_0 + \epsilon \vec{u}_1 + \epsilon^2 \vec{u}_2$ and pressure $P = P_0 + \epsilon P_1 + \epsilon^2 P_2$, where ϵ is a small number. For an in-compressible fluid, we write the first order fluid velocity (u_1, u_{1z}) as

$$(u_{1x}, u_{1z}) = \left(-\frac{\partial \phi_1}{\partial x}, -\frac{\partial \phi_1}{\partial z} \right) \quad (1.2)$$

where ϕ_1 is the first order velocity potential, We then make the assumptions that η_1 and ϕ_1 are represented by the forms, $\eta_1 = a \cos(k.x - \omega t)$ and $\phi_1 = b(z) \cos(k.x - \omega t)$

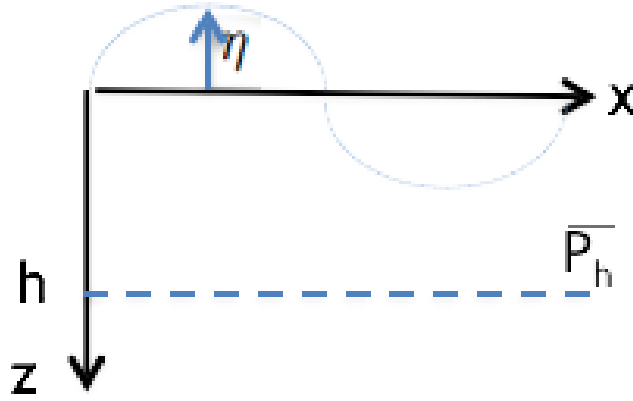


Figure 1.2 – Wave motion representation in 2D. \bar{P}_h is pressure variation at depth h . η is the second order surface elevation.

Considering the boundary condition at the ocean bottom h and at the free surface and eqn 1.1, we get the dispersion relation :

$$\omega^2 = gk \tanh(kh) \quad (1.3)$$

In case of deep water, we obtain

$$\begin{aligned} \omega^2 &= gk \\ \phi_1 &= \sqrt{\frac{g}{k}} a e^{-kz} \sin(k.x - \omega t) \\ u_{1x} &= -a \omega e^{-kz} \cos(k.x - \omega t) \\ u_{1z} &= -a \omega e^{-kz} \sin(k.x - \omega t) \end{aligned}$$

Now, if the second order surface elevation and particle velocity is considered, equation of motion takes the form,

$$\frac{\bar{P}_2 - P_a}{\rho} - gz = \frac{1}{\lambda} \frac{\partial^2}{\partial t^2} \int_0^\lambda \frac{1}{2} \eta^2 dx \quad (1.4)$$

where P_a is the atmospheric pressure, $\overline{P_2}$ is the mean pressure over one wavelength λ . Extending this further to a special case of wave motion, considering two progressive waves of equal wavelength λ and period T traveling in opposite directions, the sea surface elevation is the sum of the two waves: $\eta = a_1 \cos(kx - \omega t) + a_2 \cos(kx + \omega t)$ thus, the pressure becomes,

$$\frac{\overline{P_2} - P_a - gh}{\rho} = -2a_1 a_2 \omega^2 \cos(2\omega t) \quad (1.5)$$

where a_1 and a_2 are the amplitudes at the water free surface in the wavetrains. If one of the interfering wavetrains has a zero amplitude, the right hand of the equation becomes zero implying a constant mean pressure, P_2 . If both the amplitudes are equal, $a_1 = a_2 = a$, the mean pressure varies with an amplitude proportional to the square of the wave amplitude and with twice the frequency of the original water wave, thus satisfying the conditions that favor generation of secondary microseisms.

In a more general case, the power spectral density of the random pressure wavefield generated as a result of non-linear interaction of gravity waves, leading to generation of microseisms is given by (Hasselmann (1963), Ardhuin et al. (2011)) :

$$F_p(\mathbf{x}, f) = [2\pi^2][\rho_w g]^2 f E^2(f/2) \int_0^\pi M(f/2, \phi) M(f/2, \phi + \pi) d\phi \quad (1.6)$$

where F_P is the pressure PSD at a location \mathbf{x} and frequency f , the function E determines the sea surface elevation PSD, the function M is the wave energy distribution over the directions ϕ , whereas the integral denotes the non-dimensional ocean gravity wave interaction term.

As we succeed to explain mathematically the cause of microseisms, we now take a look at some of the possibilities that favor the occurrence of the above physical conditions. Numerical modeling of these noise sources has helped in better understanding the origin and seismic energy distribution. One such model for secondary microseisms has listed three cases that leads to its generation. They are broadly classified as: Class I wind waves with a broad directional spectrum, Class II: sea states with a significant contribution of coastal reflections, and Class III: the interaction of two independent wave systems (Ardhuin et al. 2011). Figure 1.3 illustrates the different conditions of noise generation (Ardhuin et al. 2011). In class I, the waves are generated by local wind with energy distributed at angles larger than 90 deg from the mean wave direction. On interaction with waves in the opposite direction, a pressure source is generated. These type of waves have frequencies larger than 0.2 Hz. In class II, ocean wave-wave interaction occurs due to coastal reflections being the source of waves in the opposing direction. The less likelihood mechanism of noise generation is classified as class III. In this, two distinct wave systems have overlapping frequency spectra and opposite directions. One of these systems is usually the wind-sea, forced by the local wind, and the other is a swell, usually propagating from a different generation area. However, strongest noise sources occur in the middle of ocean basins, where crossing wavefield are more common (Ardhuin et al. 2011).

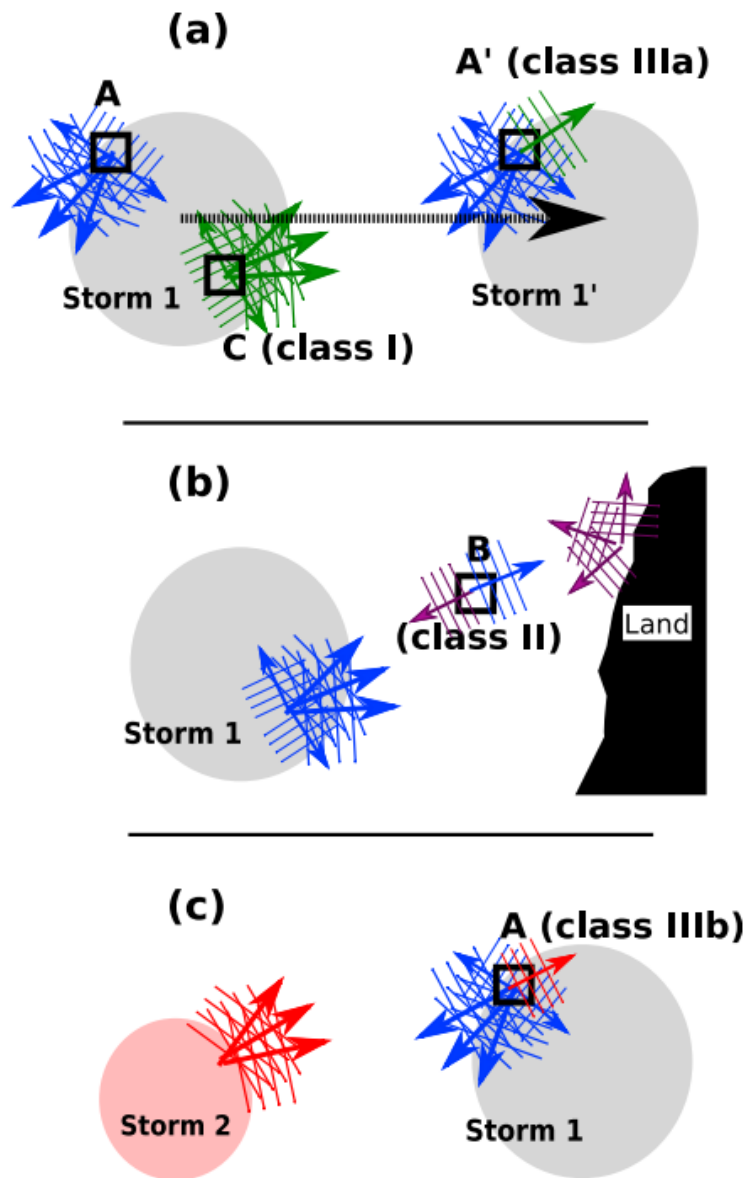


Figure 1.3 – Schematic of wave conditions in noise-generating situations. (a) Storm 1 is rapidly moving so fast that waves generated at C become swell that can meet the wind-sea at point A'. In this case the noise generated by the local wind-sea alone at point C (class I) can be much stronger at point A' because of the wider directional distribution. (b) Noise generated when waves reflect off the coast (class II), and (c) noise generated when waves from two distinct storms cross, here at point A (class III). Source: (Arduin et al. 2011)

1.3 Behavior of microseisms

Microseism sources generally excite Rayleigh waves at frequencies greater than 0.14 Hz (Gutenberg (1958), Ramirez (1940), Haubrich and McCamy (1969), Nawa et al. (1998), Kobayashi and Nishida (1998)), but what puzzled the seismologists was the simultaneous excitation of Love waves or SH waves (Toksöz and Lacoss (1968), Friedrich et al. (1998), Nishida et al. (2008a), Tanimoto et al. (2015a)), with comparable amplitudes as Rayleigh waves. Since the noise sources are close to the ocean surface and the shear component that generates Love waves is absent in the source, this phenomenon needed an explanation. In this chapter, we begin by elaborating some of the evidences that show propagation of Love waves and to what extent a clear understanding of the mechanism was reached. The purpose of this PhD is to deal with the underlying question of understanding the generation of Love waves by numerically modeling the effect of ocean-continental boundary on the propagation of the wave field using 3-D spectral element method. We make a note that this thesis is entirely focused on analyzing the wave field in the frequency band of secondary microseisms [0.1-1 Hz], which will be discussed in the next chapters.

1.4 Observation of Love waves

Many data-driven studies have shown the existence of Love waves. In the past, (Nishida et al. 2008a) showed their appearance in the tiltmeter data obtained from the Japanese Islands. They performed frequency domain beamforming to estimate the temporal and azimuthal changes of the amplitude of Rayleigh and Love waves in the frequency band between 0.1 and 1 Hz. Beamforming is basically the frequency-domain representation of the sum of all array records with time delays predicted by the slowness vector. We show from their study in figure 1.4, Love and Rayleigh wave on the transverse and radial component of the beam in different frequencies 0.06-0.1 Hz, 0.1-0.2 Hz and 0.2-0.4 Hz respectively. Beamforming results shows similar azimuthal distribution of Love and Rayleigh waves but with varying amplitudes. In figure 1.5, the estimated kinetic energy ratio of Love and Rayleigh wave against frequency is shown. The ratio is skewed around 1. For frequencies below 0.1 Hz, the ratio is greater than 1 whereas for frequencies above 0.1 Hz, it drops below 1. In their study, Nishida et al. (2008a) also emphasized that the dominant incident azimuth for Love and Rayleigh wave is strongest in directions along ocean-continent borders, next from deep ocean floors and the weakest from continents. Moreover, the plausible mechanism proposed for the Love wave excitation is ocean-gravity waves coupling with the topography. They proposed that it is the shear traction acting on the sloping sea-floor that leads to simultaneous generation of Love and Rayleigh waves (Fukao et al. 2010).

Several other studies also reported the observation of Love waves. With the new ring laser technique that directly records rotation components of the seismograms, Tanimoto et al. (2015b) estimated the Rayleigh-to-Love wave ratio in the secondary microseism frequency band [0.13 - 0.3 Hz] at Wettzell, Germany. Figure 1.6 depicts the Rayleigh wave surface acceleration recorded on the vertical component of STS-2 and Love wave acceleration derived from ring laser seismograph having comparable amplitudes. The R/L kinetic energy ratio for the frequencies between 0.1-0.3 Hz is found below 1 which implies that Love

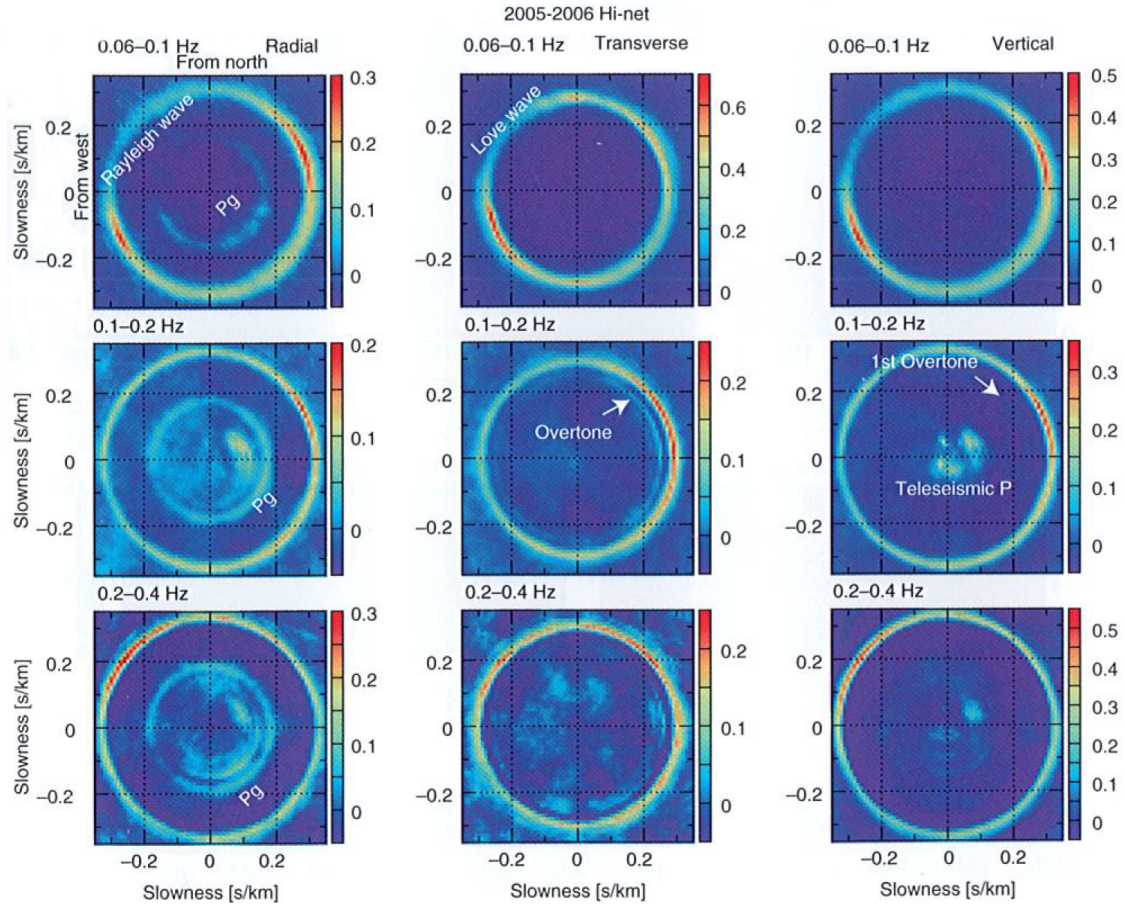


Figure 1.4 – Frequency–slowness spectra on the radial, transverse and vertical component respectively at; top: 0.06–0.1 Hz; middle: 0.1–0.2 Hz; bottom: 0.2–0.4 Hz. The circles are the constant slowness contours. The sources for Rayleigh and Love waves have same azimuthal direction. [Source: Nishida et al. (2008a)]

wave energy is approximately 20 – 35% more than Rayleigh wave energy. However, this result shows contradiction with the previous study (Nishida et al. 2008a) where Love wave energy is found to be 50% of Rayleigh wave energy above 0.1 Hz.

Love waves were also recorded in the three-component seismic array data from Pilbara, Australia (Gal 2017). They used deconvolution-enhanced CLEAN-3C Capon beamforming method (Gal et al. 2016) to compute the mean power for three components shown in Figure 1.7. There are equally distributed sources of vertical, radial and transverse energy present. In figure 1.8, the azimuthal variability of Z-T ratio around the Pilbara region is shown at frequencies 0.35 Hz, 0.6 Hz and 1 Hz. The results show that the vertical and transverse component surface waves are observed from all the coastlines of Australia except for the east coast. The R_g waves (high frequency crustal Rayleigh wave) recorded on the vertical component show strong azimuthal dependence as compared to L_Q/L_g (L_Q , Love wave; L_g , superposition of Love modes) energy recorded on the T component. At lowest frequency, the Z component energy is almost twice the energy on the T component. However, the ratio shows a decrease at higher frequencies and high abundance of Love wave energy was observed along the coastlines in the south-southwest region. Gal (2017) showed the strong dependence of the Z/T power ratio as a function of the location of the coastline with respect to the array. The directionality of L_Q waves generation was found

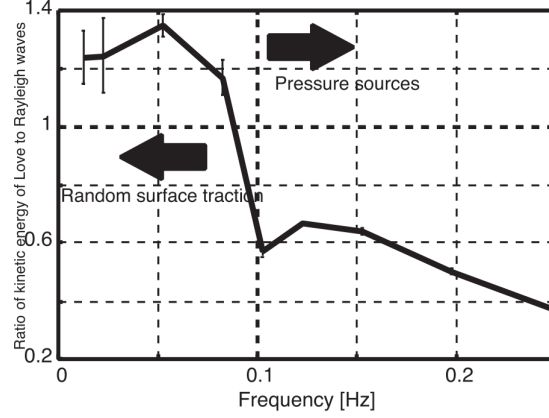


Figure 1.5 – Energy ratio of Love to Rayleigh waves as a function of frequency (from 0.01 to 0.25 Hz). Below 0.1 Hz the ratio is about 1. There is a sudden decrease at 0.1 Hz above which the energy ratio is about 0.5. This sudden change in energy ratio indicates a change of excitation mechanism across 0.1 Hz. [Source: [Nishida et al. \(2008a\)](#)]

to coincide with areas covered with thick seafloor sediments. The plausible mechanism suggested is $R_g - to - L_Q$ conversion at the sedimentary basin boundaries thus converting the amplified R_g energy in the form of Love waves.

Understanding the mechanism kept gaining interest of the seismologists and different methods were adopted. One very recent study ([Ziane and Hadziioannou 2019](#)) proposed the means of multiple scattering of surface waves as a possible mechanism for the generation of Love waves in the secondary microseism by computing Love-to-Rayleigh wave ratio in a highly heterogeneous 3-D media (represented in figure 1.9). In order to represent the heterogeneous medium, von Karman function was chosen to model the Earth’s crust. It’s 3D PSDF (power spectral density function) is given by ([Sato et al. 2012](#)) :

$$P(m) = \frac{8\pi^{3/2}\Gamma(\kappa + 3/2)\sigma^2 a^3}{\Gamma(\kappa)(1 + a^2 m^2)^{\kappa+3/2}} \quad (1.7)$$

where a is referred to as the correlation length, constraining the corner wave number of the PSDF, while the Hurst exponent (κ) gives the decay of the PSDF after the corner wave number. The fluctuation strength σ determines the deviation from the mean elastic property of the medium. m represent the wave number of the medium and wavefield respectively. Γ is the gamma function.

In this study, they obtained L/R ratio for different fluctuation strength, σ (figure 1.10) and correlation length a (figure 1.11). The ratio is found to increase with increasing σ . For example, in their case study, fluctuation strength varies between 5% and 30% but the L/R ratio stabilizes after three to four scattering mean free path (SMFP gives distance after which the wave field is statistically scattered the first time). It is shown in figure 1.10, the L/R ratio stabilizes around 0.2 for fluctuation strength of 10% and propagation distance is 2.5 SMFP whereas for $\sigma = 20$ or above, L/R ratio reaches as high as 0.6 ([Ziane and Hadziioannou 2019](#)). When L/R ratio is computed for different correlation length a (50 m, 500 m) as shown in fig 1.11, it increases from 0.2 to 0.5 respectively. They also studied the effect of layered medium (single layer (SL), multiple layers (ML), gradient layers (GL)) on the ratio. The results shown in figure 1.12 demonstrate similar increasing

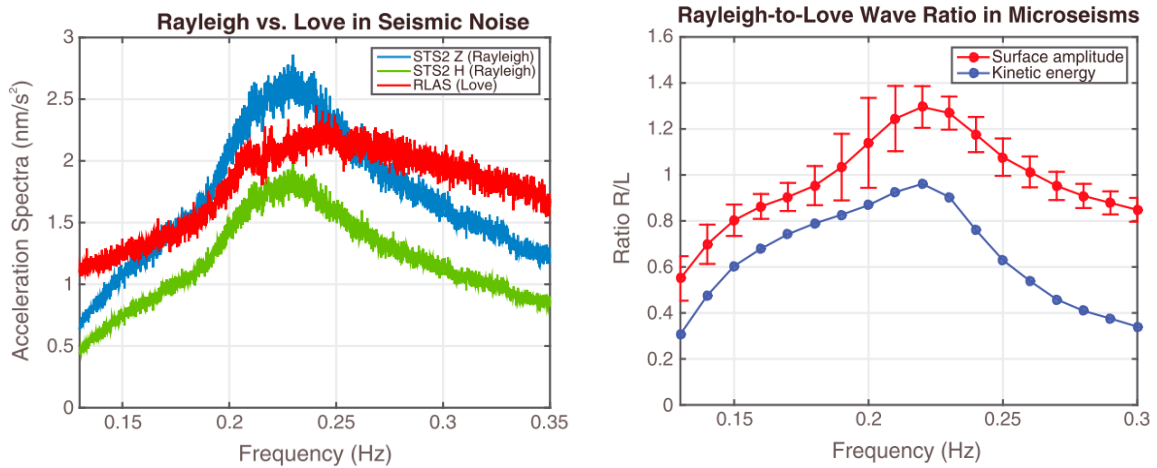


Figure 1.6 – Left: Comparison among the transverse acceleration from the rotation measurements (red), the vertical acceleration from STS-2 (blue), and the horizontal acceleration from the vertical acceleration plus theoretical surface ellipticity (green). The peak is observed at 0.22-0.23 Hz where rayleigh wave acceleration exceeds Love wave acceleration by 20% but becomes lower outside this frequency range. Right: The Rayleigh/Love ratio of surface amplitudes (red) and the ratio of the kinetic energy (blue). The R/L kinetic energy ratio is above 1 only for frequency range 0.22-0.23 Hz. (Tanimoto et al. 2015b)

rate of L/R for the SL and ML types with maximum ratio obtained between 0.3 and 0.4 after propagation distance of 5 SMFP. The L/R ratio for the GR model increases slower and reaches a maximum value of around 0.3. It was indicated that Rayleigh wave-field scattering does not show strong dependence on the layering structure, however the conversion of wavefield to Love waves is more effective for layering types with sharp velocity contrasts. They also proposed a medium with multiple layer plus gradient to be the best condition for the generation of Love waves. In case of real earth model, L/R ratio reported was 0.2 for frequency around 0.2 Hz. Since these ratios are lower than the observed (Nishida et al. (2008a), Tanimoto et al. (2015a)) scattering could be considered as one of the factors of Love wave excitation but it could not fully explain the observations.

1.5 Methodology

1.5.1 Spectral Element method

Spectral element method has many applications in the field of seismology (Chaljub et al. 2007). It has been utilized for studying seismic wave propagation in 2D and 3D structures (Faccioli et al. 1997). For this thesis, we apply the method to demonstrate the effect of ocean-continental slope on wave propagation inside a 3D media. In this section, we elucidate the important wave equation governing seismic wavefield propagation and the schemes used to obtain its solution (Igel 2017, Chapter 7).

Spectral element method is a high degree finite element method that uses a specific set of basis functions inside the elements - the Lagrange polynomials combined with an interpolation scheme based upon the Gauss-Lobatto-Legendre (GLL) collocation points (Komatitsch and Vilotte (1998), Komatitsch and Tromp (1999), Komatitsch et al. (2000), Cupillard et al. (2012)) that makes spectral element method extremely efficient and a fa-

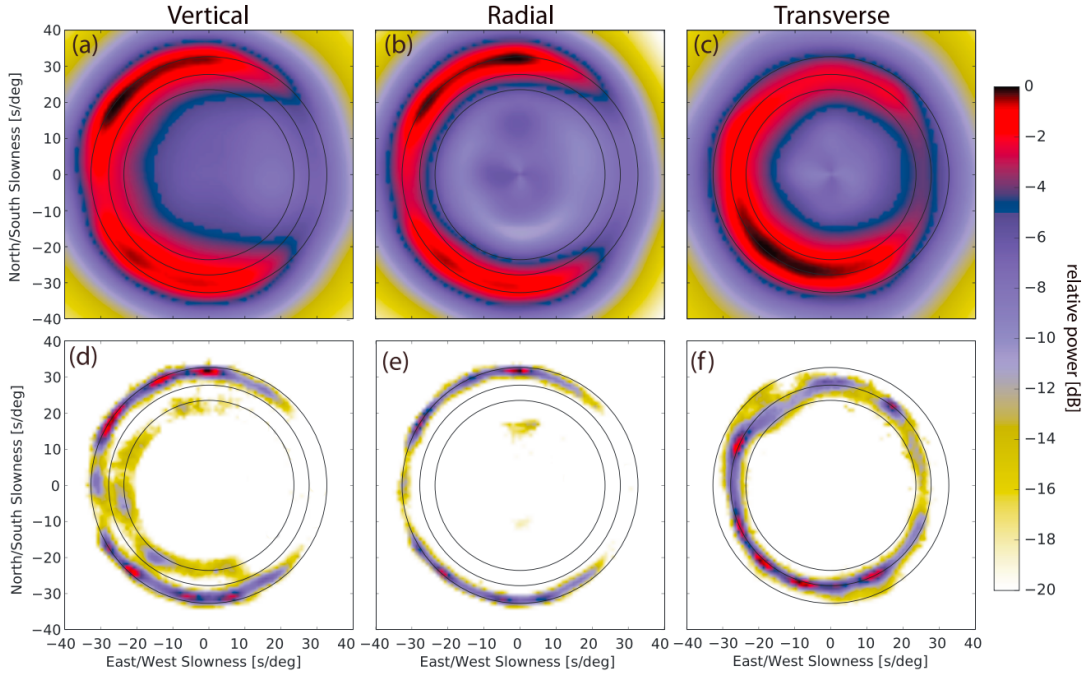


Figure 1.7 – Beamforming results for the three components using seismic array data in Pilbara for Z, R and T components at $f_1 = 0.35 \pm 0.0175$ Hz. (a-c) using the conventional 3C Capon approach. (d-f) displays the result with CLEAN-3C (Gal et al. 2016) that results in a sidelobe free power. The black circles are of constant velocity 3.4 , 4.0 and 4.7 km/s. The results show the directional characteristics of Rg waves sources on the radial and vertical component whereas LQ waves sources on the T component. From (Gal 2017)

avorable method because the mass matrix that needs to be inverted in the finite element formulation becomes diagonal (except it only works with hexahedral grids in 3D) and easily solvable. Another advantage of using this method is the implicit implementation of free-surface boundary condition.

Starting with the classical 1D elastic wave equation for shear waves (Igel 2017; Chapter 7, p 184),

$$\rho \partial_t^2 u = \partial_x (\mu \partial_x u) + f \quad (1.8)$$

where u is the displacement , f the external force, ρ the mass density, and μ the shear modulus. u and f depend on x and t (x : space ; t : time)

To find the solution of the wave equation for an Earth model, the important boundary condition that needs to be obeyed while simulating wave propagation, the stress-free condition at the Earth's surface i.e.,

$$\sigma_{ij} n_j = 0, \quad (1.9)$$

where σ_{ij} is the symmetric stress tensor and n_j the normal vector, which using the stress-strain relation can be written in the form:

$$\mu \partial_x u(x, t)|_{x=0,L} = 0, \quad (1.10)$$

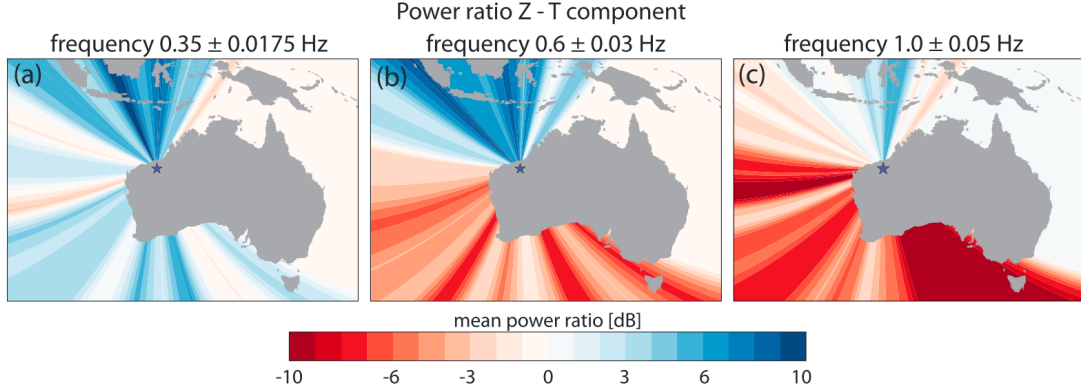


Figure 1.8 – Azimuth variability of power ratio between the Z and T components (Z component is mainly composed of phases $Rg + Lg$). The Z/T ratio at frequency 0.35 Hz is positive for directions where Rg show strong beam power, and negative for directions with low Rg beam power. There is almost zero T component. At frequency 0.6 Hz, all directions from the south to west are dominated by T component energy. Only along the northern coastlines, there is strong Rg beam power. At frequency 1 Hz, Rg is stronger only towards north-northeast direction. The Z/T power ratio integrated over all directions are: 1.95 for f1, 1.86 for f2, and 1.01 for f3. From (Gal 2017)

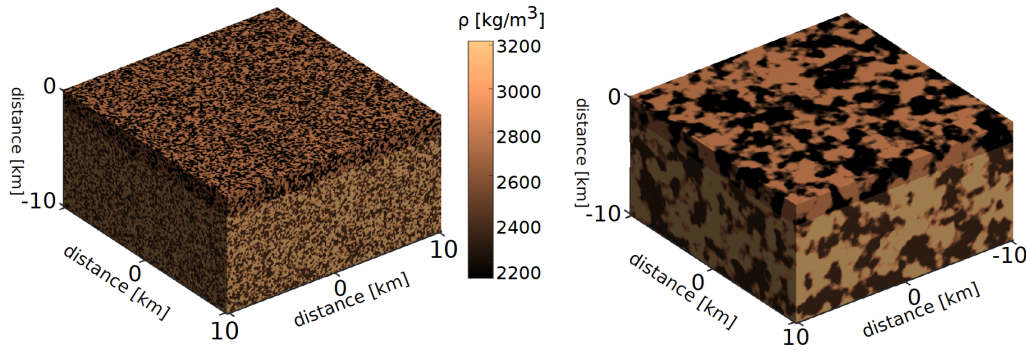


Figure 1.9 – Two realizations of a random medium with different correlation lengths; left: correlation length $a=50$ m; right: correlation length $a=500$ m; the different colours show the random distribution of the density kg/m^3 given by the von Karman PSDF (see equation 1.7). From (Ziane and Hadziioannou 2019)

$x=0, L$ are the spatial boundaries of the domain D ($x \in D = [0, L]$). We now formulate the weak form of the wave-equation, In order to do that, equation 1.9 is multiplied by the time-independent test function $v(x)$ as shown in equation 1.12. $v(x)$ is so chosen that it, together with its first derivative, is square integrable over the integration domain D .

$$\int_D v \rho \partial_t^2 u dx - \int_D v \partial_x (\mu \partial_x u) dx = \int_D v f dx \quad (1.11)$$

Using the boundary condition in eqn 1.11

$$\partial_x u(x, t)|_{x=0} = \partial_x u(x, t)|_{x=L} = 0. \quad (1.12)$$

and applying integration by parts leads to,

$$\int_D v \rho \partial_t^2 u dx + \int_D \mu \partial_x v \partial_x u dx = \int_D v f dx, \quad (1.13)$$

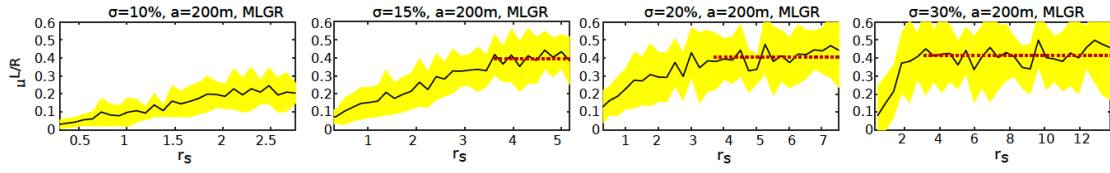


Figure 1.10 – L/R ratio as a function of distance, for varying fluctuation strength σ . The black line shows the mean over 14 angular directions(see figure 2, Ziane et al. 2019) and the yellow area indicates one standard deviation. (Ziane and Hadziioannou 2019)

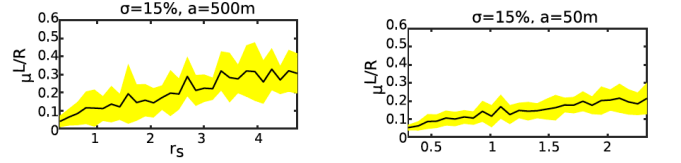


Figure 1.11 – L/R ratio as a function of distance with varying correlation length a . (Ziane and Hadziioannou 2019)

Equation 1.13 is equivalent to eqn 1.9 if and only if eqn 1.13 is true for all possible test functions $v(x)$.

We note from equation 1.13 that the boundary condition is implicitly fulfilled. The next step required is to determine the displacement field u . In order to simulate wave propagation in Earth models with heterogeneous distributions of elastic parameters, seismic wavefield u is computed using the Galerkin method (Igel 2017, Chapter 7, p 186).

$u(t)$ is represented as the superposition of basis functions $\phi_i(x)$ weighted by time-dependent coefficients $u_i(t)$, resulting in approximate displacement field $\bar{u}(x, t)$:

$$u(x, t) \simeq \bar{u}(x, t) = \sum_{i=1}^{N_p} u_i(t) \phi_i(x) \quad (1.14)$$

where N_p equivalentents the number of test functions superimposed. Hereafter, the important step is to use the same function ϕ_i as the test function $v(x)$ in solving equation 1.13, hence obtaining

$$\int_D \phi_i \rho \partial_t^2 \bar{u} dx + \int_D \mu \partial_x \phi_i \partial_x \bar{u} dx = \int_D \phi_i f dx, \quad (1.15)$$

Equations 1.15 and 1.16 are now combined that leads to the equation with the unknown coefficients $u_i(t)$:

$$\begin{aligned} & \sum_{i=1}^{N_p} [\partial_t^2 u_i(t) \int_D \rho(x) \phi_j(x) \phi_i(x) dx] + \\ & \sum_{i=1}^{N_p} [u_i(t) \int_D \mu(x) \partial_x \phi_j(x) \partial_x \phi_i(x) dx] = \\ & \int_D \phi_i f(x, t) dx \end{aligned} \quad (1.16)$$

for all basis functions ϕ_j with $j = 1, \dots, n$. this well-known equation for finite-element problems, can be written in matrix notation as:

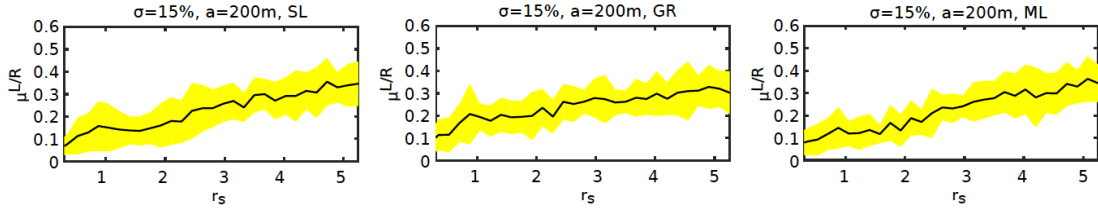


Figure 1.12 – L/R ratio as a function of distance for three models with varying layering types. All models have $\sigma=15$ and correlation length $a=200$ m. (Ziane and Hadziioannou 2019)

$$M\partial_t^2 u(t) + Ku(t) = f(t), \quad (1.17)$$

with implicit matrix-vector operations. The mass-matrix (M), stiffness matrix (K) and volumetric forces $f(t)$ are defined over the entire domain.

From eqn 1.17, the mass matrix is written as:

$$M_{ji} = \int_D \rho(x)\phi_j(x)\phi_i(x)dx, \quad (1.18)$$

the stiffness matrix :

$$K_{ji} = \int_D \mu(x)\partial_x\phi_j(x)\partial_x\phi_i(x)dx, \quad (1.19)$$

and the vector containing the volumetric forces $f(x,t)$:

$$f_j(t) = \int_D \phi_j f(x,t)dx. \quad (1.20)$$

To obtain the solution of the wave equation another level of discretization is required where the domain D is divided into subdomain D_e [consisting of n_e elements], allowing the introduction of discontinuities in material parameters that in turn leads to discontinuity of the displacement gradient ∇u (see Igel 2017: Chapter 7, p 188). The equation 1.17 can be written as,

$$\begin{aligned} & \sum_{i=1}^{N_p} [\partial_t^2 u_i(t) \sum_{e=1}^{n_e} \int_{D_e} \rho(x)\phi_j(x)\phi_i(x)dx] \\ & + \sum_{i=1}^{N_p} [u_i(t) \sum_{e=1}^{n_e} \int_{D_e} \mu(x)\partial_x\phi_j(x)\partial_x\phi_i(x)dx] \\ & = \sum_{e=1}^{n_e} \int_{D_e} \phi_j(x)f(x,t)dx, \end{aligned} \quad (1.21)$$

representing a linear system of N_p equations for each j . The basis functions are also restricted to reside inside the elements D_e as

$$\bar{u}(x,t)|_{x \in D_e} = \sum_{i=1}^{N_p} u_i^e(t)\phi_i^e(x), \quad (1.22)$$

where N_p denotes the number of basis functions for polynomial order N to be summed.

Using equation 1.22 and 1.23, equation 1.18 becomes

$$M^e \partial_t^2 u(t) + K^e u^e(t) = f^e(t), e = 1, \dots, n_e \quad (1.23)$$

$u^e, K^e, M^e,$ and f^e are the coefficients of the unknown displacement inside the element, stiffness, mass matrices with information on the density and elastic parameters, and forces respectively. Matrix-vector multiplications are implicit.

To facilitate the above mathematical operations under the integral, there is a need to define the spatial coordinates of an element in order to solve the integrals. This is achieved by using the reference interval F_e between $[-1, 1]$, thus mapping the global system $x \in D$ to the local coordinates represented as $\xi \in F_e$. The transformation eventually looks like:

$$x = F_e(\xi), \xi = \xi(x) = F_e^{-1}(x), e = 1, \dots, n_e, \quad (1.24)$$

where n_e is the number of elements, and $\xi \in [-1, 1]$.

So that x is related to the local coordinate ξ as

$$x(\xi) = F_e(\xi) = \frac{h_e(\xi + 1)}{2} + x_e, \quad (1.25)$$

where x_e represents the coordinate of the left side of the element and h_e is the element size. According to the scheme, the Lagrange polynomials l_i^N are used as the interpolating functions.

$$\phi_i \rightarrow l_i^N(\xi) \quad (1.26)$$

$$l_i^N(\xi) = \prod_{j \neq i}^{N+1} \frac{\xi - \xi_j}{\xi_i - \xi_j}, i, j = 1, 2, \dots, N + 1, \quad (1.27)$$

where ξ_i are fixed points in the interval $[-1, 1]$ and the Lagrange polynomials hold the orthogonality.

$$l_i^N(\xi_j) = \delta_{ij}, \quad (1.28)$$

$\delta_{ij} = 1$ if $i=j$ and 0 otherwise. the points ξ are chosen according to so-called Gauss-Lobatto-Legendre (GLL) points.

So, for $N+1$ Lagrange polynomials, the order N is equivalent to the number of intervals inside each element which implies that with $N= 2$ we would obtain a spectral-element discretization with even spacing of collocation points. As the order increases, the difference between the distance of collocation points increases in a linear way. The GLL points are the roots of the first derivative of the Legendre polynomials L_N of degree N .

Hence, our displacement function (from equation 1.23) looks like

$$u^e(\xi) = \sum_{i=1}^{N+1} u^e(\xi_i) l_i(\xi) \quad (1.29)$$

and the wave equation transforms to:

$$\begin{aligned} & \sum_{i=1}^{N+1} [\partial_t^2 u_i^e(t) \int_{-1}^1 \rho(\xi) l_j(\xi) l_i(\xi) \frac{dx}{d\xi} d\xi \\ & + \sum_{i=1}^{N+1} [u_i^e(t) \int_{-1}^1 \mu(\xi) \partial_\xi l_j \partial_\xi l_i(\xi) \left(\frac{d\xi}{dx}\right)^2 \frac{dx}{d\xi} d\xi \\ & = \int_{-1}^1 l_j(\xi) f(\xi, t) \frac{dx}{d\xi} d\xi \end{aligned} \quad (1.30)$$

This brings us to the point where everything is known, only the displacement and acceleration values u_i and $\partial_t^2 u_i$ are unknown. One efficient way to solve the integrals and find the unknown values is defined such that the function to be integrated, say $f(x)$ is replaced by a polynomial approximation that can be integrated analytically. In spectral element method, Lagrange polynomials have the job as interpolating functions.

For example, the arbitrary function $f(x)$ defined in the interval $x \in [-1, 1]$ using the integration scheme can be represented as (Igel 2017: Chapter 7, p 194):

$$\int_{-1}^1 f(x) dx \simeq \int_{-1}^1 P_N(x) dx = \sum_{i=1}^{N+1} w_i f(x_i), \quad (1.31)$$

with

$$P_N(x) = \sum_{i=1}^{N+1} f(x_i) l_i^N(x), \quad (1.32)$$

and the integration weights are calculated with

$$w_i = \int_{-1}^1 l_i^N(x) dx. \quad (1.33)$$

We note that the numerical results converges to the exact solution for a smooth polynomial function with higher order. Now that the GLL integration scheme was chosen, another level of discretization is introduced where the continuous integration over the elements is replaced by a sum of over $N+1$ weighted functional values located at well-known GLL points which brings us to the solution equations for our spectral-element system at the element level represented using matrix notation:

$$\sum_{i=1}^{N+1} M_{ji}^e \partial_t^2 u_i^e(t) + \sum_{i=1}^{N+1} K_{ji}^e u_i^e(t) = f_j^e(t), e = 1, \dots, n_e \quad (1.34)$$

where

$$M_{ji}^e = \omega_j \rho(\xi) \frac{dx}{d\xi} \delta_{ij} |_{\xi=\xi_j} \quad (1.35)$$

$$K_{ji}^e = \sum_{k=1}^{N+1} \omega_k \mu(\xi) \partial_\xi l_j(\xi) \partial_\xi l_i(\xi) \left(\frac{d\xi^2}{dx} \right) \frac{dx}{d\xi} |_{\xi=\xi_k} \quad (1.36)$$

$$f_j^e = \omega_j f(\xi, t) \frac{dx}{d\xi} |_{\xi=\xi_j} \quad (1.37)$$

The equation contains derivatives of basis functions, (approximated by Lagrange polynomials) which are calculated using Legendre polynomials, following Funaro (1993). Legendre polynomials defined in the interval $\xi \in [-1, 1]$ are given as:

$$L_N(\xi) = \frac{1}{2^N N!} \frac{d^N}{d\xi^N} (\xi^2 - 1)^N \quad (1.38)$$

where N denotes the polynomial degree. And, hence their derivatives are computed using:

$$\partial_\xi l_k(\xi_i) = \sum_{j=0}^N d_{ij} l_k(\xi_j), k = 0, \dots, N \quad (1.39)$$

with

$$d_{ij} = \begin{cases} -\frac{1}{4}N(N+1), & \text{if } i = j = 0 \\ \frac{L_N(\xi_i)}{L_N(\xi_j)} \frac{1}{\xi_i - \xi_j}, & \text{if } 0 \leq i \leq N, 0 \leq j \leq N, i \neq j \\ 0, & \text{if } 1 \leq i = j \leq N-1 \\ \frac{1}{4}N(N+1), & \text{if } i = j = N \end{cases} \quad (1.40)$$

Finally, the derivatives of the basis function is approximated using:

$$\partial_\xi u^e(\xi) = \sum_{i=1}^{N+1} u^e(\xi_i) \partial_\xi l_i(\xi) \quad (1.41)$$

In the end an important step in order to find the complete solution for the entire physical domain is linking the elemental results called assembly. Since, the classic finite (spectral) element method assumes continuity of the solution fields at the element boundaries, the complete solution is obtained by simply adding up the elemental solutions at the corresponding boundary boundary collocation points, thus with the principle of one value for each element boundary in the spectral element method. As illustrated in Section 7.5, Chapter 7 (Igel 2017), on assimilation of mass matrix and stiffness matrix for n_e of elements, a system of equations with $n_g = n_e \times N + 1$ (g stands for global matrices and N: interpolation order) coefficients for the displacement u_g is obtained. M_g & K_g have dimensions $n_g \times n_g$. The force vector f_g also has n_g elements. u_g , as a response to time-dependent forces, is updated as

$$u_g(t + dt) = dt^2 [M_g^{-1} (f_g(t) - K_g u_g(t))] + 2u_g(t) - u_g(t - dt) \quad (1.42)$$

1.5.2 Mesh generation

The first and foremost step required in order to implement this method and study the seismic wavefield is meshing of the domain. For our purpose, we use the software Trellis to achieve well-segmentation of the domain. Prior to that, there exists some necessary conditions to be taken into consideration for accurate meshing.

For $4 \leq N \leq 8$, N being the polynomial degree, at least five GLL nodes per wavelength are needed in the region to describe the seismic wavefield. The mesh is composed of hexahedral elements and honors the main discontinuities.

The mesh element size (d) for a polynomial degree $4 \leq N \leq 8$, d is constrained by the shortest wavelength λ_{min} propagating in the medium as:-

$$d \leq N/5\lambda_{min}$$

We also need to ensure stability of the time-marching. The time step δt of the finite difference scheme has to verify the Courant-Freidrichs-Lewy(CFL) condition:

$$\delta t \leq C \frac{\delta x}{\alpha}$$

where C denotes the Courant number, usually between 0.3 and 0.4 and $\delta x/\alpha$ is the minimum ratio between grid spacing δx being the distance between two GLL nodes) and P-wave speed of the slower medium.

1.5.3 Green's function

The seismic wave propagation computed using spectral element method represents the green's function (i.e., impulse response of the medium) and the signal recorded by the receiver is the convolution of green's function with the source. The interest of this study lies in modeling Love waves in secondary microseisms. Since these noise sources are unknown, we can simply investigate the Green's function as the seismic wave field produced by secondary microseism. This is due to the linearity between the convoluted signal and the Green's function. In our study, we compute seismic wave field using a single point source that represents secondary microseism.

1.5.4 Computation of Rotational component

In this section, we explain the computation of rotational component that will be used in the analysis of the wave field produced using the above described spectral element method in chapter 3. It is an effective method that assists in modeling SH/Love waves generated due to secondary microseisms. One of the advantage of computing vertical rotation and horizontal acceleration is that it allows the estimation of local Love wave phase velocity and its propagation direction. It is derived as follows: The displacement of any point \mathbf{x} in a classical frame when perturbed by an infinitesimal quantity $\delta \mathbf{x}$ is written as (Aki & Richards 2002, p. 13):

$$\mathbf{u}(\mathbf{x} + \delta \mathbf{x}) = \mathbf{u}(\mathbf{x}) + \mathbf{G}\delta \mathbf{x} \tag{1.43}$$

$$= \mathbf{u}(\mathbf{x}) + \varepsilon \delta \mathbf{x} + \omega \delta \mathbf{x} \tag{1.44}$$

where $\mathbf{G}, \varepsilon, \omega$ are the gradient, strain, and rotation second order tensors, respectively, and

$$\omega = \frac{1}{2} \nabla \times u(x) \quad (1.45)$$

ω is a vector representing the angle of rigid rotation (three components of rotation) caused due to the disturbance.

In pursuit of our interest, let us consider the case of transversely polarized plane wave with displacement given by $\mathbf{u}(x,y,z,t) = (0, u_y(t-x/c), 0)$ propagating in the x direction, with c being the horizontal phase velocity. Using the rotation expression we get,

$$\omega(x, y, z, t) = \frac{1}{2} \nabla \times \mathbf{u}(x, y, z, t) = (0, 0, -\dot{u}_y(t-x/c)/(2c)) \quad (1.46)$$

Thus we have,

$$\omega_z(x, y, z, t) = -\frac{\dot{u}_y(x, y, z, t)}{2c} \quad (1.47)$$

Since Rayleigh waves are vertically polarized, hence they do not generate a vertical component of rotation whereas Love waves have horizontal transverse polarization, thereby producing vertical rotational. Now in practice, there are two ways of observing rotational ground motions a) finite-differencing of seismic array data b) directly through ring laser, mechanical gyros). Since we use only array-derived rotation for our study, we briefly describe it in this section.

In eqn. 1.45, the position vector δx is replaced by a non infinitesimal quantity \mathbf{R} , thereby becoming

$$\mathbf{d} = \mathbf{u}(\mathbf{x}+\mathbf{R}) - \mathbf{u}(\mathbf{x}) = \mathbf{G}^{FD} \mathbf{R} \quad (1.48)$$

where \mathbf{G}^{FD} is a first order approximation of \mathbf{G} , assuming \mathbf{u} varies linearly between \mathbf{x} and $\mathbf{x}+\mathbf{R}$. Now if we use three non aligned points, we get two such vectorial equations with one common point

$$\mathbf{d}_1 = \mathbf{G}^{FD} \mathbf{R}_1 \quad (1.49)$$

and

$$\mathbf{d}_2 = \mathbf{G}^{FD} \mathbf{R}_2 \quad (1.50)$$

Thus, if we know the ground displacement at three stations on the surface with known positions, we can estimate $\partial u_x / \partial y, \partial u_y / \partial x$. Hence, the vertical component of rotation can be determined using the expression,

$$\omega_z = \frac{\partial u_y}{\partial x} - \frac{\partial u_x}{\partial y} \quad (1.51)$$

The estimation of local Love wave phase velocity is done using the relation where v_T is the transverse component of the seismogram on velocity

$$\frac{v_T}{\omega_z} = -2c \quad (1.52)$$

1.5.5 Calculation of slope at the ocean-continental boundary

The study focuses on modelling the effect of ocean-continent boundary in generating Love waves and the slope angle plays an important role in determining the amount of conversion taking place at the boundary into Love waves. In this section, we will discuss quantitatively the variation of slope angles worldwide. The method used here depends on the topography data obtained from ETOPO 1 Arc-minute Global Relief model developed by National Oceanic and Atmospheric Administration (NOAA) in its bedrock version. For the calculation of the slope, two points are considered between which the slope calculation is done (Masounave E. (2018) Analyse et Modélisation du bruit sismique longue période (hum)(Master’s thesis, IPGP)). The topography at the ocean-continent interface is divided into $1^\circ \times 1^\circ$ grids. We choose a point of highest altitude and a point of lowest altitude in each grid as shown in figure, and then the slope between the two points are calculated using the formula:

$$slope = \frac{\partial x}{\partial y} \quad (1.53)$$

This method represents good first approximation of the slopes. Figure 1.13 shows the profiles around the coast of three different regions, namely Japan, Germany and Australia according to which slopes were calculated. Different studies in these selected regions have shown the occurrence of Love waves (Section 1.4). Similarly, profiles are selected around the entire globe using this technique. The slope values found at each of these points, as shown in figure 1.14, ranges between 0% and 7%. Around Japan, the slope values are found to vary between 2% and 5.8%. The north-northwest and southern Australian coast has very low slope values (0%-1%). Towards the south-west, slope values are found between 3%-4.5 %. Mainly, Love waves were detected coming from the south-southwest of Australia (figure 1.8). We similarly observe low slope values (0%-1%) along the profile west of Germany.

In this study we show that when we consider model ETOPO 1, most of the slope are lower than 10%. ETOPO 1 provide a smooth variability of the model over a grid of $1^\circ \times 1^\circ$. The local ocean-continent boundary slope can be locally higher. We will address the significance of slope angle in chapter 4.

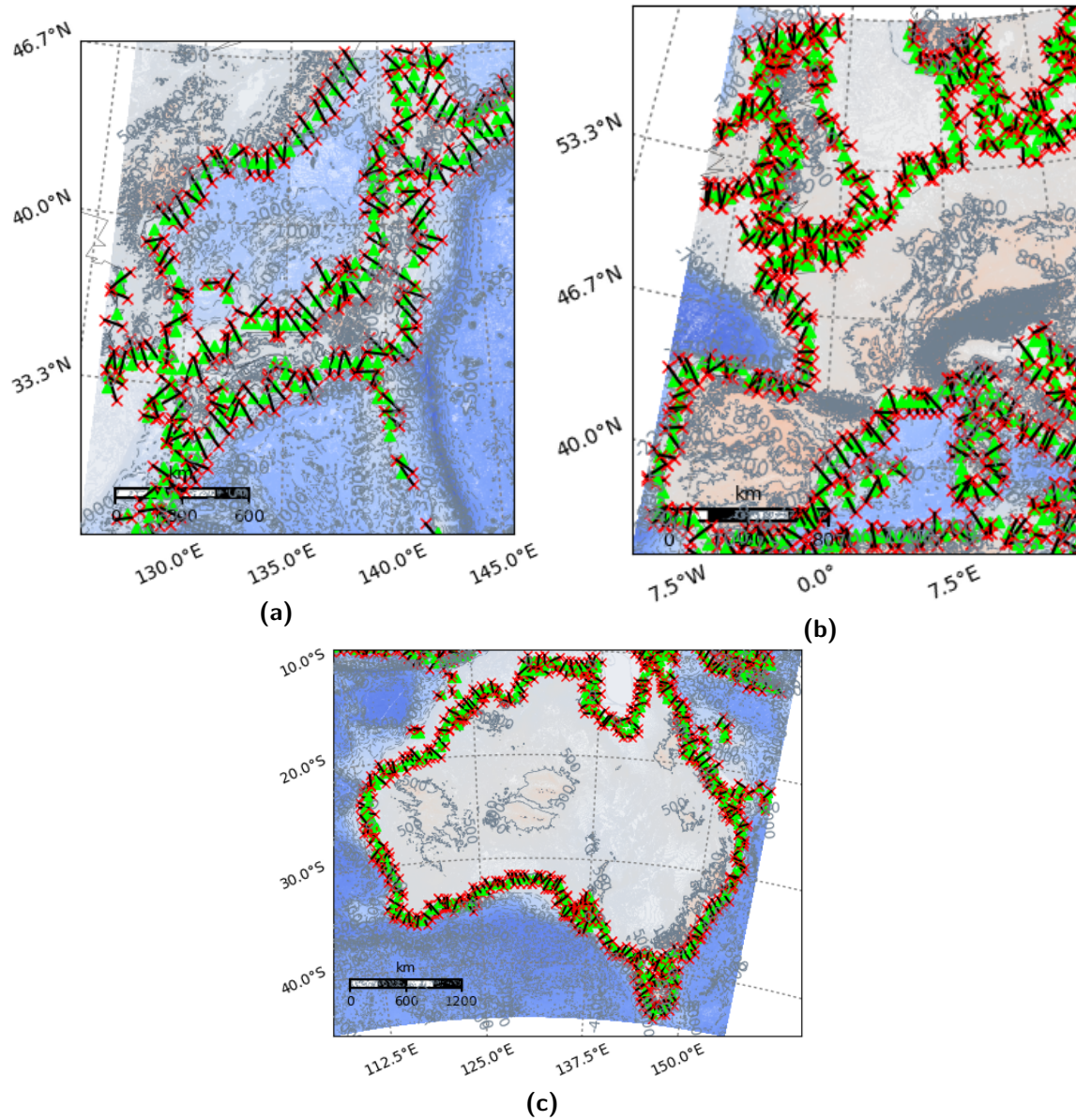


Figure 1.13 – Topographic map of a) Japan b) Germany c) Australia showing the profiles according to which slopes were calculated (black lines) at each point. These profiles are made perpendicular to the coast.

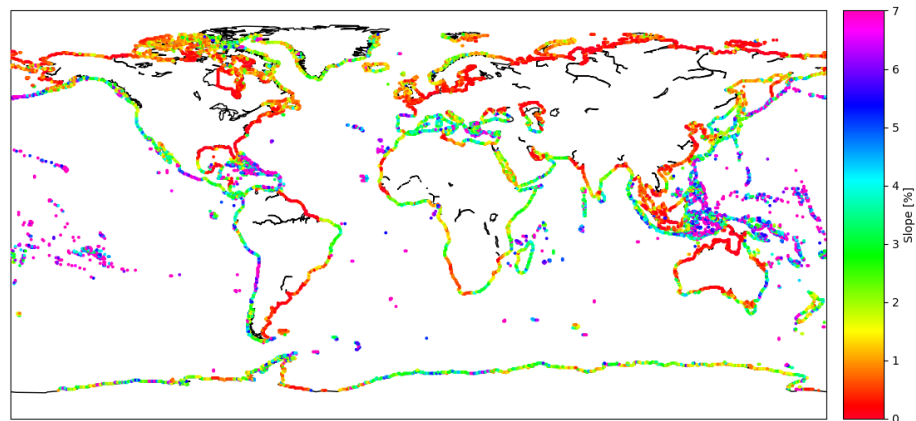


Figure 1.14 – Value of the slope (in percentage) calculated at each source point of the model using the topography data from ETOPO1.

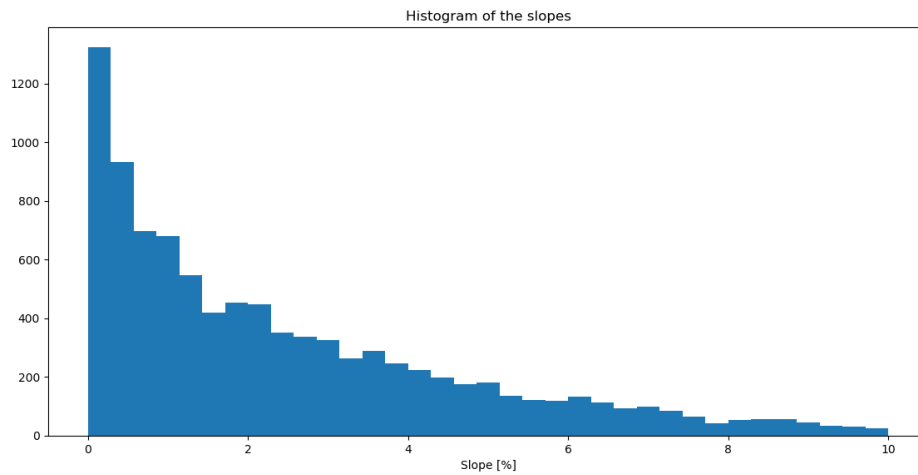


Figure 1.15 – Histogram showing the distribution of the slopes determined in figure 1.14. The distribution of the slope values lies between 0-10 % . Most of the slope values are lower than 2 % . Very few slopes have values greater than 7% when they are computed with model ETOPO 1 which gives an average of the topography on a grid.

Chapter 2

Data Analysis

2.1	Observations of Love waves in Data	36
2.2	Data and Methodology	36
2.2.1	Data	36
2.2.2	Beamforming	36
2.3	Results and Discussion	37

2.1 Observations of Love waves in Data

In the previous chapter, we elaborated the different studies carried over the past years that reported the occurrence of Love waves in secondary microseisms. Before we investigate the underlying generation mechanism of Love waves, we first analyze the data, for example, a few days of data recorded by the seismic array to detect Love waves. We apply the same technique that has been used to detect P, PP & PKP in the seismic noise, called beamforming (Backus et al. (1964), Toksöz and Lacoss (1968), Seriff et al. (1965), Gerstoft et al. (2008), Zhang et al. (2009), Koper et al. (2009), Gerstoft et al. (2008), Obrebski et al. (2013)). Recent applications of beamforming includes examining surface wave microseisms which successfully detected Rayleigh and Love waves in the noise data (Capon (1973), Nishida et al. (2008b)).

2.2 Data and Methodology

2.2.1 Data

In this example, we will use the three-component continuous ground-motion data recorded in the Alaska and California arrays for three days. The data has been procured from the Incorporated Research Institutions for Seismology (IRIS) data management center from the network AK for the period 9-12 October 2014. The pre-processing of the data involves the deconvolution of raw data from the instrument response function and pre-filtering in the frequency band of secondary microseisms [0.1-0.5 Hz].

2.2.2 Beamforming

In our objective to extract secondary microseism Love waves and Rayleigh waves in the seismic data recorded by the station array, we use the beamforming techniques from Meschede et al. (2017) that enable to compute the phase weighted stack of the beams in order to improve the signal to noise ratio (Schimmel and Paulssen (1997), Schimmel and Gallart (2007)). We briefly describe the method here. In this approach, for each window of 128 s we first compute the classical beam as (e.g. Rost and Thomas (2002)) the linear stack:

$$B_w(f, s) = \frac{1}{N^2} \left| \sum_{j=1}^N S_j e^{-i2\pi f s \cdot (\mathbf{x}_j - \mathbf{x}_c)} \right|^2 \quad (2.1)$$

$B_w(f, s)$ represents the average over Fourier spectra $S_j(f)$ of N traces that are phase aligned by multiplication with $e^{-i2\pi f s \cdot (\mathbf{x}_j - \mathbf{x}_c)}$ computed at slowness s . \mathbf{x}_j and \mathbf{x}_c are the positions of station j and the array center, respectively. For each station in the array, the traces with standard deviation larger than 2 times the median standard deviation are discarded to ensure the removal of corrupted data.

We then compute a weight factor $w(f, s)$ that measures the coherency of the incoming wave field independent of its amplitude and minimizes the larger values due to strong incoherent plane waves. The phase stack is used to weight the linear stack $B_w(f, s)$ Meschede et al.

(2017)

$$w(f, s) = \frac{1}{N^2} \left| \sum_{j=1}^N \frac{S_j(f)}{|S_j(f)|} e^{-i2\pi f s \cdot (\mathbf{x}_j - \mathbf{x}_c)} \right|^2 \quad (2.2)$$

The final phase-weighted beam PSD is then constructed as:

$$B_{pw}(f, s) = w(f, s) B_w(f, s) \quad (2.3)$$

To compute the phase weighted beam for our data, we chose the slowness grid in the range (-0.3 - 0.3) s/km and frequency band from 0.1-0.3 Hz as it encompasses the slowness range of secondary microseisms surface and body waves. The ray parameters (slowness) of the phases that can be recorded on the horizontal components are significantly larger than those recorded on the vertical component and can be explained by a mix of crustal phases, $S_g(s \simeq 0.31s/km)$, $L_g(s \simeq 0.28s/km)$ & $S_n(s \simeq 0.21s/km)$ (Isacks & Stephens, 1975). The beamforming results are analyzed in the next section.

2.3 Results and Discussion

Figure 2.1 shows results of the beamforming analysis applied to three days (9-12 December 2014) of the noise recorded by the network AK (left panel) and CI (right panel) calculated at dominant periods of secondary microseism on the three components. We observe a clear patch on the horizontal slowness plane for Z, R & T component mainly at the dominant period 8 s. Z and R components record the same waves as they arrive at same slowness whereas different waves are recorded on the T component. The maximum beam on the vertical and radial component is recorded at slowness higher than 0.3 s/km and at slowness less than 0.3 s/km on the T component. This indicates that Rayleigh waves are recorded on the Z and R components and T component records Love waves. The azimuth of the Rayleigh and Love waves is similar as they both appear from the north-east direction. This may correlate with the direction of strong secondary microseisms present on that day. Location of secondary microseism pressure sources computed using ocean wave-wave interaction model (ardhuin et al., 2011) during different time of the day from 2014-12-09 to 2014-12-10 are shown in figure 2.2, 2.3, 2.4. On these particular days, we observe that noise sources of dominant frequency (0.15 to 0.185 Hz) are continuously prevalent over the period located in the south of Greenland and some sources of high frequency (0.2-0.23 Hz) beginning from the mid day of 2014-12-09 till mid night are also observed. These strong sources could correspond to the microseismic energy from surface waves recorded by the AK and CI networks. The observations on the beam are in good agreement with the noise sources. Thereby indicating that waves recorded by the two networks are generated by these sources located in the coast of South Greenland. In conclusion, we have shown the preliminary results showing occurrence of Love waves in the noise signals recorded for two days. The data is contaminated by random fluctuations which can be removed by using other techniques. This study can be extended further by using more data. We now conduct a synthetic study to understand the generation mechanism of Love waves which is discussed in the coming chapters.

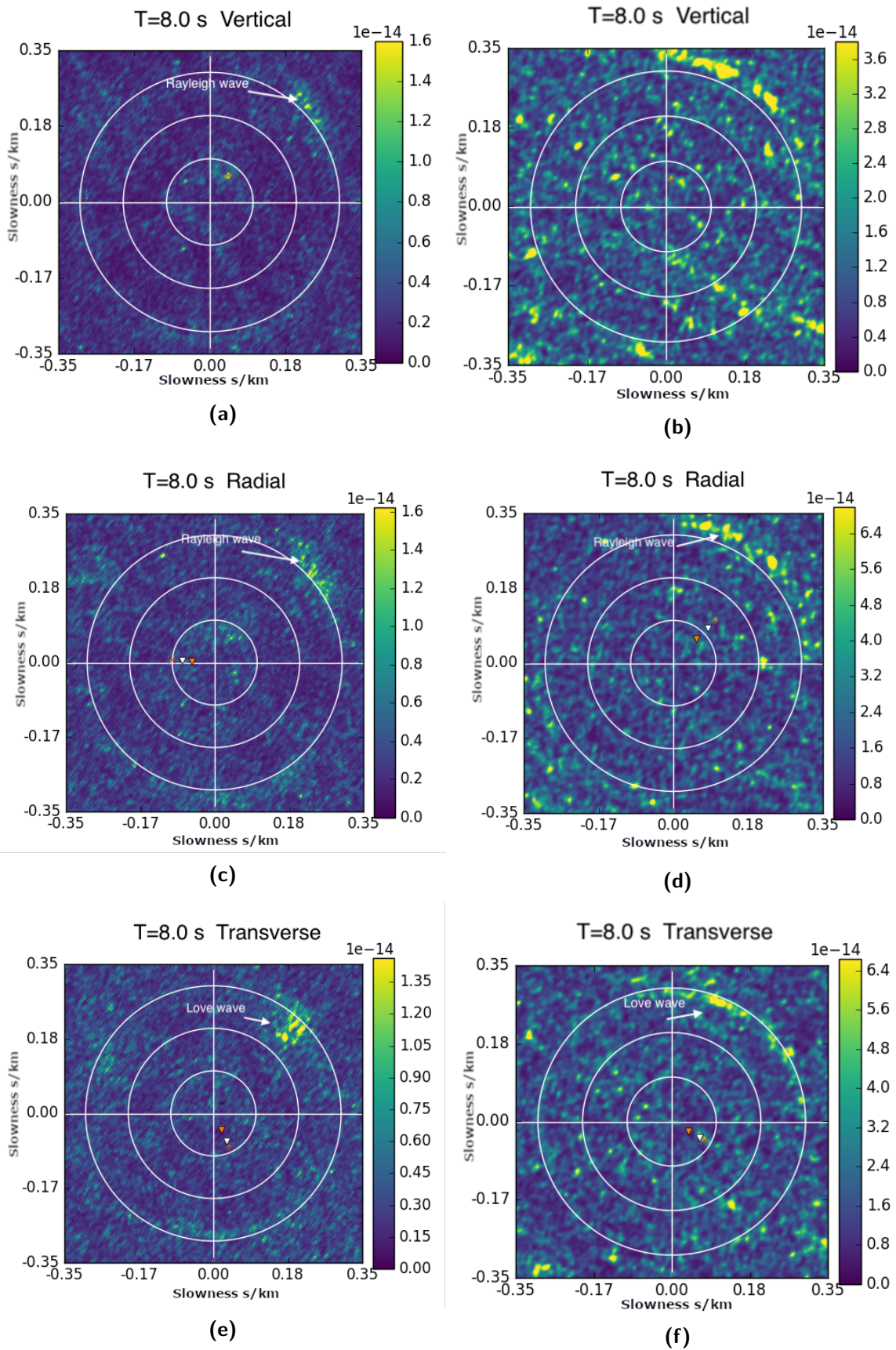
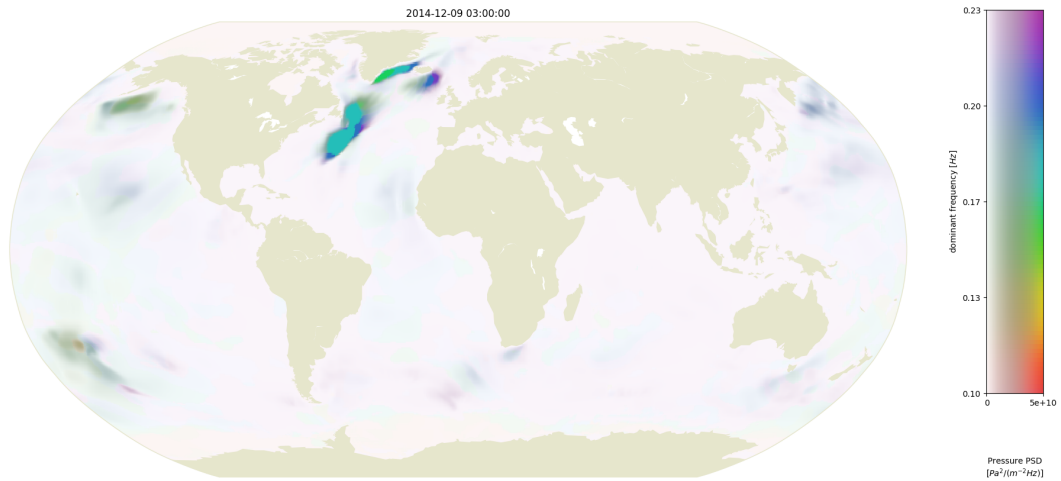
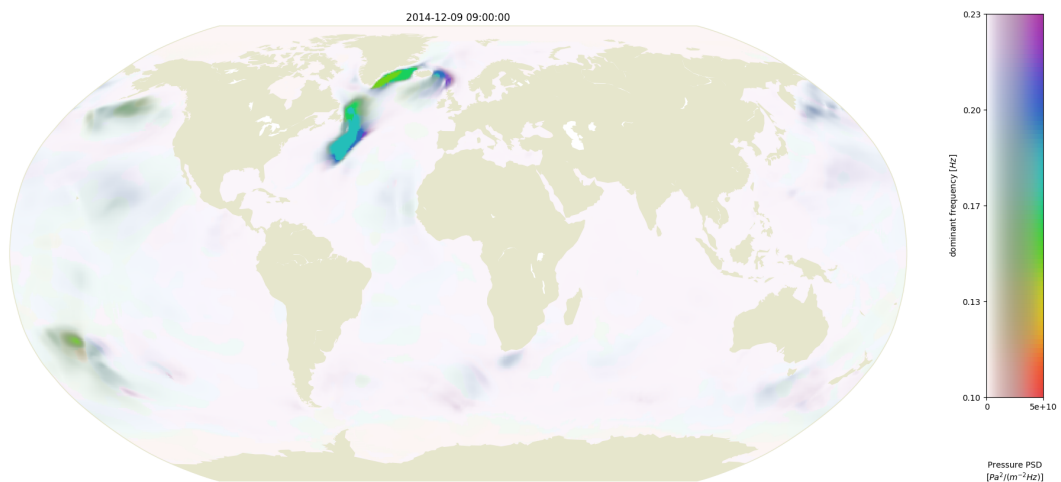


Figure 2.1 – Observed beam PSD for the two-components using seismic noise array data recorded on 09-12 December 2014 by left panel) Alaska (AK) network right panel) California network (CI) at frequency = 0.125 Hz or dominant period 8 s. The white circles are of constant velocity 0.1 km/s, 2 km/s, 3 km/s. The color hue gives the maximum of the beam PSD. The results show sources of Rayleigh waves on the vertical component and Love waves on the T component in the north-east and north-northeast direction detected by the AK and CI array of stations, respectively.

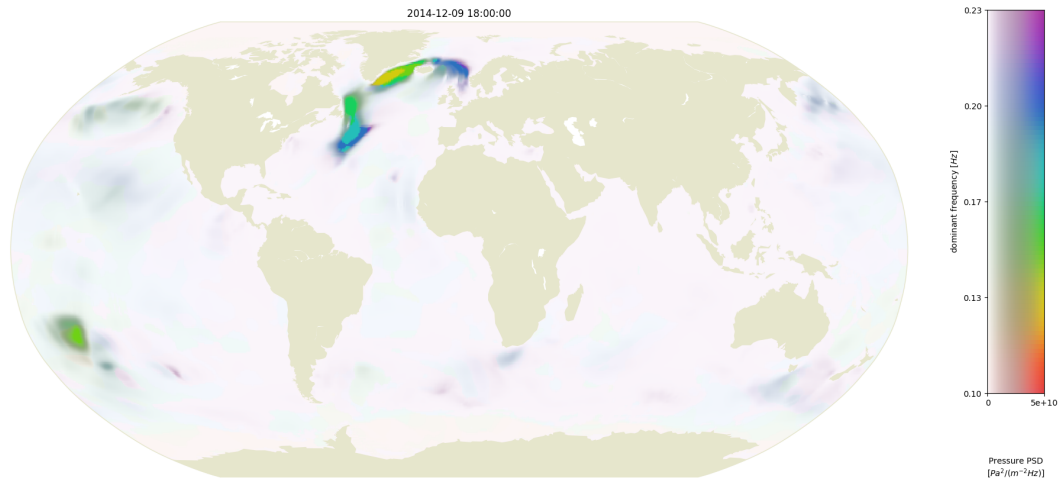


(a)

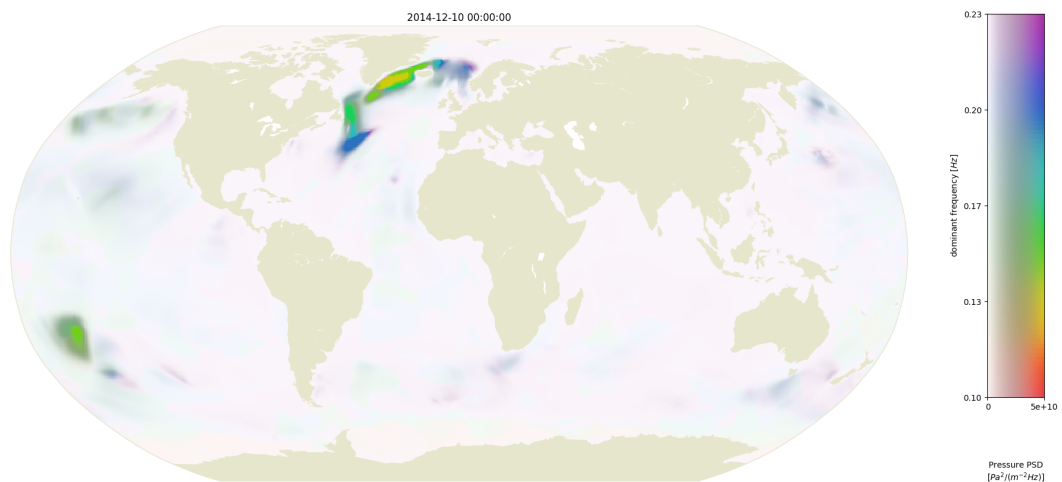


(b)

Figure 2.2 – Pressure PSD on 09 December 2014 for a period at (a) 3h and (b)9h respectively. The color hue represents the dominant frequency and color lightness the spectral maximum of the beam PSD (Ardhuin et al. 2011).

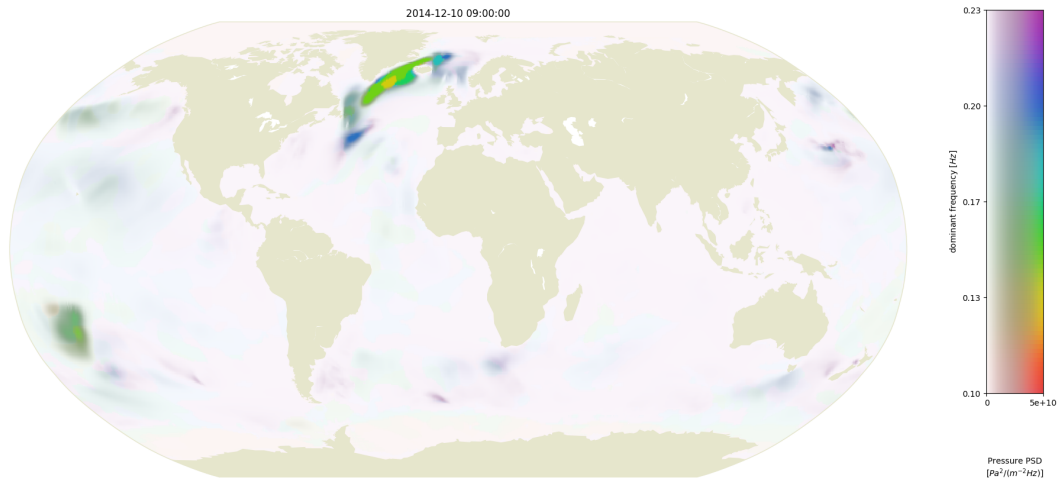


(a)

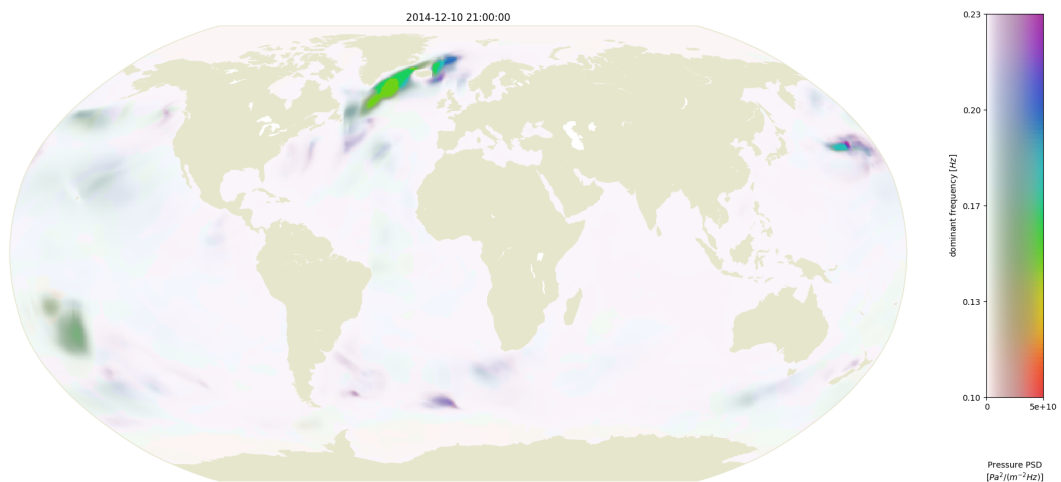


(b)

Figure 2.3 – Pressure PSD on 09 December 2014 for a period at (a) 18h and (b) mid night respectively. The color hue represents the dominant frequency and color lightness the spectral maximum of the beam PSD (Ardhuin et al. 2011).



(a)



(b)

Figure 2.4 – Pressure PSD on 10 December 2014 for a period at (a) 9h and (b) 21h respectively. The color hue represents the dominant frequency and color lightness the spectral maximum of the beam PSD (Ardhuin et al. 2011).

Chapter 3

1D Synthetic Seismograms

3.1	Group and phase velocities for 1-D Earth models	44
3.1.1	Oceanic model: 1 km ocean and 16 km crust & Continental model: 17 km crust	44
3.1.2	Oceanic model: 1 km ocean, 6 km crust and 10 km mantle & Continental model: 7 km crust and 10 km mantle	45
3.1.3	Oceanic model: 3 km ocean, 6 km crust and 10 km mantle & Continental model: 9 km crust and 10 km mantle	48
3.1.4	Oceanic model: 6 km ocean, 6 km crust and 10 km mantle & Continental model: 12 km crust and 10 km mantle.....	50
3.1.5	Oceanic model: 6 km ocean, 3 km sediments, 6 km crust and 7 km mantle	51

We have seen in previous chapter, different studies showing the simultaneous occurrence of Love and Rayleigh waves for secondary microseism noise sources. In the direction of gaining elementary understanding of the different modes of surface waves that can be generated in the earth and the partition of energy within the modes which will also facilitate in the future to determine the characteristics of the seismic wave field generated in 3D and the underlying mechanism, in this chapter, let us first discuss the existence of modes for Rayleigh and Love waves in simple 1-D Earth models using R.B Herrmann's codes (Herrmann) by computing the phase and group velocity. We also generate synthetic seismograms. The selected models correspond to either the oceanic part or the continental part of the different 3D models used in the next chapter.

3.1 Group and phase velocities for 1-D Earth models

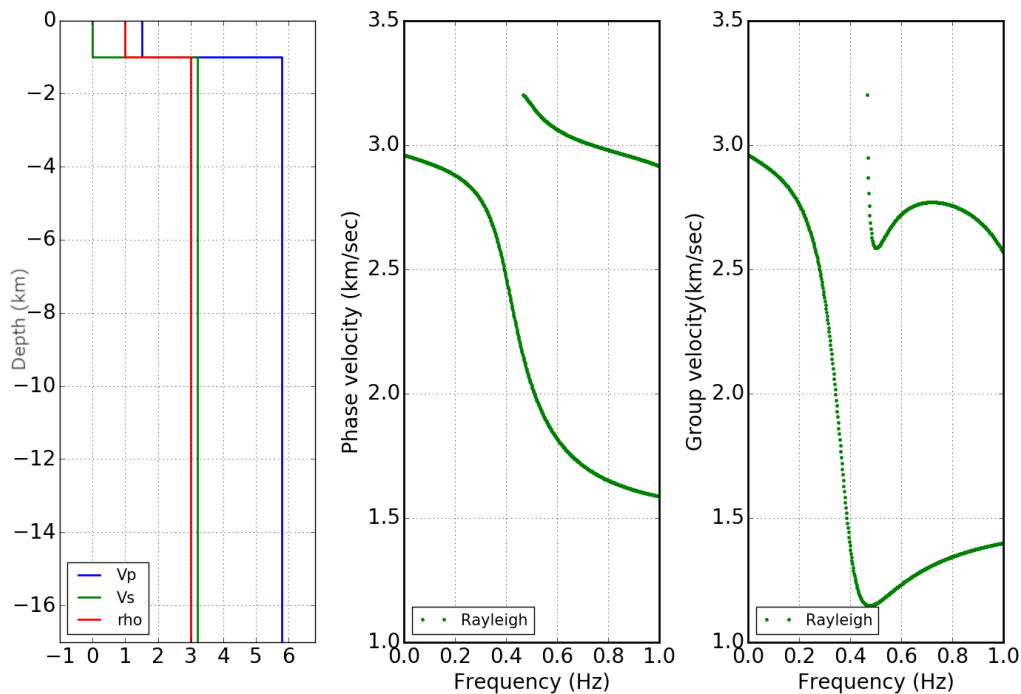


Figure 3.1 – Left: Oceanic model- V_p , V_s , density (ρ) vs depth representation for a two-layered model comprising of 1 km ocean and 16 km crust. Middle : Phase velocity as a function of frequency of Rayleigh waves for various modes (namely the fundamental and the first overtone) in the frequency band 0-1 Hz. Right: Group velocity as a function of frequency of Rayleigh waves for similar modes recorded in the frequency band 0-1 Hz.

3.1.1 Oceanic model: 1 km ocean and 16 km crust & Continental model: 17 km crust

We first consider a 1-D two-layer model consisting of 1 km thick ocean and 16 km thick crust. On the left in figure 3.1, the model is shown and the phase and group velocity obtained for the fundamental and first overtone of Rayleigh waves occupies the middle and right position respectively. For the fundamental mode of Rayleigh wave, the phase velocity varies from about 1.6 km/s to 2.9 km/s and between 2.9 km/s to 3.25 km/s for the first overtone. In this model, there exists zero Love wave mode.

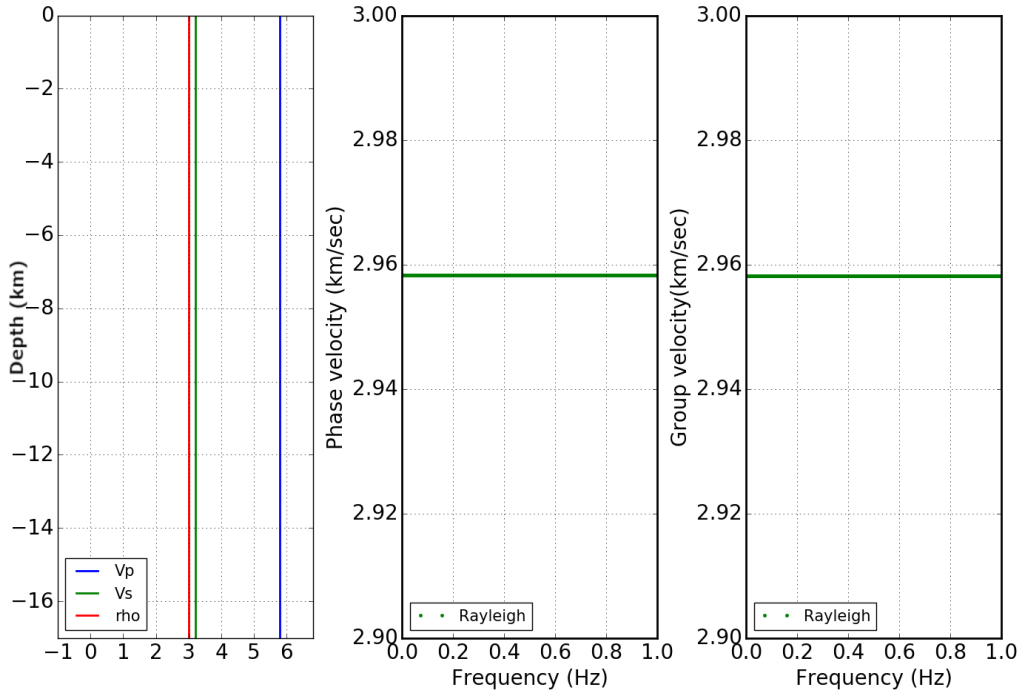


Figure 3.2 – Left: Continent model- V_p , V_s , ρ vs depth representation for a single layered model comprising of 17 km crust. Middle : Phase velocity as a function of frequency of fundamental mode of Rayleigh waves recorded in the frequency band 0-1 Hz. Right: Group velocity as a function of frequency of fundamental mode of Rayleigh waves recorded in the frequency band 0-1 Hz.

The synthetic seismograms are obtained using an explosive source located 0.1 km below the ocean surface recorded by receiver located at a distance of 120 km and 0.1 km below the crust upper limit respectively. The Z and R components of the fundamental mode and the first overtone for the oceanic model (Figure 3.1) are shown in figure 3.3. The total seismogram is computed as the superposition of the two modes. We see from their amplitude spectrum, the dominance of fundamental mode of Rayleigh waves for frequencies below 0.5 Hz. The first overtone starts to have amplitude at frequencies greater than 0.5 Hz where we record the amplitude due to the interference of the two modes. In general, the amplitude decreases at higher frequencies.

The phase and group velocity dispersion for the 1-D continental model comprising of 17 km crust is shown in fig 3.2. We observe only fundamental mode of Rayleigh wave that has a constant phase and group velocity of magnitude 2.98 km/s in the frequency range 0-1 Hz.

For these two models, no Love waves can exist. This property will be used in the next chapter to identify the waves.

3.1.2 Oceanic model: 1 km ocean, 6 km crust and 10 km mantle & Continental model: 7 km crust and 10 km mantle

We now investigate a three-layered 1-D oceanic model comprising of 1 km ocean, 6 km crust and 10 km mantle. In figure 3.4, each group and phase velocity curve correspond to

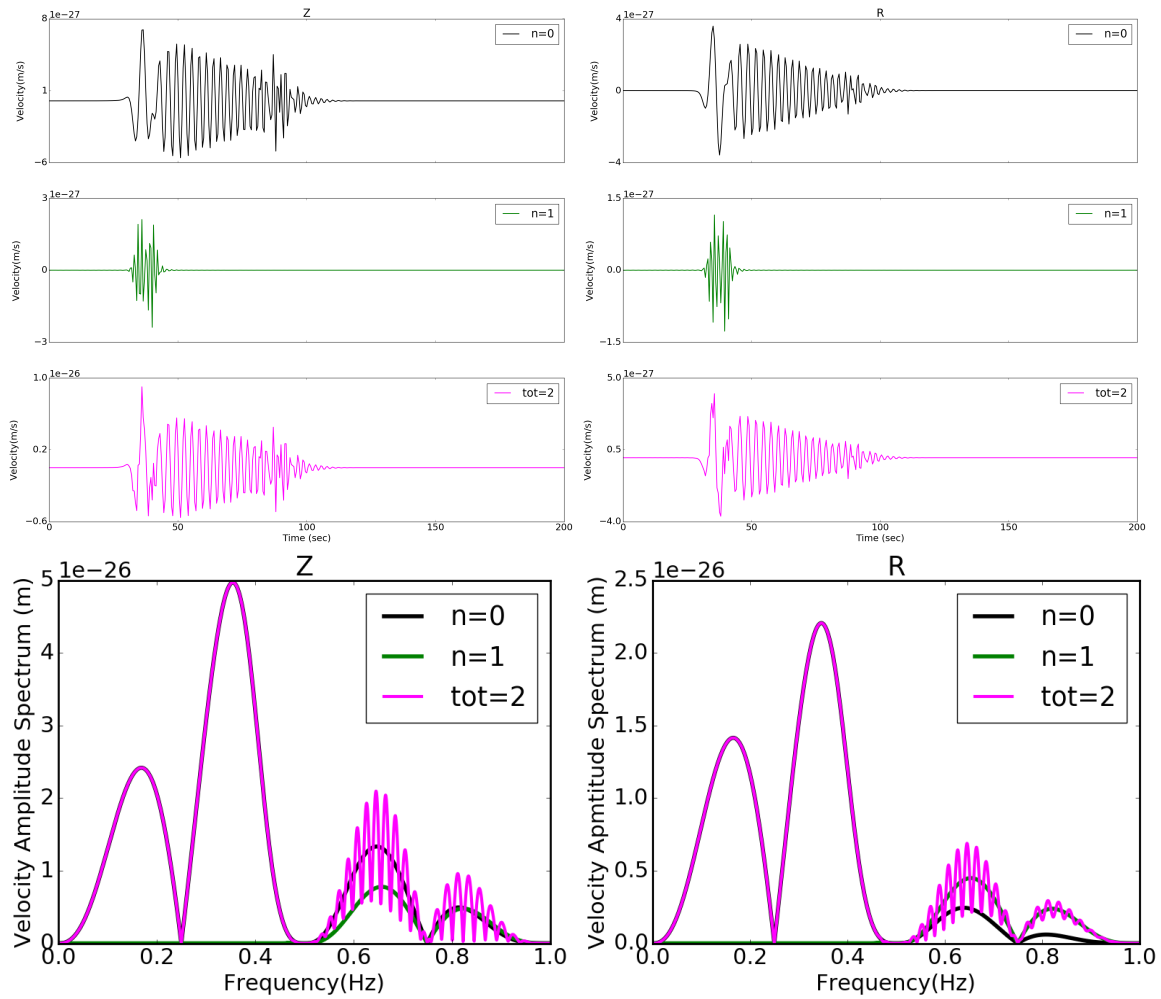


Figure 3.3 – Top: The Z and R components of seismic wavefield recorded at a receiver placed 0.1 km below the crust in an oceanic 1-D model shown in figure 3.1 (1 km ocean, 16 km crust). The source is an explosion located 0.1 km below the ocean surface. The waveforms for different modes ($n=0,1$) are superimposed to obtain total wave field (tot). Below: The Z and R amplitude spectrum of the different modes and the total wave field. For frequencies below 0.45 Hz, the fundamental mode of Rayleigh waves dominate whereas for higher frequencies, interference from the higher modes is observed.

the existing mode for this model. Primarily observed are the fundamental ($n=0$) mode, the first overtone ($n=1$), the second overtone ($n=2$) for both Rayleigh (green curves) and Love (blue curves) waves. We observe from the velocities that Love waves travel faster than Rayleigh waves. The higher modes are generated at frequencies greater than 0.3 Hz. The fundamental mode has lower velocity than the first and second overtone. In the frequency band 0-1 Hz, the phase velocity of fundamental Rayleigh and Love wave mode ranges from 1.6 km/s to 3.8 km/s and 3.25 km/s to 4.2 km/s respectively and the group velocity varies between 1.4-3.9 km/s and 3.2-4.2 km/s respectively. The phase velocity for the first overtone ranges from about 3.38 km/s to 4.2 km/s for the Rayleigh and Love waves and the second overtone has its phase velocity ranging between 3.78 km/s to 4.2 km/s.

For the continent model comprising of two-layers, 7 km crust and 10 km mantle shown in

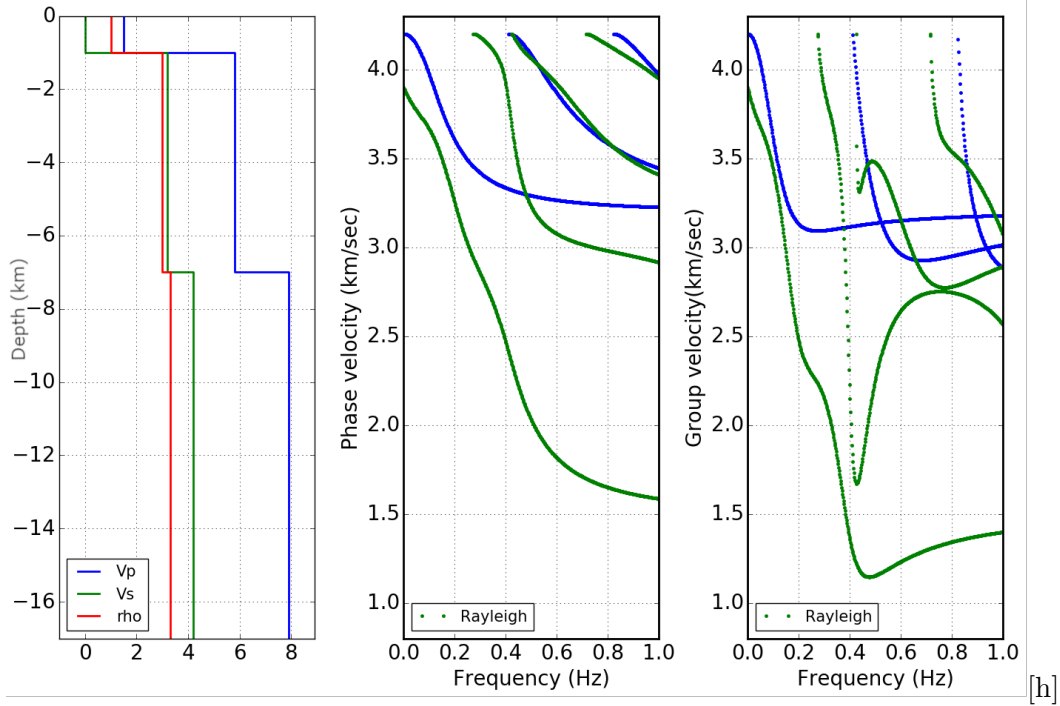


Figure 3.4 – Left: Oceanic model- V_p , V_s , ρ vs depth representation for a three-layered model comprising of 1 km ocean, 6 km crust and 10 km mantle. Middle : Phase velocity as a function of frequency of Rayleigh and Love waves for all modes (namely fundamental, first ,second and third overtone for Rayleigh waves and fundamental, first and second overtone for Love waves) in the frequency band 0-1 Hz. Right: Group velocity as a function of frequency of Rayleigh and Love waves for similar modes in the frequency band 0-1 Hz.

figure 2.5, the phase and group velocity are obtained for the fundamental, the first, second and third overtone of Rayleigh waves whereas only the fundamental, first and second overtone of Love waves are present in the frequency band 0-1 Hz. In this case, the fundamental mode of Rayleigh and Love waves show dispersion with phase velocity varying between 2.9-3.9 km/s and 3.21-4.2 km/s respectively. Similar to the oceanic model, the higher modes interfere above 0.3 Hz. The phase velocity of the first overtone changes from about 3.38 km/s to 4.2 km/s for both Rayleigh and Love waves and for the second overtone, the phase velocity has the values ranging from 3.78 km/s to 4.2 km/s.

We compute the synthetic seismograms for the oceanic model (model in Figure 3.4) using an explosion 0.1 km below the ocean surface and receiver at a distance of 120 km located 0.1 km below the sea floor (in the crustal layer) whereas for continent model in figure 3.5, the source (an explosion) and receiver both are placed 0.1 km below the crust upper limit at 120 km epicentral distance. For the 2 models, we show the Z and R components of the wave-field recorded for each mode and their amplitude spectrum in figure 3.6 and 3.7 respectively. For $f < 0.4$ Hz, the fundamental mode propagates with maximum amplitude and for $f > 0.4$ Hz, interference of higher modes is observed in the oceanic model (Figure 3.6). In the continent model, the fundamental model is dominant at all frequencies (Figure 3.7). The total waveform takes the shape of the fundamental mode in both the models. In the oceanic model, the spectrum shows negligible amplitude for higher modes below 0.2 Hz. However, for the continental model higher modes have negligible amplitude in the entire frequency range.

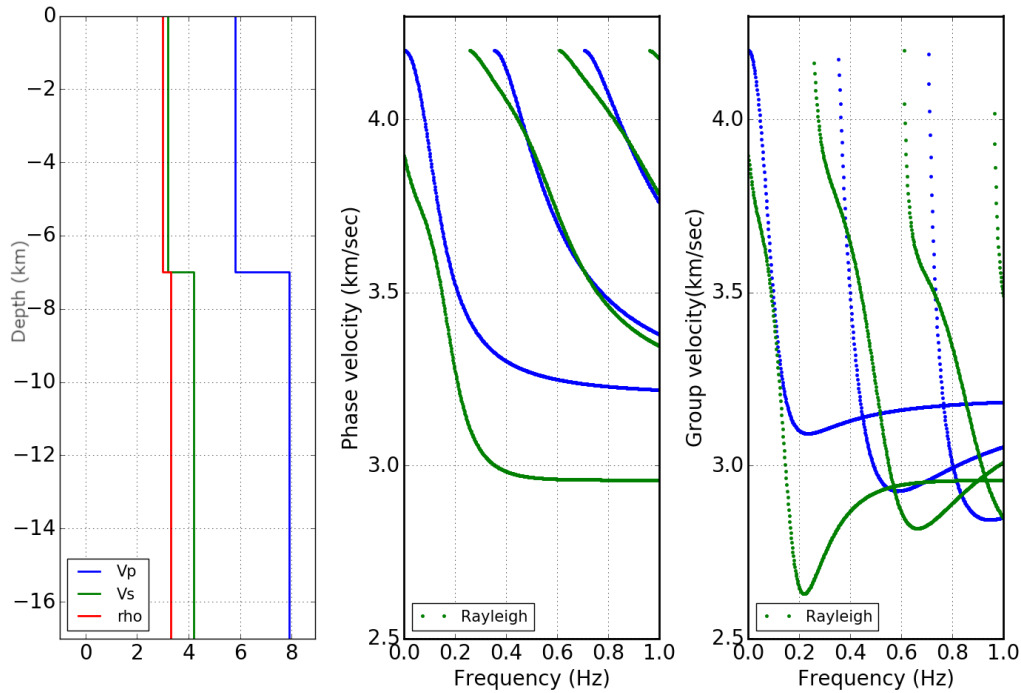


Figure 3.5 – Left: Continent model- V_p , V_s , ρ vs depth representation for a two-layered model comprising of 7 km crust and 10 km mantle. Middle : Phase velocity as a function of frequency of Rayleigh and Love waves for various modes (namely fundamental, first, second and third overtone for Rayleigh waves and fundamental, first and second overtone for Love waves) recorded in the frequency band 0-1 Hz. Right: Group velocity as a function of frequency of Rayleigh and Love waves for similar modes recorded in the frequency band 0-1 Hz.

The occurrence of higher modes at frequency higher than about 0.3 Hz for both Rayleigh and Love waves will help the interpretation of the 3D synthetic seismograms in the next chapter.

3.1.3 Oceanic model: 3 km ocean, 6 km crust and 10 km mantle & Continental model: 9 km crust and 10 km mantle

We are now interested in investigating 1-D modes in case of a deep ocean. A simple three-layered 1-D Earth model comprising of 3 km ocean, 6 km crust and 10 km mantle is considered. The model is shown in figure 3.8 and the phase and group velocity dispersion for the different modes within the frequency range 0-1 Hz are also obtained. In case of deep ocean, we observe the propagation of six modes (namely, the fundamental, the first, the second, the third, the fourth and the fifth overtones) of Rayleigh waves and three local Love waves modes (namely, the fundamental, the first and the second overtone). The fundamental mode of Rayleigh wave is the only Rayleigh mode at frequencies lower than 0.15 Hz. At $f > 0.15$ Hz, both fundamental and higher modes are observed. The phase velocity of the fundamental mode of Rayleigh waves ranges from about 1.5 km/s to 3.8 km/s whereas for the Love waves, it ranges between 3.25 km/s and 4.2 km/s.

In the continent model of 9 km crust and 10 km mantle represented in figure 3.9, the phase and group velocity dispersion are recorded for the fundamental and three overtones of Rayleigh and Love waves in the frequency band 0-1 Hz. The fundamental mode of

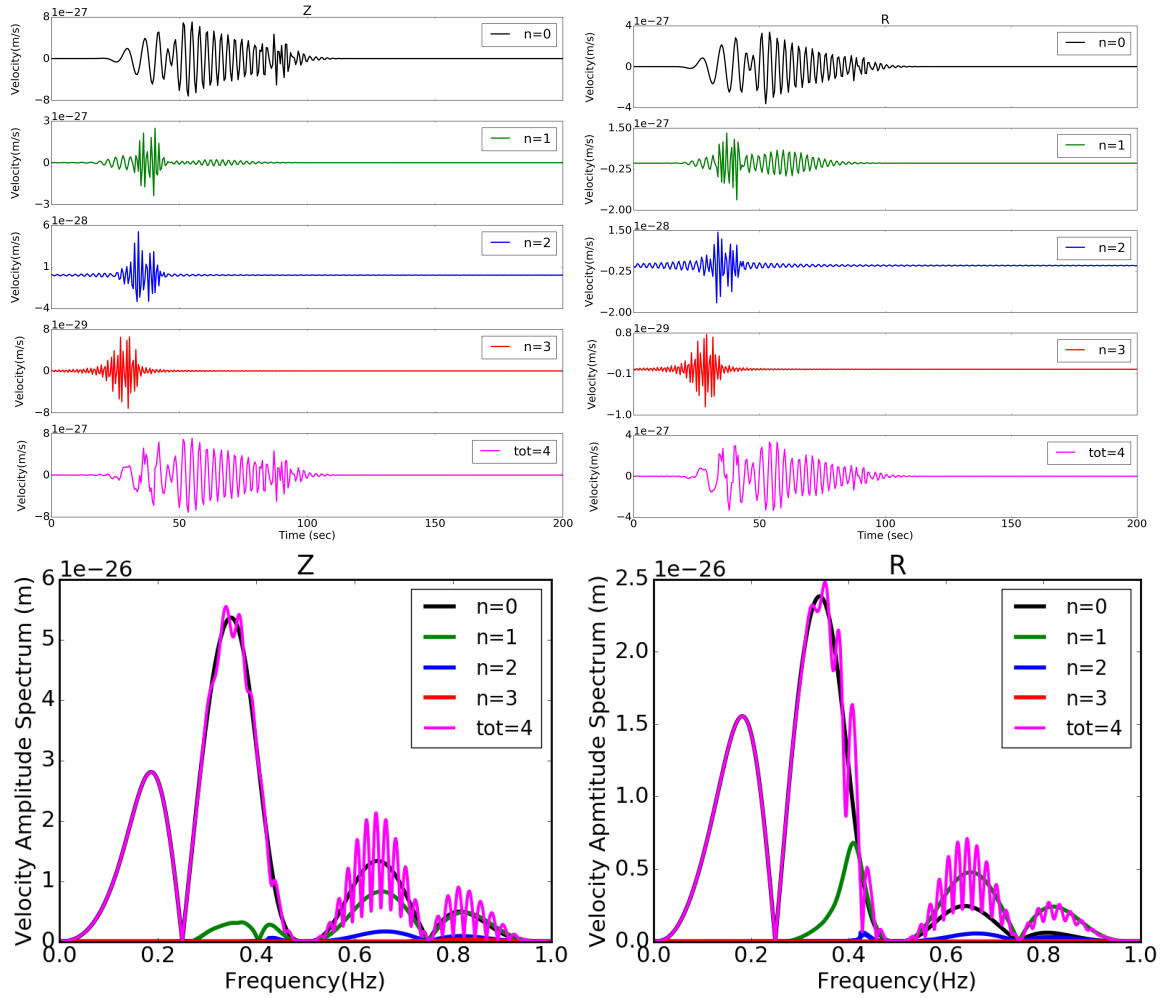


Figure 3.6 – Top: The Z and R components of seismic wavefield recorded at a receiver placed 0.1 km below the crust of an oceanic 1-D model shown in figure 3.4 (1 km ocean, 6 km crust, 10 km mantle). The waveforms for different modes ($n=0,1,2,3$) are superimposed to obtain total wave field (tot). Below: The Z and R amplitude spectrum of the different modes and the total wave field. For frequencies below 0.25 Hz, the fundamental mode of Rayleigh waves dominates whereas for higher frequencies, interference from the higher modes is observed.

Rayleigh and Love wave is the unique mode only for frequencies below 0.2 Hz. The higher modes appear at frequencies greater than 0.2 Hz. The phase velocity for the fundamental mode of Rayleigh and Love waves is scattered within 2.8 km/s to 3.9 km/s and 3.21 km/s to 4.2 km/s respectively.

Using similar source-receiver configuration as in section 2.1.2, the synthetic seismograms are computed. Figure 3.10 and 3.11 represent the Z and R components of the seismic velocity recorded for the 1-D model shown in figure 3.8 and 3.9 respectively. For the oceanic model, we observe higher amplitude of Z and R component in case of 3 km ocean model than 1 km. In figure 3.9, the total wavefield is predominantly fundamental Rayleigh waves as higher modes have negligible amplitude.

This section shows that for the oceanic model, increasing the ocean thickness, increases the number of modes and the resulting seismograms become more complex.

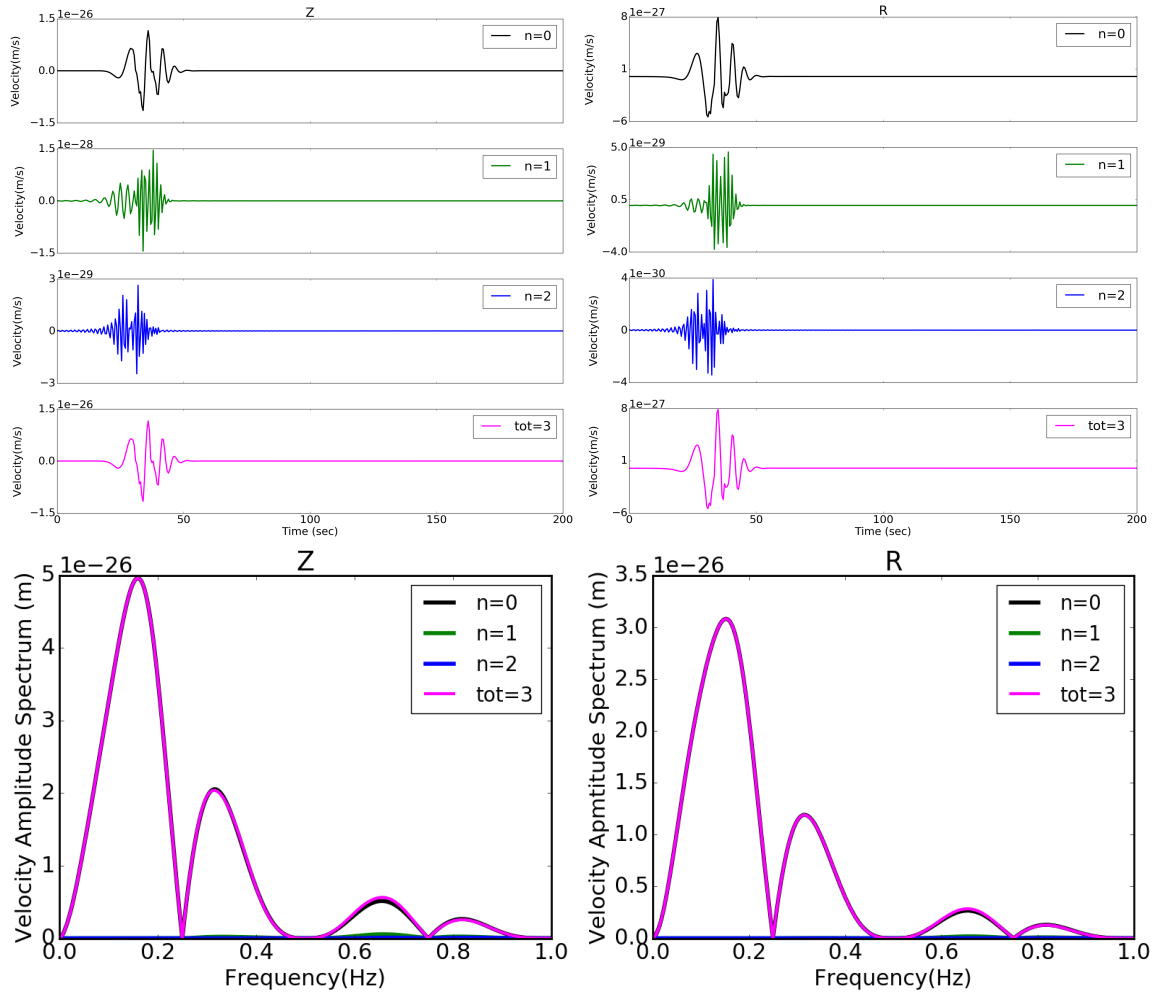


Figure 3.7 – Top: The Z and R components of seismic wavefield recorded at a receiver placed 0.1 km below the crust in the continental 1-D model shown in figure 3.5 (7 km crust, 10 km mantle). The waveforms for different modes ($n=0,1,2$) are superimposed to obtain total wave field (tot). Below: The Z and R amplitude spectrum of the different modes and the total wave field. The wavefield is predominantly fundamental mode of Rayleigh waves as higher modes have negligible amplitude.

3.1.4 Oceanic model: 6 km ocean, 6 km crust and 10 km mantle & Continental model: 12 km crust and 10 km mantle

For our last case, we consider a deeper oceanic model. In case of 1-D model made of 6 km ocean, 6 km crust and 10 km mantle as depicted in figure 3.12, the phase and group velocity dispersion are obtained for various modes of Rayleigh ($n=0,1,2,3,4,5,6,7,8,9$) and Love waves ($n=0,1,2$) within the frequency band 0-1 Hz. The higher modes of Rayleigh waves exists at frequencies above 0.75 Hz. The phase velocity of the Rayleigh wave fundamental mode varies between 1.5 km/s and 3.8 km/s and between 3.25 km/s - 4.2 km/s for Love waves.

Similarly, for the 1-D continent model, now with 12 km crust and 10 km mantle shown in figure 3.13, the group and phase velocity are obtained for the fundamental and higher overtones (the first, second, third and fourth) of Rayleigh and Love waves. The Z and R components of the synthetic seismograms for all the modes obtained for the oceanic model in figure 3.12 are plotted along with their amplitude spectrum in figure 3.14. Similarly to

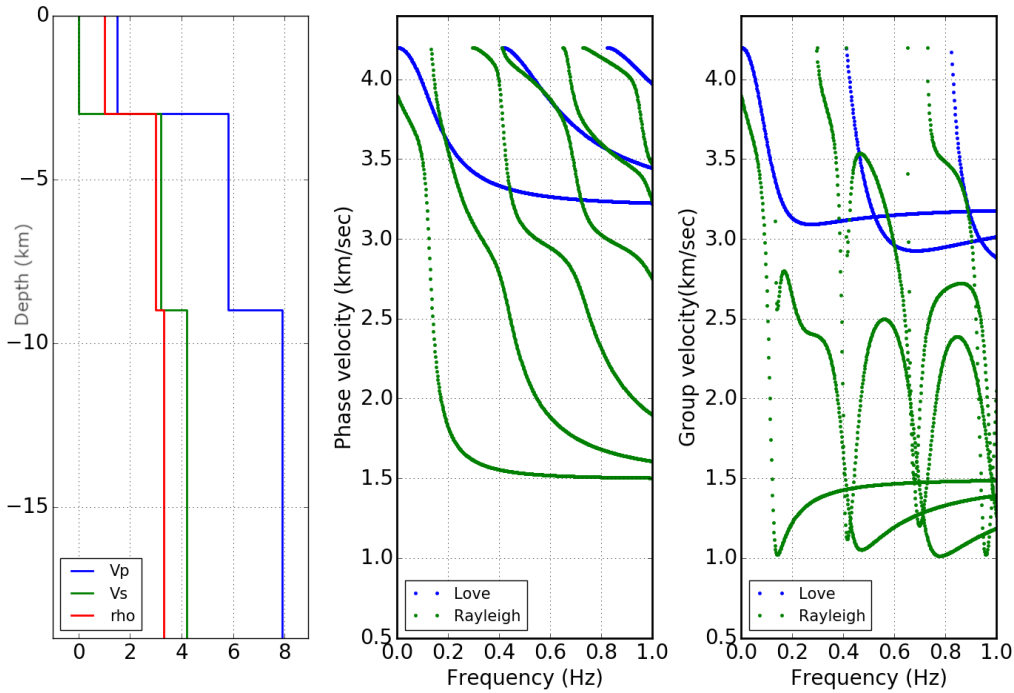


Figure 3.8 – Left: Oceanic model- V_p , V_s , ρ vs depth representation for a three-layered model comprising of 3 km ocean, 6 km crust and 10 km mantle. Middle : Phase velocity as a function of frequency of Rayleigh and Love waves for all modes (namely fundamental, first, second, third, fourth, fifth, sixth overtone for Rayleigh waves and fundamental, first and second overtone for Love waves) in the frequency band 0-1 Hz. Right: Group velocity as a function of frequency of Rayleigh and Love waves for similar modes in the frequency band 0-1 Hz.

previous section, the source is an explosion in the ocean located 0.1 km below the ocean surface and the receiver are placed 0.1 km below the ocean-crust interface. Due to 6 km ocean thickness and interference from the higher modes at $f < 0.05$ Hz, we observe lower amplitude of Z and R components as compared to 3 km ocean model. In case of continent model in figure 3.13, when the source (an explosion) and receiver are placed 0.1 km below the crust upper limit and the epicentral distance is 120 km, the Z and R components shown in figure 3.15 depict the dominance of fundamental mode for the entire frequency band.

In summary, when the ocean is 6 km thick, the waveforms become more complex and of smaller amplitude with respect to previous cases (thinner ocean layer).

3.1.5 Oceanic model: 6 km ocean, 3 km sediments, 6 km crust and 7 km mantle

As we have observed different modes and their relative amplitude in 1-D models of varying ocean and crustal thickness, we are also interested in understanding the effect of sediments on the mode propagation. Lastly, we present a 1-D model comprising of 6 km ocean, 3 km sediments, 6 km crust and 7 km mantle shown in figure 3.16. The phase and group velocity dispersion curves show the presence of eleven modes of Rayleigh and Love waves in the frequency band between 0-1 Hz. We observe from these curves that Love wave modes are the first arrivals in this frequency band. The fundamental mode of Love wave appears at

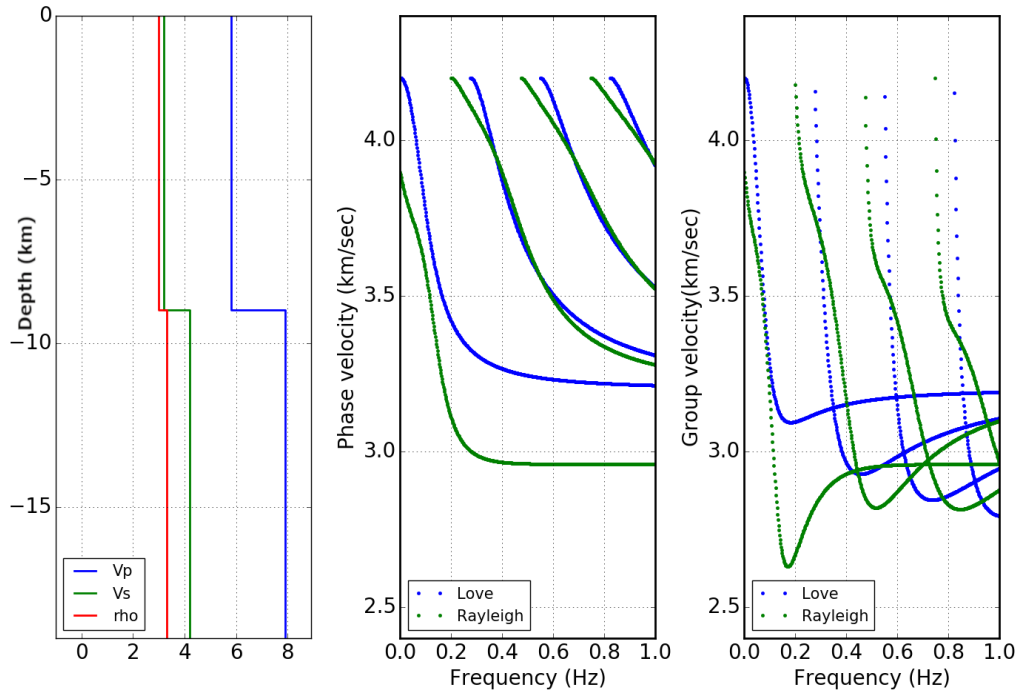


Figure 3.9 – Left: Continent model- V_p , V_s , ρ vs depth representation for a two-layered model comprising of 9 km crust and 10 km mantle. Middle : Phase velocity as a function of frequency of Rayleigh and Love waves for various modes (namely fundamental, first, second, third and fourth overtone for Rayleigh waves and fundamental, first, second and third overtone for Love waves) recorded in the frequency band 0-1 Hz. Right: Group velocity as a function of frequency of Rayleigh and Love waves for similar modes recorded in the frequency band 0-1 Hz.

lower frequency than the Rayleigh wave mode. For $f > 0.05$ Hz, there is interference of higher modes. The synthetic seismograms are computed using an explosion 0.1 km below the ocean surface and a receiver located 0.1 km below the sediments-crust interface. The source-receiver distance is 120 km. The Z and R velocity components of the synthetic seismograms are displayed in figure 3.17 corresponding to the different modes. As an effect of sediments, the total energy observed on the Z and R components is greater than the energy recorded in figure 3.14 for the 6 km ocean model without sediments.

We will use the above analysis for understanding the propagation of Rayleigh and Love waves in a 3-D media which will be discussed in the following chapter.

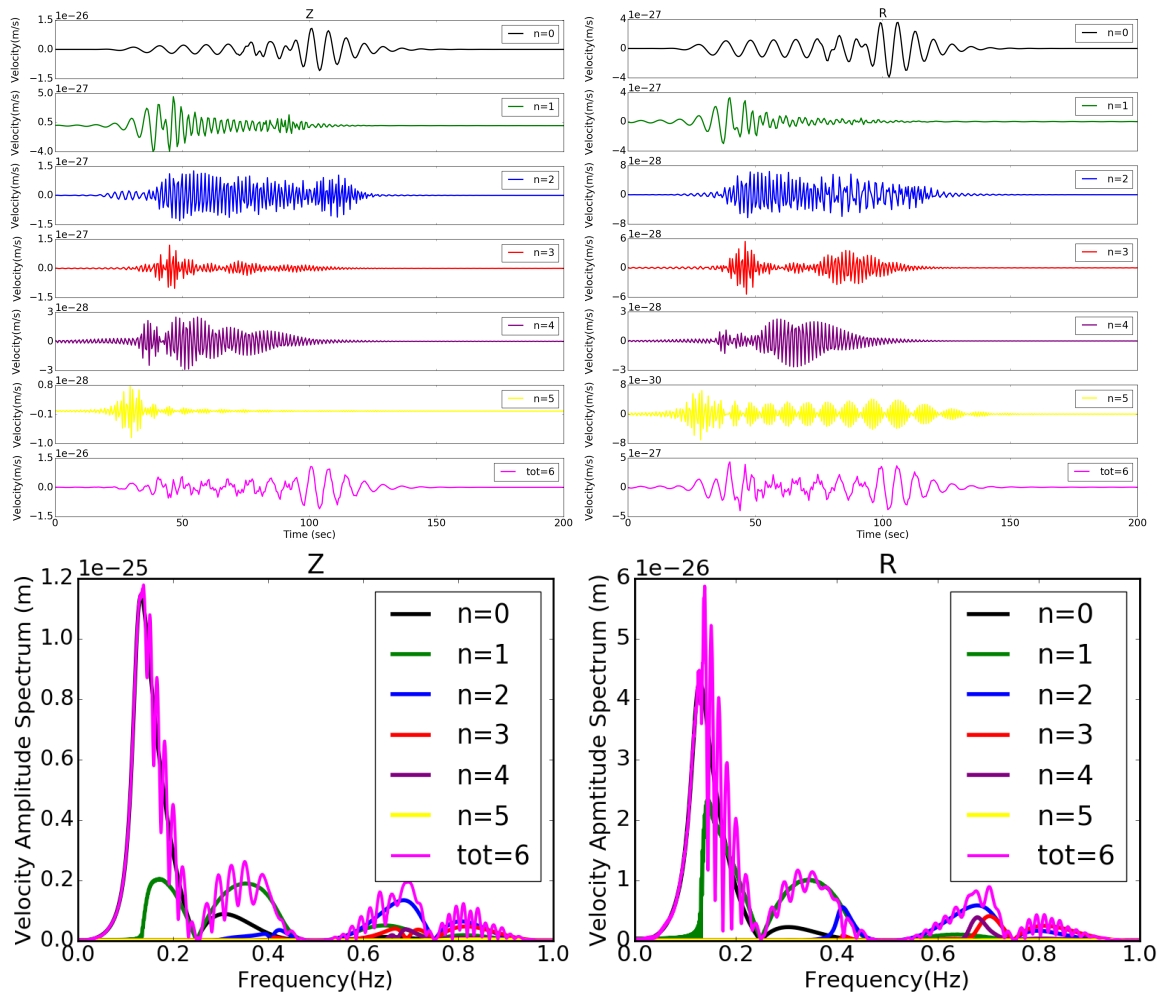


Figure 3.10 – Top: The Z and R components of seismic wavefield recorded at a receiver placed 0.1 km below the crust in the oceanic 1-D model shown in figure 3.8 (3 km ocean, 6 km crust and 10 km mantle). The waveforms for different modes ($n=0,1,2,3,4,5$) are superimposed to obtain total wave field (tot). Below: The Z and R amplitude spectrum of the different modes and the total wave field. For frequencies below 0.15 Hz, the fundamental mode of Rayleigh waves dominate whereas for higher frequencies, interference from the higher modes is observed.

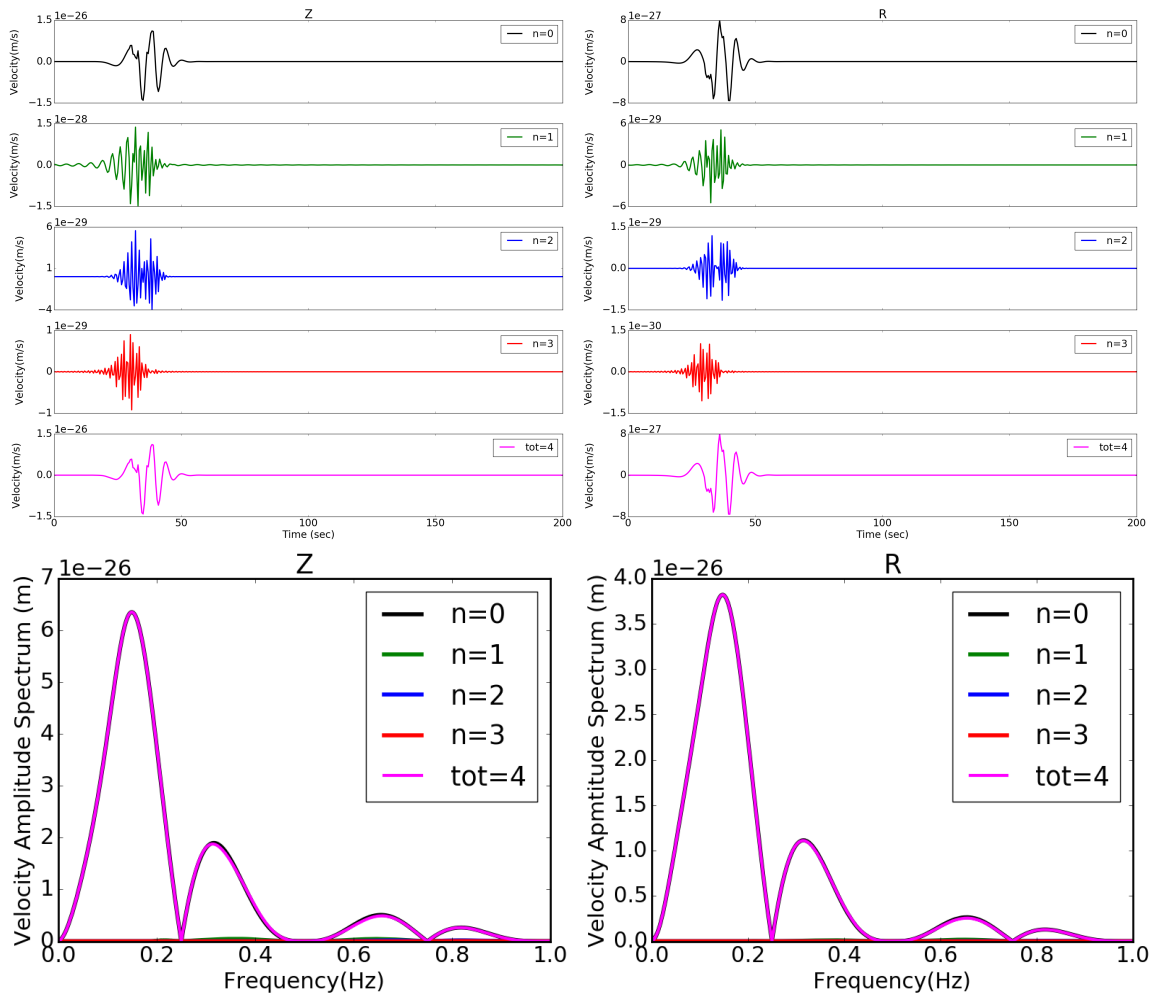


Figure 3.11 – Top: The Z and R components of seismic wavefield recorded at a receiver placed 0.1 km below the crust in the continental 1-D model shown in figure 3.9 (9 km crust, 10 km mantle). The waveforms for different modes ($n=0,1,2,3$) are superimposed to obtain total wave field (tot). Below: The Z and R amplitude spectrum of the different modes and the total wave field. The wavefield is predominantly fundamental mode of Rayleigh waves as higher modes have negligible amplitude.

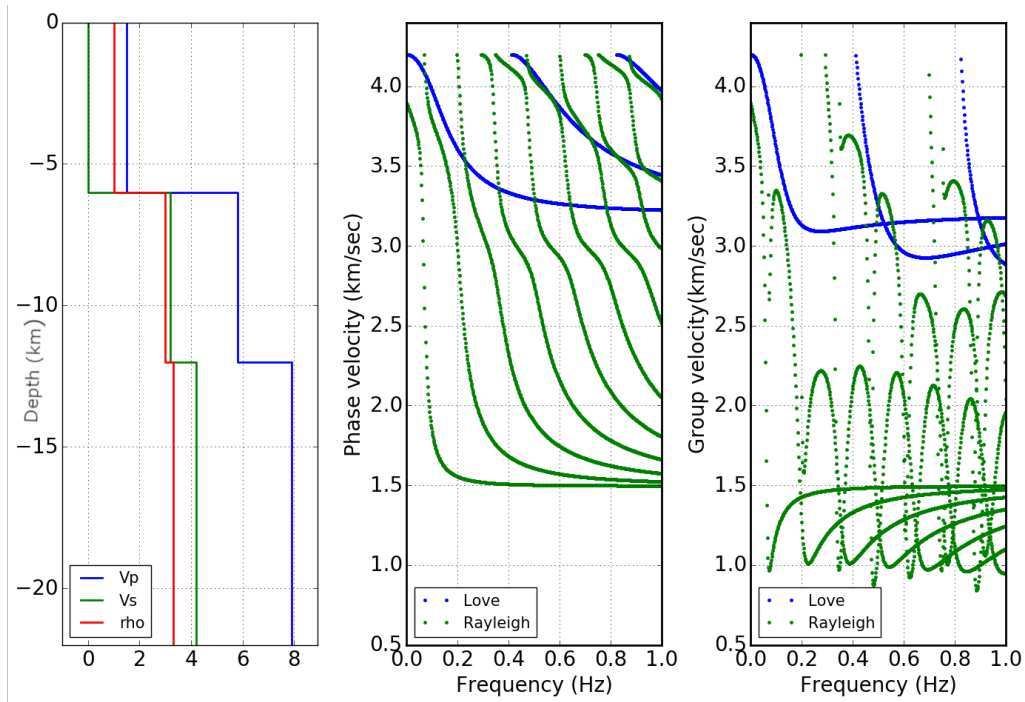


Figure 3.12 – Left: Oceanic model- V_p , V_s , ρ vs depth representation for a three-layered model comprising of 6 km ocean, 6 km crust and 10 km mantle. Middle : Phase velocity as a function of frequency of Rayleigh and Love waves for various modes in the frequency band 0-1 Hz. Right: Group velocity as a function of frequency of Rayleigh and Love waves for similar modes in the frequency band 0-1 Hz.

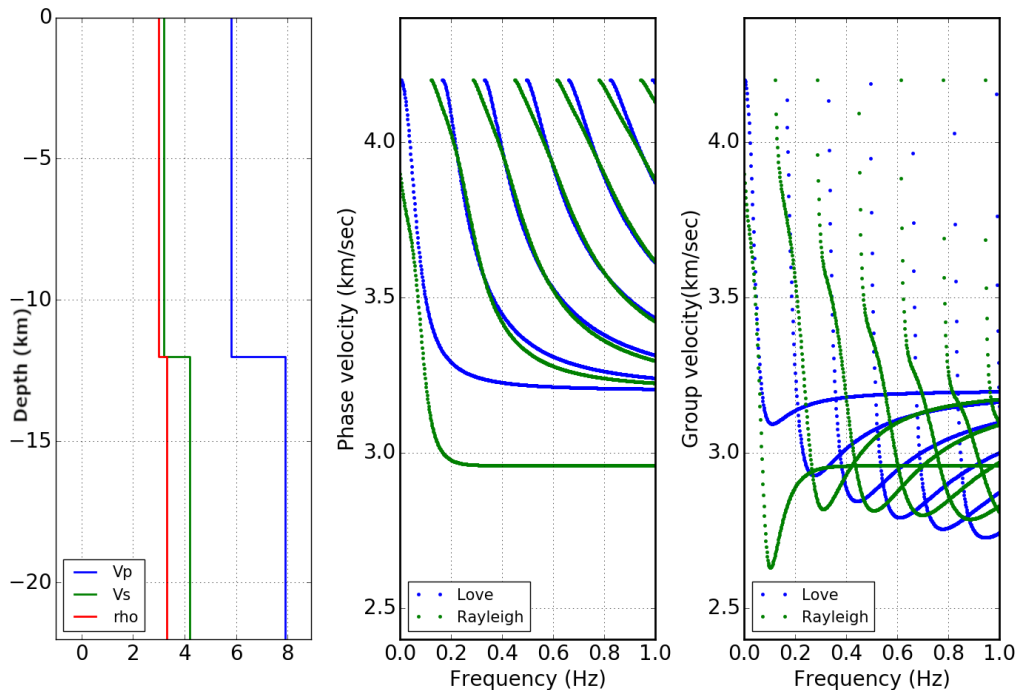


Figure 3.13 – Left: Continent model- V_p , V_s , ρ vs depth representation for a two-layered model comprising of 12 km crust and 10 km mantle. Middle : Phase velocity as a function of frequency of Rayleigh and Love waves for various modes recorded in the frequency band 0-1 Hz. Right: Group velocity as a function of frequency of Rayleigh and Love waves for similar modes recorded in the frequency band 0-1 Hz.

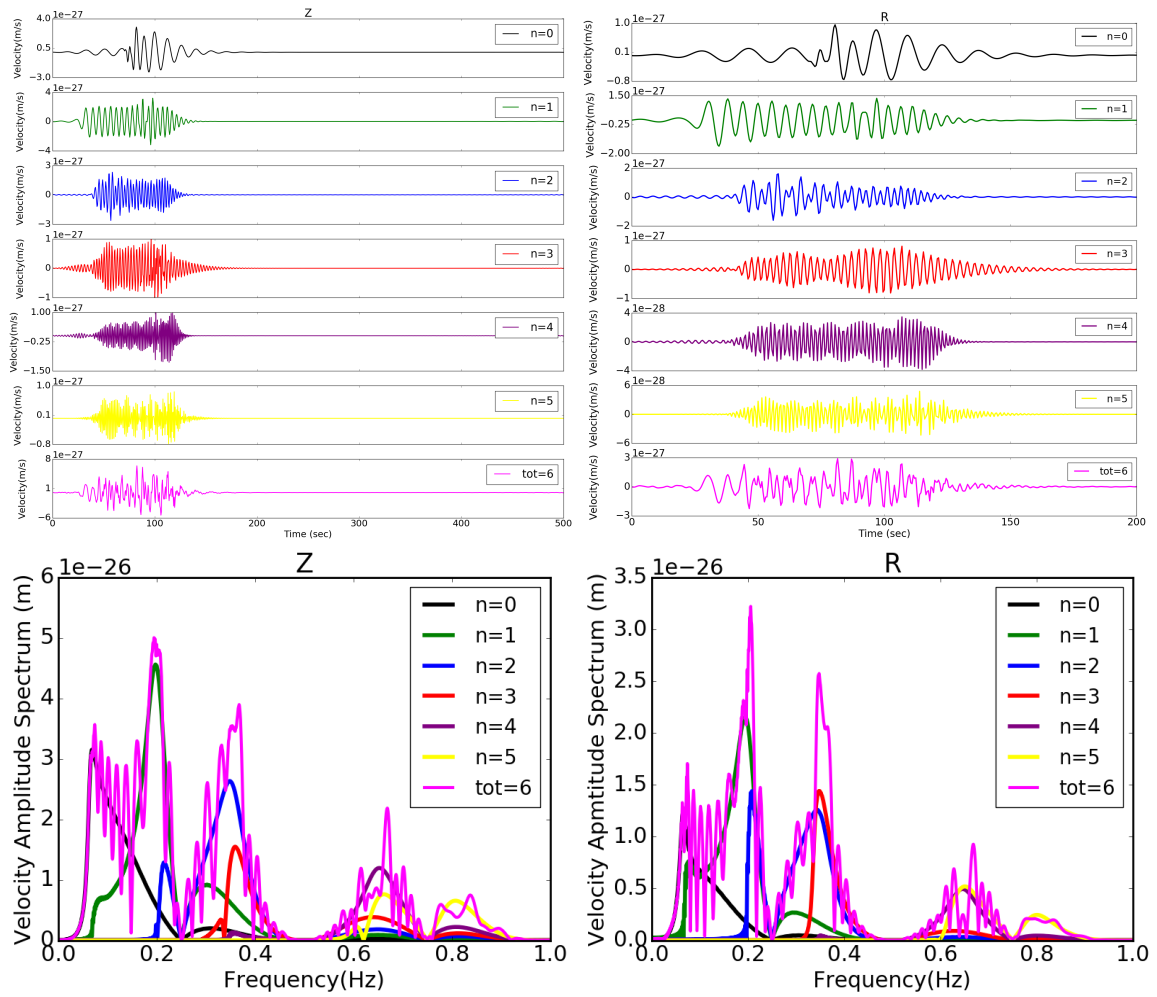


Figure 3.14 – Top: The Z and R components of seismic wavefield recorded at a receiver placed 0.1 km below the crust in the oceanic 1-D model shown in figure 3.12 (6 km ocean, 6 km crust, 10 km mantle). The waveforms for different modes ($n=0,1,2,3,4,5$) are superimposed to obtain total wave field (tot). Below: The Z and R amplitude spectrum of the different modes and the total wave field. For frequencies below 0.05 Hz, the fundamental mode of Rayleigh waves dominate whereas for higher frequencies, interference from the higher modes is observed.

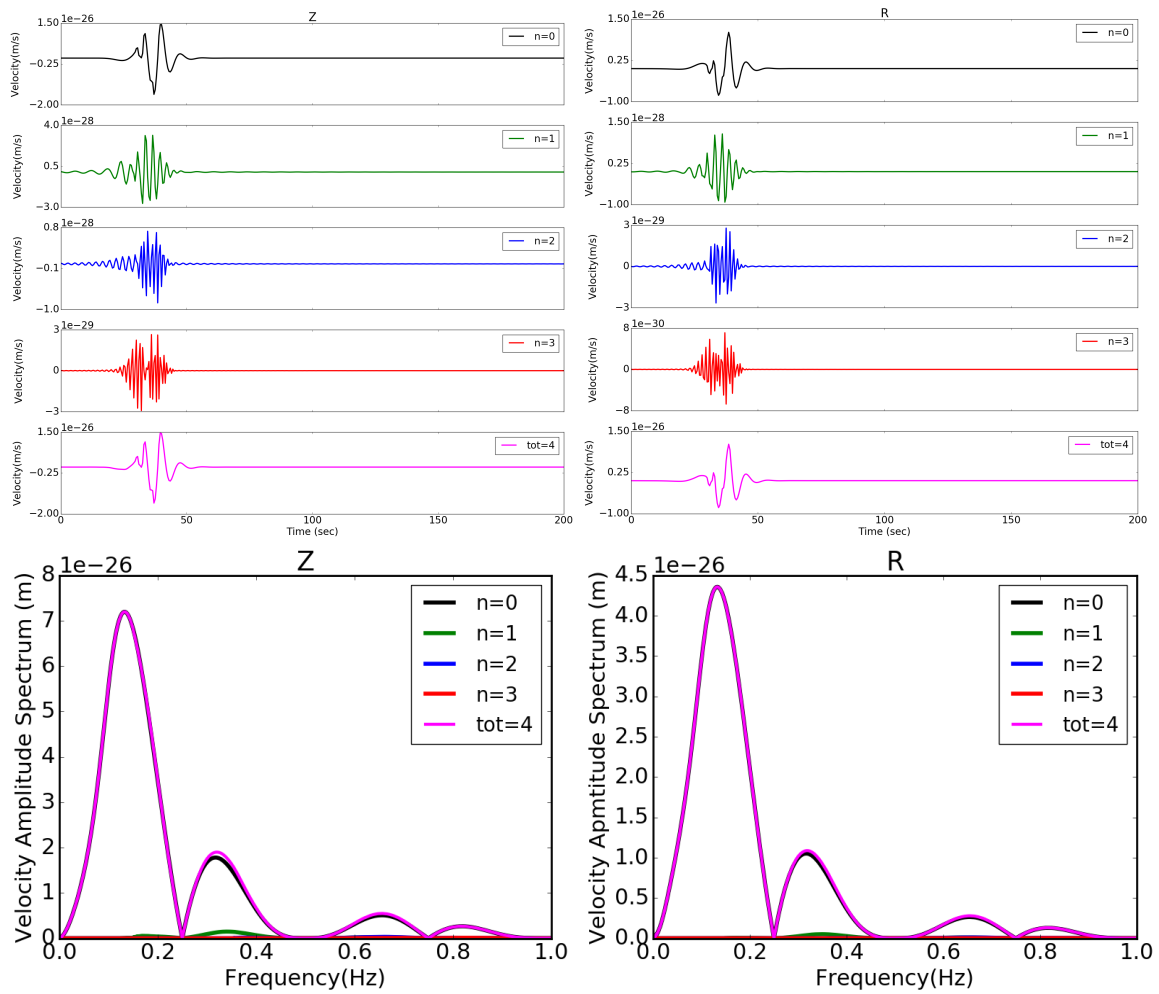


Figure 3.15 – Top: The Z and R components of seismic wavefield recorded at a receiver placed 0.1 km below the crust in the continental 1-D model shown in figure 3.13 (12 km ocean and 10 km mantle). The waveforms for different modes ($n=0,1,2,3$) are superimposed to obtain total wave field (tot). Below: The Z and R amplitude spectrum of the different modes and the total wave field. The wavefield is predominantly fundamental mode of Rayleigh waves as higher modes have negligible amplitude.

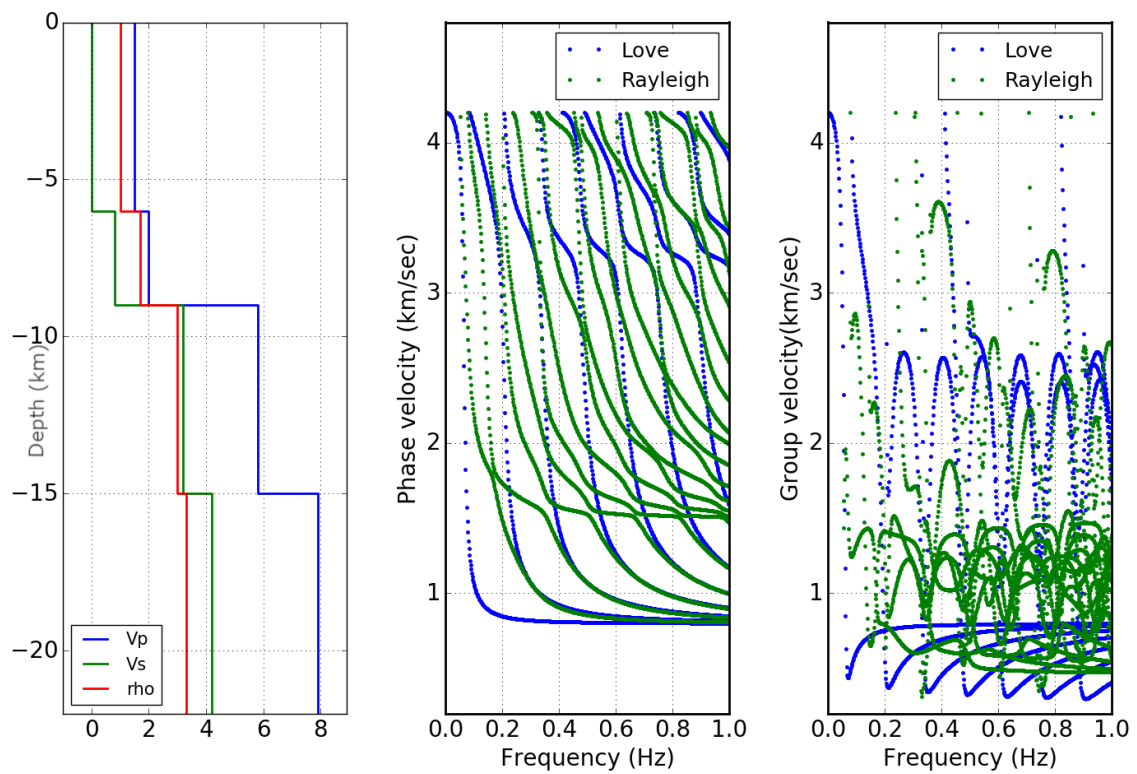


Figure 3.16 – Left: Oceanic model- V_p , V_s , ρ vs depth representation for a three-layered model comprising of 6 km ocean, 3 km sediments, 6 km crust and 7 km mantle. Middle : Phase velocity as a function of frequency of Rayleigh and Love waves for ten modes in the frequency band 0-1 Hz. Right: Group velocity as a function of frequency of Rayleigh and Love waves for similar modes in the frequency band 0-1 Hz.

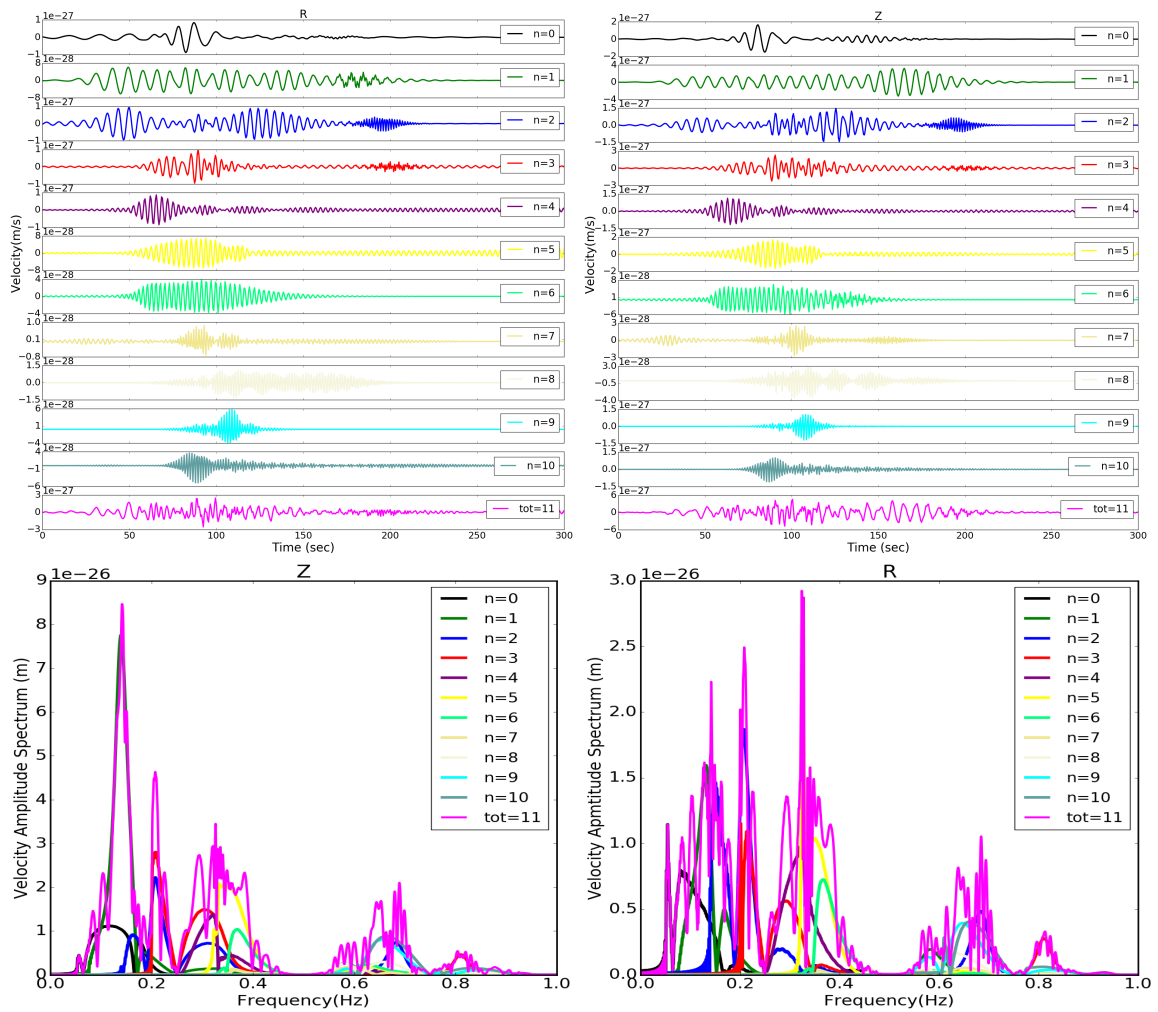


Figure 3.17 – Top: The Z and R components of seismic wavefield recorded at a receiver placed 0.1 km below the sediment-crust interface in the oceanic 1-D model shown in figure 3.16 (6 km ocean, 3 km sediments, 6 km crust and 7 km mantle). The waveforms for different modes ($n=0$ to 10) are superimposed to obtain total wave field (tot). Below: The Z and R amplitude spectrum of the different modes and the total wave field. The wavefield is predominantly fundamental mode of Rayleigh waves as higher modes have negligible amplitude.

Chapter 4

Modeling the effect of ocean-continent slope on Secondary microseisms

4.1	Effect of ocean thickness	62
4.1.1	Models Setup	62
4.1.2	Seismic wavefield for model I (1 km ocean, crust)	64
4.1.3	Seismic wavefield for model II (1 km ocean, crust and mantle) ...	72
4.1.4	Seismic wavefield for model III (3 km ocean, crust and mantle)...	80
4.1.5	Seismic wavefield for model IV (6 km ocean, crust and mantle) ..	82
4.2	Effect of sediments	85
4.2.1	Seismic wavefield for model V (6 km ocean, sediments, crust, mantle)	85
4.3	Effect of the ocean-continent slope	91
4.3.1	Seismic wavefield for model VI (3 km ocean, crust, mantle) slope 10°	91
4.4	Results summary	95

Let's summarize briefly the principal points and conclusion discussed in the previous chapters. In chapter 1, we have seen various data-oriented studies resulting in the observation of secondary microseism Love waves that lack complete understanding of its origin. In chapter 3, we have shown the modeling for simple 1-D Earth structures of the modes of Rayleigh and Love waves that exist in the oceanic and the continental models, and their relative amplitude. The main advantage of this analysis is that it constitutes a fundamental basis to understand wave field in 3D models. To broaden the domain of understanding, we now propose to study the effect of the presence of ocean-continent boundary on the seismic wave field generated from secondary microseisms noise sources. In order to do that, we apply 3D spectral element method to model the effect of ocean-continent boundary on Love/Rayleigh wave ratio and quantify it using different sources and model parameters. For this purpose, we evaluate the relative change in the amplitude of the seismic wave field on the different components recorded on the continent and the existence of Love waves due to the effect of 1) varying ocean thickness, 2) the source-site effect, 3) the presence of sediments below the ocean floor, 4) the varying ocean-continent slope angle.

4.1 Effect of ocean thickness

4.1.1 Models Setup

Before we begin analyzing the seismic wavefield generated in a 3D medium, here we focus on the description of the models used in order to perform simulations with the SEM. The different 3D models are summarized in table 1. As explained in chapter 1 (section 1.5.2), in order to apply the spectral element method, a mesh is first created depending on the properties of waves that propagate through the medium. For mesh designing, the element size is simply determined using the relation stated in Section 1.5.2 and the corresponding time step for wave field computation is constrained using the CFL condition. Thus, the element size of the mesh is 1 km. The construction of the mesh is done using the meshing tool Trelis.

For our study, we first consider the Earth model (model I) shown in figure 4.1 in which no Love waves can be generated. Indeed, we have seen with the modeling in 1D media that no Love wave are generated when the oceanic model is made of ocean and crust layers only and the continental model is just a crust layer (Fig 3.1 and 3.2). We begin investigating the seismic wave field in a model with a thin ocean layer. Therefore we build model I as 1 km thick ocean overlying 16 km of crust on the oceanic side and 17 km thick crust on the continental side (section 4.1.2).

The volume of the mesh is restricted to 210 km x 210 km x 17 km. The ocean-continent boundary is a sloping surface making an angle of 32° with the horizontal X-axis. We associate our model with the characteristic elastic properties of P and S waves propagating in the ocean and the crust, summarized in table 4.2. These values will be used for all the models. For wavefield computation, we put an explosion of frequency 0.05-1 Hz and magnitude $1^{20}N$, at a depth of 1 m below the free ocean surface close to the ocean-continent slope (indicated as S2 in figure 4.1b). The receivers are aligned on the continent parallel to the ocean-continent boundary at an increasing source-receiver azimuth (0 to 42.27°) as well as distance increasing from 90 km to 134 km (represented by a yellow line

Models			
Model number	Oceanic side	Continental side	Ocean-continent slope angle
Model I	1 km ocean, 16 km crust	17 km crust	32°
Effect of ocean thickness			
Model II	1 km ocean, 6 km crust, 10 km mantle	7 km crust, 10 km mantle	32°
Model III	3 km ocean, 6 km crust, 10 km mantle	9 km crust, 10 km mantle	32°
Model IV	6 km ocean, 6 km crust, 10 km mantle	12 km crust, 10 km mantle	32°
Effect of sediments			
Model V	6 km ocean, 3 km sediments, 6 km crust, 7 km mantle	15 km crust, 7 km mantle	32°
Effect of Ocean-continent slope angle			
Model VI	3 km ocean, 6 km crust, 10 km mantle	9 km crust, 10 km mantle	10°

Table 4.1 – Different 3D model configurations used in this study to model the effect of ocean-continent slope on the transverse energy using both a source close and far from the ocean-continent boundary.

in figure 4.1b, see Appendix for the coordinates). They are placed in the crust at a depth of 1 m below the surface.

We then consider a model in which Love waves can exist. We have shown through 1D modeling that Love waves can exist in oceanic models that contains ocean, crust and mantle layers (Figure 3.4) and in continental models that contains a crust and a mantle layer (Figure 3.5). Therefore, we build model II by adding one bottom layer to model I as depicted in figure 4.2. The oceanic part of model II now has three layers: 1 km ocean, 6 km crust and 10 km mantle and two layers in the continental part: 7 km crust and 10 km mantle. The horizontal dimensions of the mesh and ocean-continent slope angle is same as in model I. The added mantle layer has elastic properties of P and S waves listed in table 4.2.

The source location has a significant affect on the seismic noise amplitude. We investigate the source site effect in model II by considering two separate sources 1) a source close to the ocean continental boundary (indicated as S2 in figure 4.2b) with same source-receiver configuration as in model I; 2) a source far-away from the ocean-continent boundary (S1) as represented in figure 4.2.

We then evaluate the effect of ocean thickness on the seismic wave field, in order to do that, we build 3D models with thicker oceans (3 km and 6 km). The third model (model III) consists of three homogeneous layers : 3 km thick ocean, 6 km crust and 10 km mantle on the oceanic side and two layers: 9 km crust and 10 km mantle on the continent side. Accordingly the mesh volume now becomes 210 km x 210 km x 19 km. The slope angle is kept constant (32°). We investigate the seismic wave field in model III due to a close

Layer	Density	P-wave velocity	S-wave velocity
Ocean	$\rho_w = 1.0g/cm^3$	$\alpha_w = 1.5km/s$	$\beta_w = 0$
Crust	$\rho_c = 3g/cm^3$	$\alpha_c = 5.8km/s$	$\beta_c = 3.2km/s$
Mantle	$\rho_m = 3.4g/cm^3$	$\alpha_m = 8km/s$	$\beta_m = 4.1km/s$

Table 4.2 – Density and body wave speeds in the ocean and crust layer

source and far source in section 4.1.4 using the same source-receiver configuration as in model II.

For the case of 6 km deep ocean (model IV), the three layers in the oceanic part are 6 km ocean, 6 km crust and 10 km mantle. The continental part of the model has 12 km crust and 10 km mantle. The horizontal dimensions of the model remain same as in model II, only the vertical dimension increases to 22 km. Using the same source as in model II, the source site effect for model IV is investigated in sections 4.1.5 for close source and far source.

The seismic wavefield for each model is analyzed in the following sections. We compare the amplitudes of the vertical and horizontal components that allow us to evaluate the amount of conversion of incident energy into energy on the transverse component. Further, we do polarization analysis to decipher the characteristic of the seismic wave field.

4.1.2 Seismic wavefield for model I (1 km ocean, crust)

The seismic wave field simulated for the model setup I is analyzed in this section.

The three-component seismic wavefield in velocity is shown in figure 4.3a, 4.3b, 4.3c for the Z , R and T component of the seismic velocity respectively, recorded at all stations arranged in the order of increasing Y coordinate of the station. The rotation of the components is done following the direction convention indicated in Fig 4.3d (R in the direction of propagation path: T perpendicular to R). The elliptical polarization between Z and R (Fig 4.4) demonstrates that the wavefield propagates predominantly as Rayleigh wave. Focusing on the T component, we record non-zero seismic wavefield (figure 4.3c). Considering that in both the oceanic and continental part of the model, there exists no Love wave modes as demonstrated in the previous chapter, considering a 1D model (figure 3.1 and 3.2), therefore the signal on the T component cannot be Love waves.

The amplitude spectrum of the 3-components v_R, v_Z & v_T are plotted for the receivers indicated as A, B, C, D, E & F in figure 4.5, exhibit the occurrence of two peaks at frequencies, 0.4 Hz and 0.8 Hz and the spectrum amplitude remains of similar amplitude on the Z and R components at all stations. However the amplitude on the T component shows an increase with the increasing source-receiver azimuth and longer distance. The 1 D synthetics model analysis showed that for $f < 0.4$ Hz, the wave field propagates as a fundamental mode only whereas for $f > 0.4$ Hz, it propagates as a mixture of fundamental and first overtone of Rayleigh waves in the oceanic model (Figure 3.1 and 3.3 for the 1D oceanic model and as a fundamental mode on the continent (Figure 3.2 for the 1D continent model). Therefore, at the ocean-continent interface, the fundamental mode is transmitted as fundamental mode and the first overtone is converted to fundamental mode. The particle motion on the T and R components for these stations is analyzed in figure 4.6 and 4.7 in the frequency band 0.1-0.15 Hz and 0-1 Hz respectively. The only waves

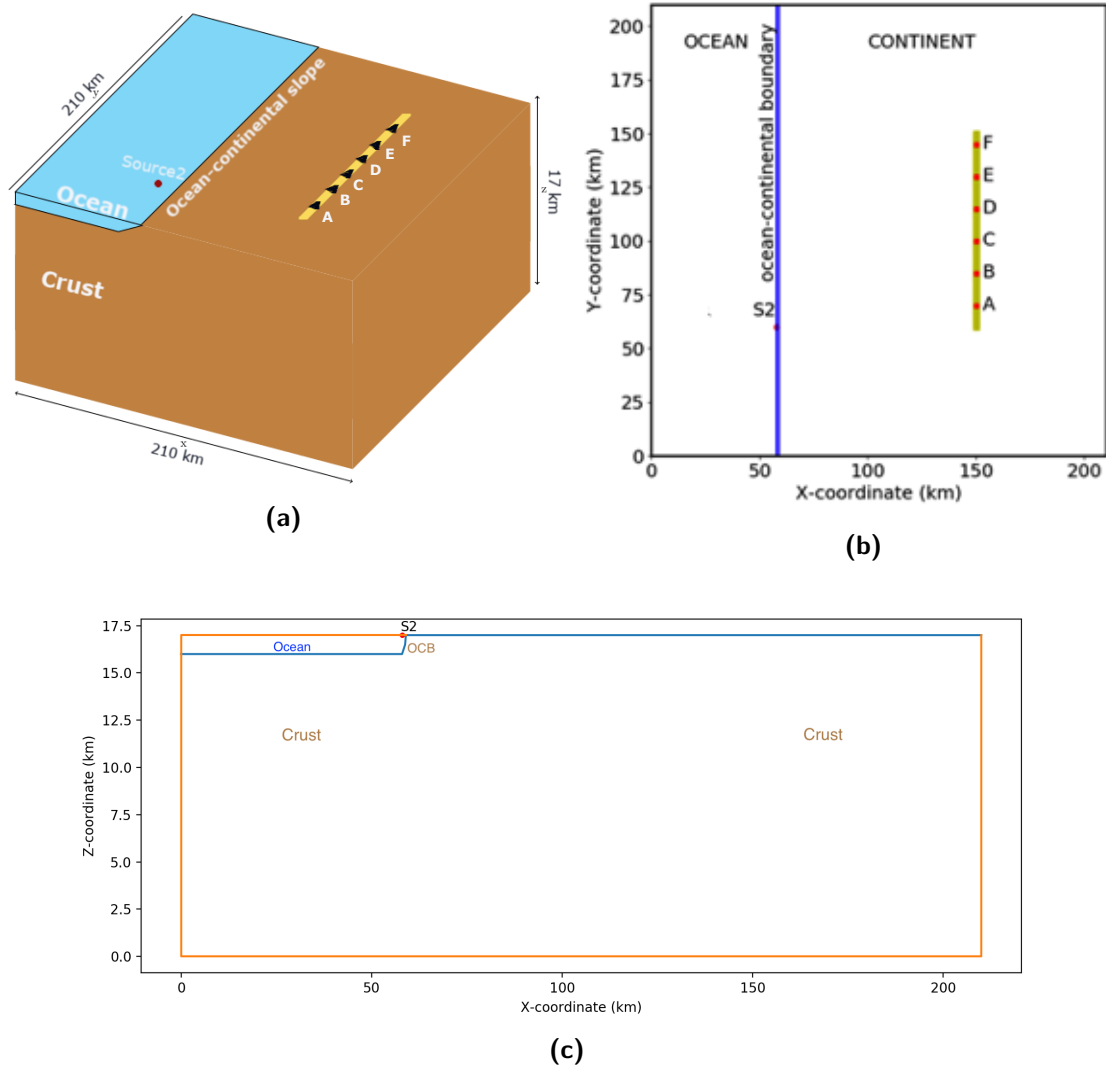


Figure 4.1 – Model I a) 3D representation of the model I with 1 km ocean and 16 km crust on the oceanic side and 17 km crust on the continent side. The volume of the mesh is 210 km × 210 km × 17 km. b) Top view of the source-receiver configuration. The source S2 (red dot) is an explosion whose spectrum is flat in the frequency band 0-1 Hz. S2 is located 1 m below the ocean surface close to the ocean-continent boundary. We deploy an array of 90 stations along the yellow line at a depth of 1 m below the crust. (Stations specified as A,B,C,D,E & F are used for waveform analysis. c) 2D profile of the mesh in XZ plane.)

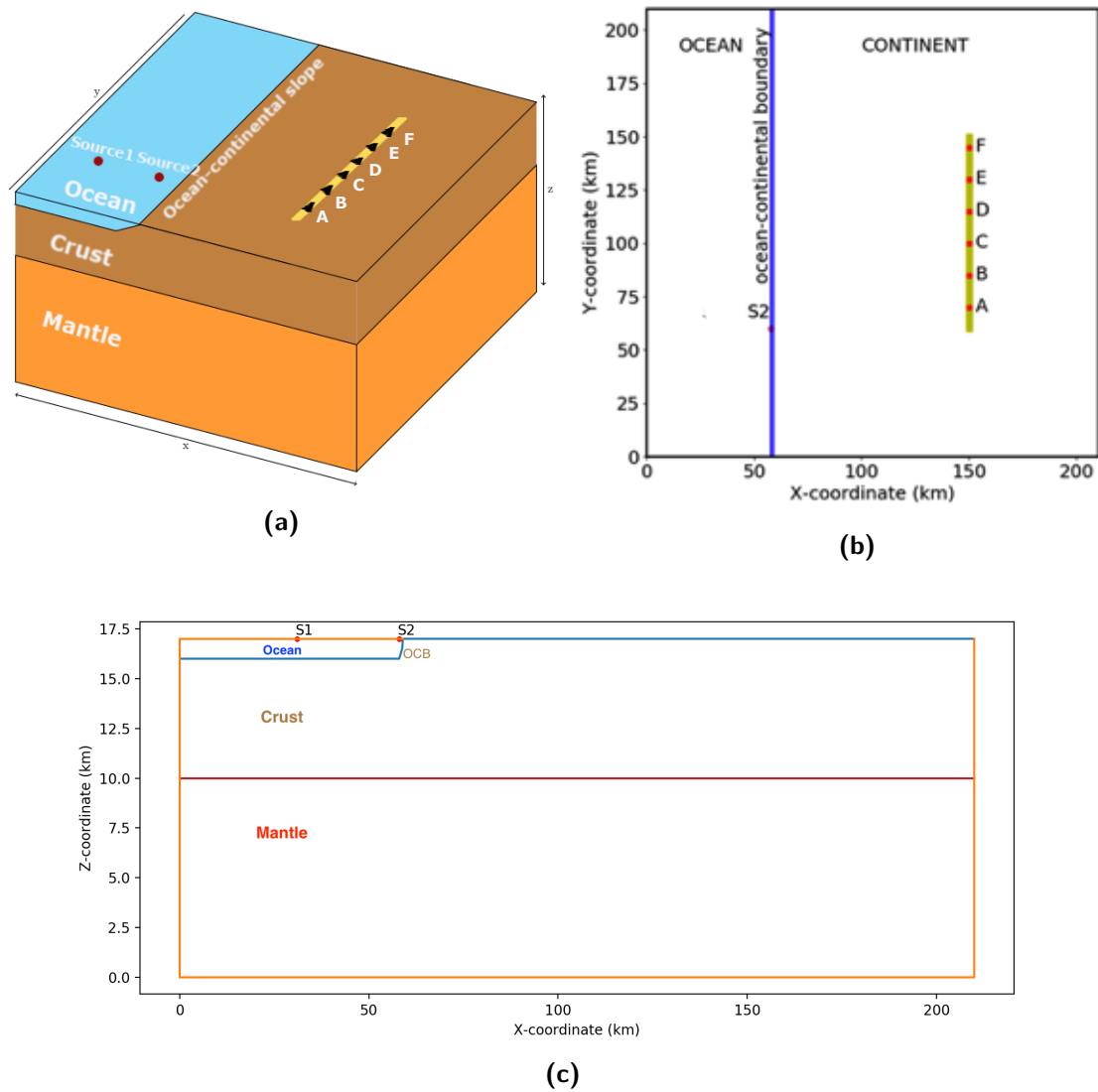


Figure 4.2 – Model II a) 3D representation of the model II with 1 km ocean, 6 km crust and 10 km mantle on the oceanic side, 7 km crust and 10 km mantle on the continent side. The volume of the mesh is 210 km x 210 km x 17 km. b) S2 (red dot) represents an explosion with flat response in the frequency band 0-1 Hz injected 1 m below the ocean surface close to the ocean-continent boundary. We deploy an array of 90 stations on the continent along the yellow line at a depth of 1 m below the crust. (Stations specified as A,B,C,D,E & F are used for waveform analysis. c) 2D profile of the mesh in XZ plane.

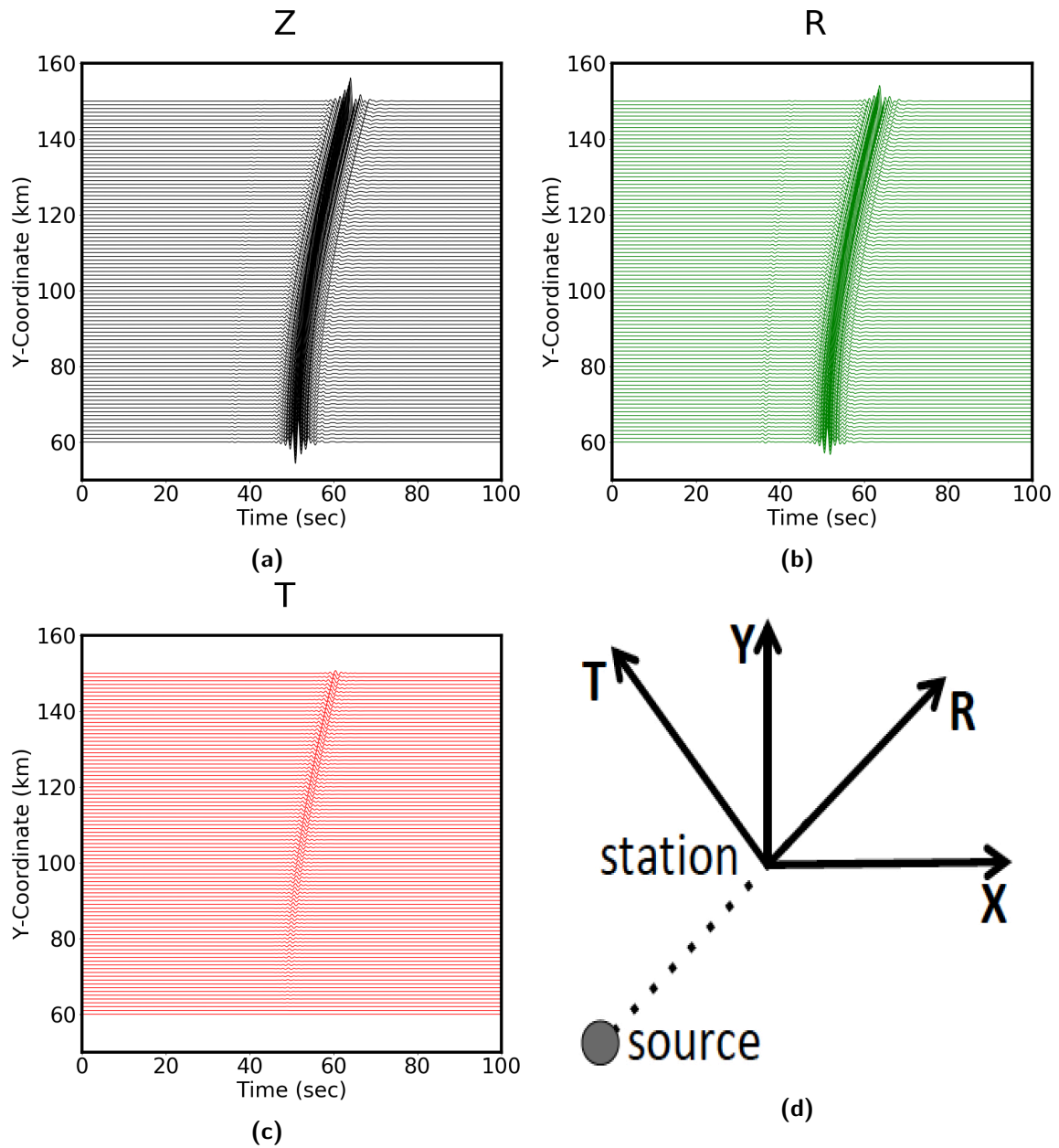


Figure 4.3 – Synthetic seismic velocity as a function of the stations y-coordinate for the a) vertical Z, b) radial R and c) transverse T components. Seismograms are computed for model I (1 km ocean and crust) and the source S2 located close to the ocean-continent boundary. d) sign-convention for rotation of X and Y displacement into radial R and transverse T.

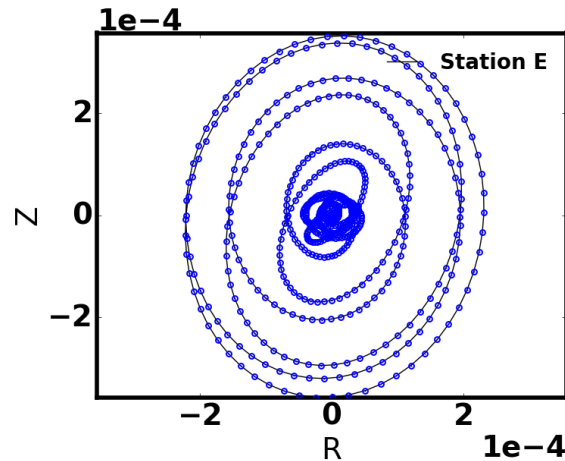


Figure 4.4 – Particle motion in the Z-R plane for station E in the frequency band 0.1-1 Hz in case of model I (1 km ocean and crust) and the source (S2) located close to the ocean-continent boundary. The elliptical polarization demonstrates the propagation of Rayleigh waves along the Z and R direction.

that can exist are P, S and fundamental Rayleigh wave when we restrict the frequency to 0.1-0.15 Hz as in Figure 4.6, and we observe that the polarization is linear at station A and becomes elliptical from station B to F with increasing ellipticity. The major axis of the ellipse is oriented parallel to the radial direction. The alignment of the particle motion along the R component demonstrate that the propagation is along the radial direction. The source is in the ocean and generate only P waves. The elliptical nature can only arise from the conversion of P to S wave at the sloping interface. Here the explanation is given in terms of body waves. As surface waves can be seen as the constructive interference of body waves, this explanation remain valid for the surface wave train. For each P wave arriving at the ocean-continent boundary, a converted S wave is generated and its polarization is in the plane of incidence of the P wave with respect to the sloping ocean-continent boundary. As the interface is not vertical, the converted S wave has a radial and transverse component. Therefore, the elliptical particle motion is due to a geometrical effect of the P to S conversion at the sloping interface. In the whole frequency range (figure 4.7), the polarization remains linear for all source-receiver azimuths with the major axis oriented parallel to the radial demonstrating that the propagation is along the radial component. The slightly more complex polarization in this frequency band results from the conversion of both the fundamental mode and the first overtone to fundamental mode surface wave at the interface. The first overtone is propagating at a different velocity than the fundamental mode and therefore, applying Snell's law at the interface, the converted mode propagate along azimuth that is slightly different from the radial azimuth and the resulting signal can be partly observed on the transverse component. Similarly, the Snell's law slightly modify the propagation azimuth of the fundamental mode through the interface.

In summary, for model I (1 km ocean and crust) the R-component seismic wave field recorded on the continent is P, S and fundamental mode Rayleigh waves. On the transverse component, we can record both S waves and Rayleigh wave fundamental mode that were generated by conversion at the sloping ocean-continent interface.

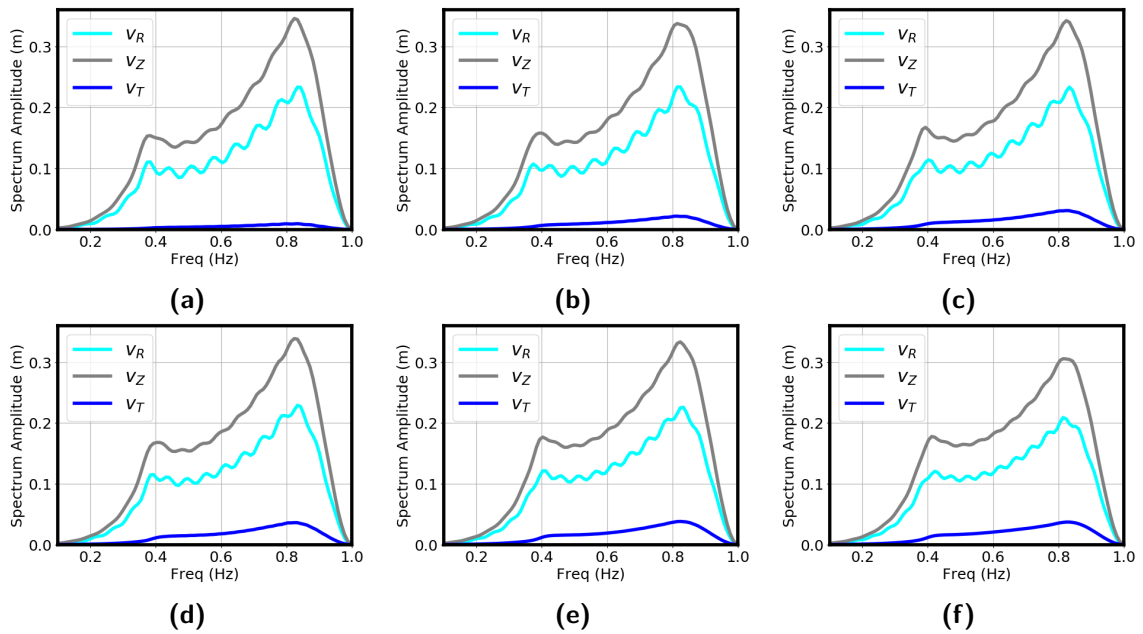


Figure 4.5 – Amplitude spectrum for stations A, B, C, D, E & F are shown in a), b), c), d), e), f) respectively for model I (1 km ocean and crust) and the source (S2) located close to the ocean-continent boundary. We observe weaker signal on the transverse component than on the vertical and radial components.

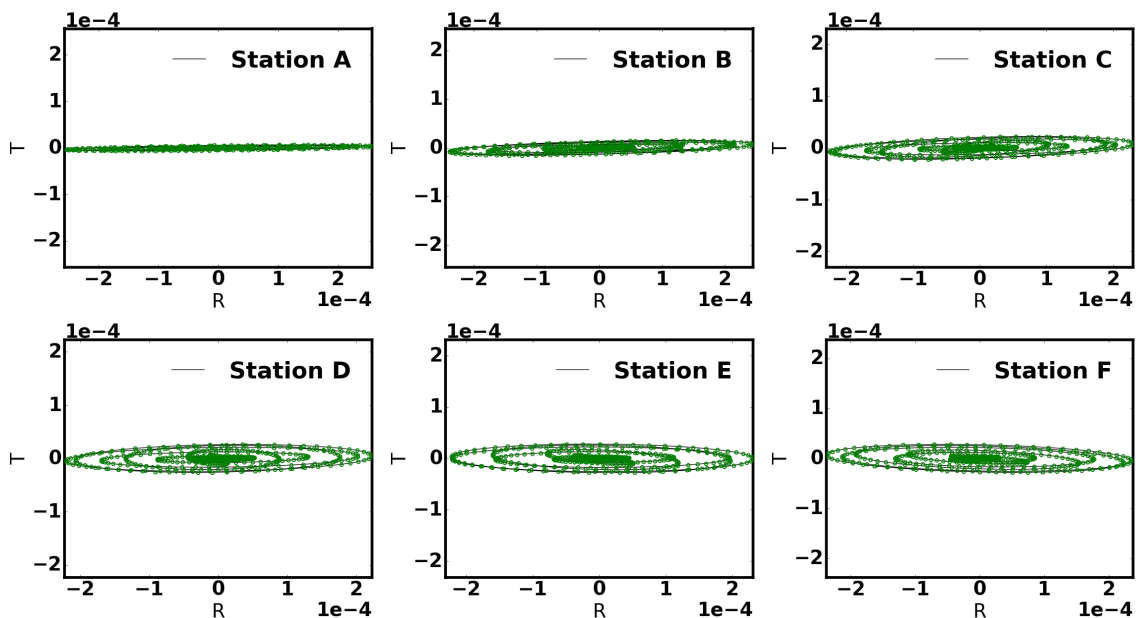


Figure 4.6 – Particle motion in the horizontal plane R-T for stations A, B, C, D, E, F for model I (1 km ocean and crust) and source S2 close to the ocean-continental boundary in the frequency band 0.1-0.15 Hz. The wave field is linearly polarized along the radial direction. The particle motion along R demonstrates that the propagation is along the radial direction.

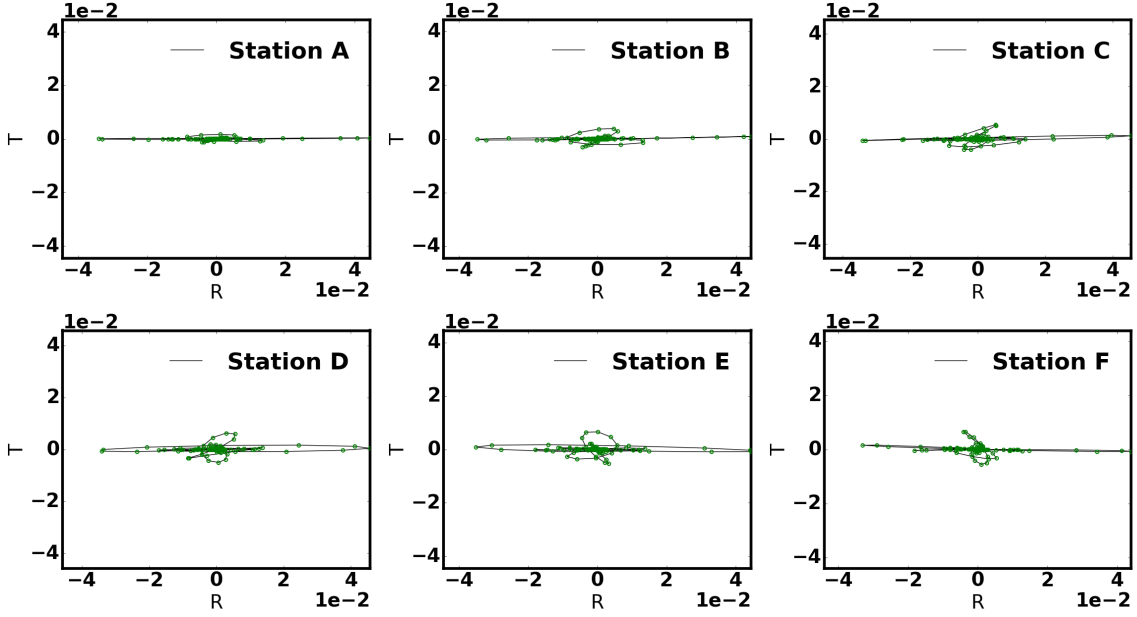


Figure 4.7 – Particle motion in the horizontal plane R-T for stations A, B, C, D, E, F for model I (1 km ocean and crust) and source close to the ocean-continental boundary in the frequency band 0.1-1 Hz. The wave field is linearly polarized with longitudinal axis aligned parallel to the radial direction. The complex particle motion in the center is attributed to the propagation of higher modes.

Rotational motion for model I and source at the ocean-continent boundary

In previous section, we observed that the seismic wave field traversing through the oceanic and the continental part of model I has small amplitude on the transverse component and that these waves cannot be Love waves. Now to interpret the wavefield, we compute the vertical rotational, as described in section 1.5.3, for all stations and compare it with the seismograms in velocity on the T component. For our study, we compute vertical rotational using an array of three stations (one along the x and other along y direction) centered around each of the above stations with an inter-station distance less than 1/4 of the minimum seismic wavelength (700 m in case of model I). The vertical rotational ω_Z is computed as

$$\omega_Z = \frac{\partial u_y}{\partial x} - \frac{\partial u_x}{\partial y} \quad (4.1)$$

where u_x and u_y is the horizontal seismic displacement along x and y axis respectively. $\frac{\partial u_y}{\partial x}$ is the difference between seismic displacement y-component for the two stations aligned along the x axis, and $\frac{\partial u_x}{\partial y}$ is similar for the x-components recorded by two stations along the y axis (Hadziioannou et al. 2012). The vertical rotational only records shear motion and its waveform similarity with the transverse velocity provides an evidence of propagation of SH waves. In that case we have $v_T = 2c\omega_Z$ where c is the local horizontal phase velocity. Figure 4.8 shows for model I the amplitude spectrum of Rayleigh (computed as $\sqrt{v_R^2 + v_Z^2}$, where v_R & v_Z are velocity in radial and vertical direction respectively) and for waves recorded on the transverse component on the left panel for each station. The waves that propagate on the T component have smaller amplitude than the Rayleigh waves. The next panel on the right shows the comparison of scaled vertical rotational, $2c\omega_Z$ and the transverse velocity (v_T). As no Love wave exist for this model, the local phase velocity

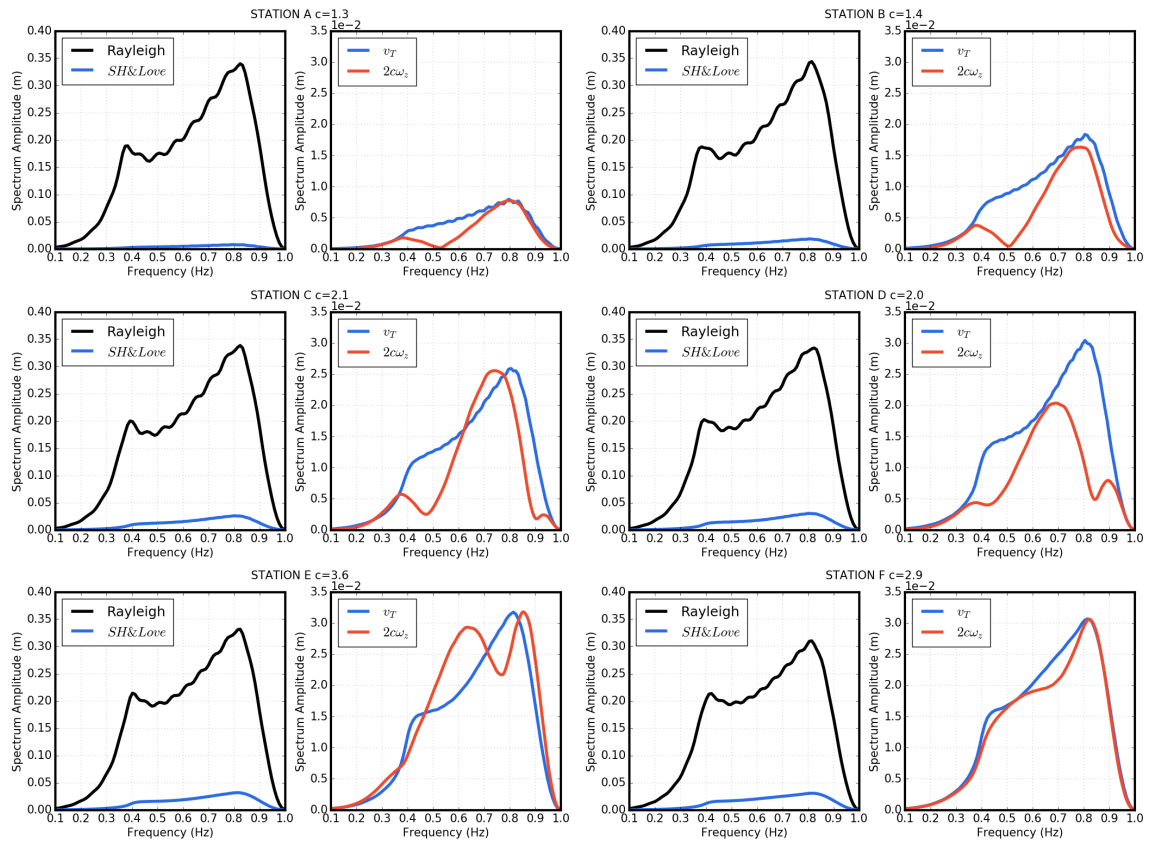


Figure 4.8 – Rayleigh vs SH/Love wave amplitude spectrum adjacent to vertical rotational rate $\times 2c$ (c : the local phase velocity computed as $v_{Tmax}/2\omega_{Zmax}$ fundamental Love wave velocity from 1-D synthetics) vs transverse velocity as a function of frequency for stations A, B, C, D, E & F in model I (1 km ocean, without mantle) and source close to the ocean-continental boundary. Rayleigh wave amplitude is higher than SH wave amplitude at all stations. The far stations have relatively higher SH wave amplitude than the close stations. The dissimilarity between the vertical rotational rate and transverse velocity indicates no Love wave propagation at all frequencies. Therefore, shear waves are recorded at all stations.

c is computed as $v_{Tmax}/2\omega_{Zmax}$. The computed c is written on top of each plot. The energy that is recorded on the transverse component in this model does not superimpose with the vertical rotational (the red and blue curves do no match) for $f > 0.2$ Hz. It does match for $f < 0.2$ Hz but the amplitude is very weak. For $f < 0.2$ Hz, the waves that propagate on the T component are mostly shear waves whose horizontal velocity (phase velocity) is related to $v_s/\sin\theta$ where θ is the incidence angle of the S wave at the station. As this angle is close to 90 deg, the S wave propagate almost horizontal and the phase velocity is close to v_s in the crust. Therefore on the T-component, at lower frequencies SH waves are recorded on the continent. At frequency above 0.2 Hz, the pattern is more complex because the signal recorded on the T component may result from both SH wave and the conversion of the first overtone and fundamental mode to the fundamental mode of Rayleigh wave.

In summary, we have shown that when the source is in the ocean close to the sloping ocean continent boundary, we can record signal on the transverse component for station on land. These signals are not Love waves because no Love wave exist in this model and for frequency below 0.2 Hz they are SH waves.

4.1.3 Seismic wavefield for model II (1 km ocean, crust and mantle)

Source at the the ocean-continental boundary

Similar to section 3.1.1, the seismic wave field simulated for model setup II using a source placed close to the ocean-continental boundary is analyzed by comparing the amplitude spectrum and polarization. Figures 4.9a, 4.9b, 4.9c represent the Z, R and T components of the seismic velocity recorded at all stations. Z and R components record Rayleigh waves as the dominant wave type in the frequency band of 0.1-1 Hz. We clearly observe that higher amplitude of seismic wavefield is generated on the T component as compared to the wave field in model I(4.10 versus Figure 4.5). The amplitude spectrum depicted in the figure 4.10 for stations A, B, C, D, E & F show increase in the amplitude on the T component with increasing source-receiver azimuth and longer distance. We observe two peaks at 0.4 and 0.8 Hz which remains same for all stations. The amplitude at high frequency is larger than at low frequency.

Figure 4.11 shows the particle motion in the R-T plane in the frequency band 0. to 0.15 Hz. This frequency band was selected because only the fundamental mode of surface wave is present. The polarization is linear along the radial axis for the closest station A. It becomes progressively elliptical and the major axis of the ellipse rotates with an increasing angle with respect to R component for stations further away. The P wave generated at the source can be reflected and/or transmitted at the ocean bottom and at the crust-mantle interface before reaching the ocean-continent interface with different incident angles. It is then transmitted as P and S waves on the continental side. The interference of all these transmitted S waves may explain the tilted horizontal elliptical polarization.

The polarization observed for the entire frequency band in figure 4.12 is even more complex, due to the presence of fundamental mode and higher modes in the oceanic part of the model and it is difficult to predict how different modes affect the particle motion.

The tilt in the polarization (unlike in model I) and the larger amplitude on the transverse component with respect to model I may be related to the presence of Love and/or large

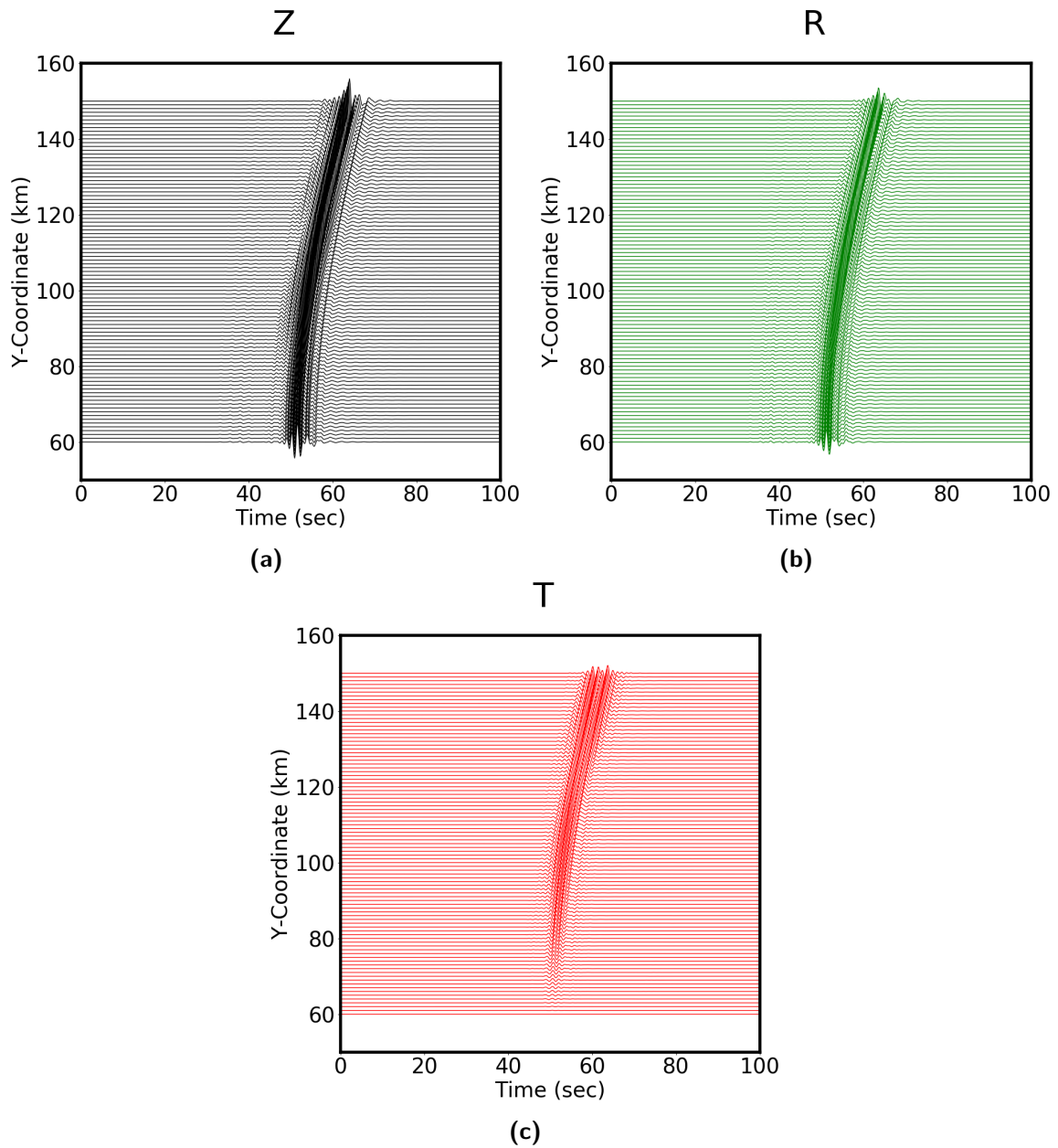


Figure 4.9 – Synthetic seismic velocity as a function of the stations y-coordinate for the a) vertical Z, b) radial R and c) transverse T components. Seismograms are computed for model II (1 km ocean, crust and mantle) and the source (S2) located close to the ocean-continent boundary.

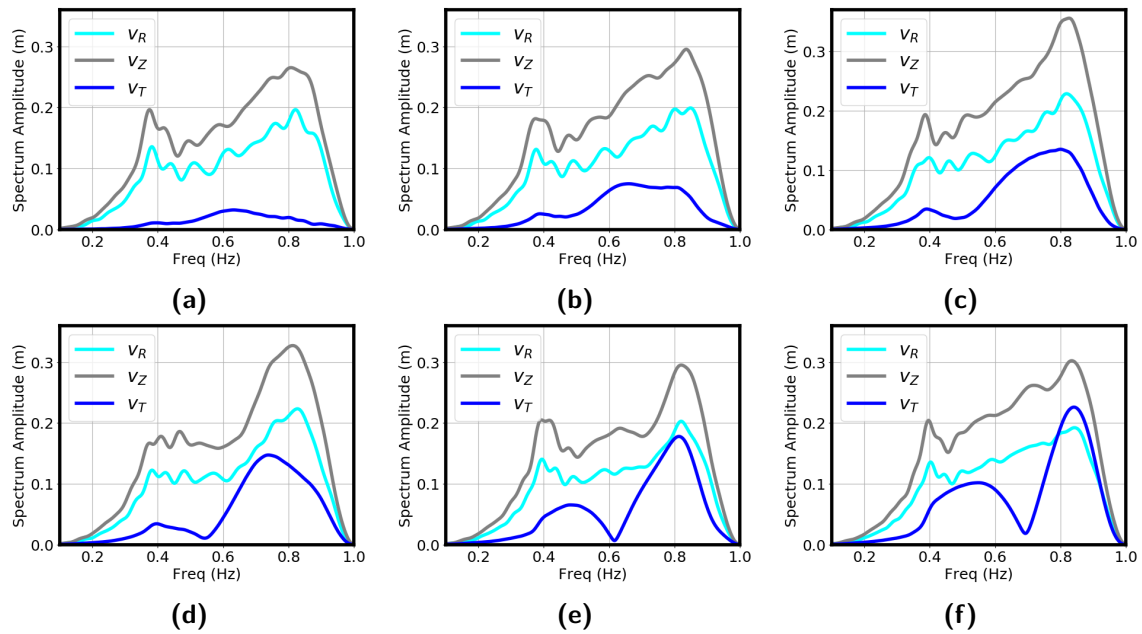


Figure 4.10 – Amplitude spectrum for stations A, B, C, D, E & F are shown in a), b), c), d), e), f) respectively for model II (1 km ocean, crust, mantle) and source S2 close to the ocean-continental boundary. The signal on the transverse component becomes stronger at larger source-receiver azimuth and is greater than the signal in model (I).

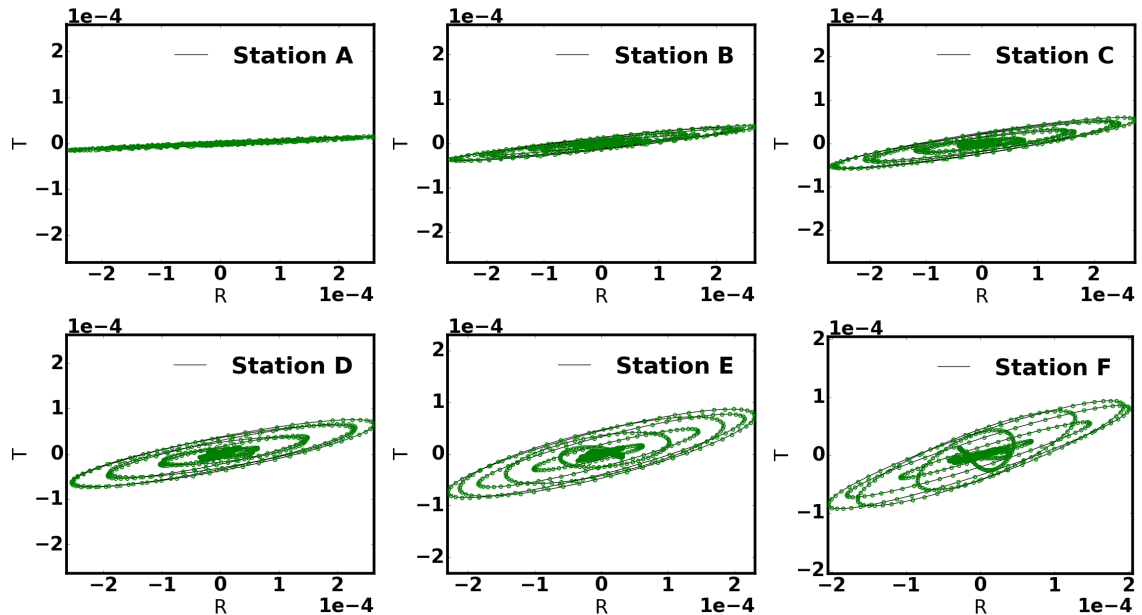


Figure 4.11 – Particle motion in the horizontal plane R-T for stations A, B, C, D, E, F for model II (1 km ocean, crust, mantle) and source close to the ocean-continental boundary in the frequency band 0.1-0.15 Hz. The wave field is elliptically polarized but the longitudinal axis rotates with respect to the radial axis.

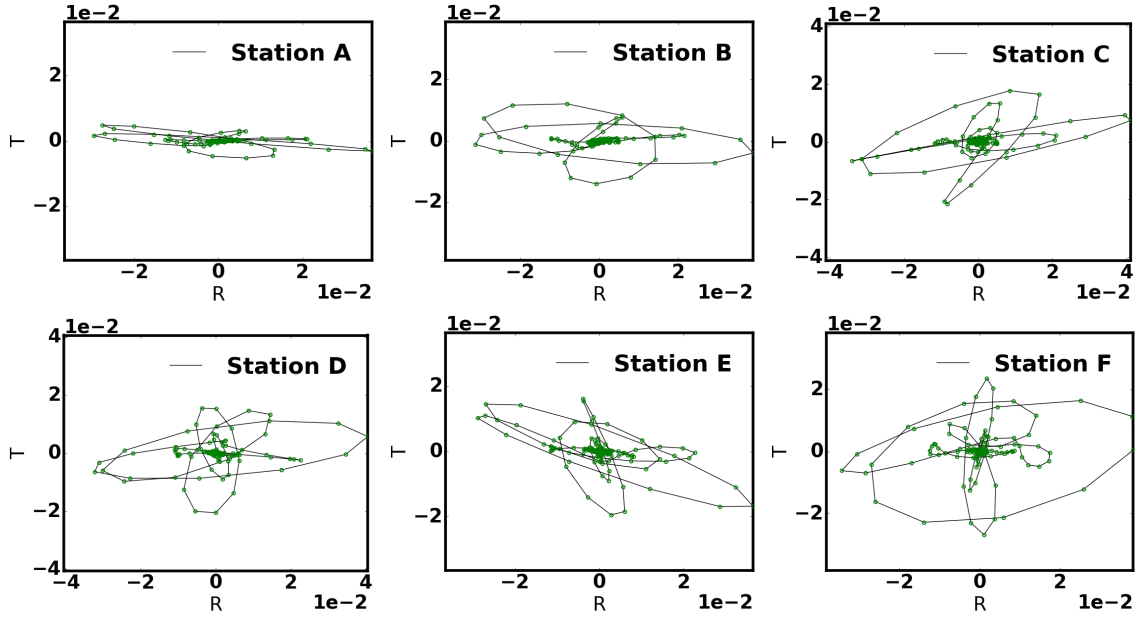


Figure 4.12 – Particle motion plots for stations A, B, C, D, E, F for model II (1 km ocean, crust, mantle) and source close to the ocean-continental boundary in the frequency band 0.1-1 Hz. The wave field is elliptically polarized but the longitudinal axis rotates with respect to the radial axis and becomes horizontal at station F

amplitude SH waves in the T component. In order to prove the existence of Love wave and/or SH wave we now analyze the rotational motion in section 4.1.3.

Rotational motion for source at the ocean-continent boundary

Similar to section 4.1.2, we compute the vertical rotational to compare with the transverse velocity. Figure 4.13 (left panel) shows the energy of the Rayleigh waves and on the transverse component for model II as a function of frequency. We see that the energy on the transverse component is larger for this model than for model I. The middle panel for each station shows the comparison between $2c\omega_Z$ and v_T . In that case c is the theoretical phase velocity of the fundamental mode of Love wave at the station location, that is in the continental 1D model (7 km crust and 10 km mantle). We observe a good agreement between both waveforms which demonstrate that the signal on the transverse component is dominantly Love waves. Finally we show the L/R amplitude ratio plotted as a function of frequency on the right panels of figure 3.13. The ratio increases with larger azimuth and distance with respect to the source. The highest ratio at stations A, B, C, D, E & F is 0.148, 0.3, 0.397, 0.47, 0.53, 0.64 observed at peak frequencies 0.63, 0.62, 0.71, 0.69, 0.78, 0.87 Hz. For $f < 0.5$ Hz, smaller L/R ratios are observed that at higher frequency. These results indicate more conversion of Rayleigh to Love waves energy at higher frequencies than at lower frequency.

Hence, in this section, we show that there is a good fit between $2c\omega_Z$ and v_T . Therefore, the signal on the transverse component is dominantly fundamental Love waves. We conclude that Love waves are generated in 1 km ocean model as a result of conversion of Rayleigh wave energy into Love wave energy at the ocean-continental boundary. The maximum L/R ratio obtained is 0.64.

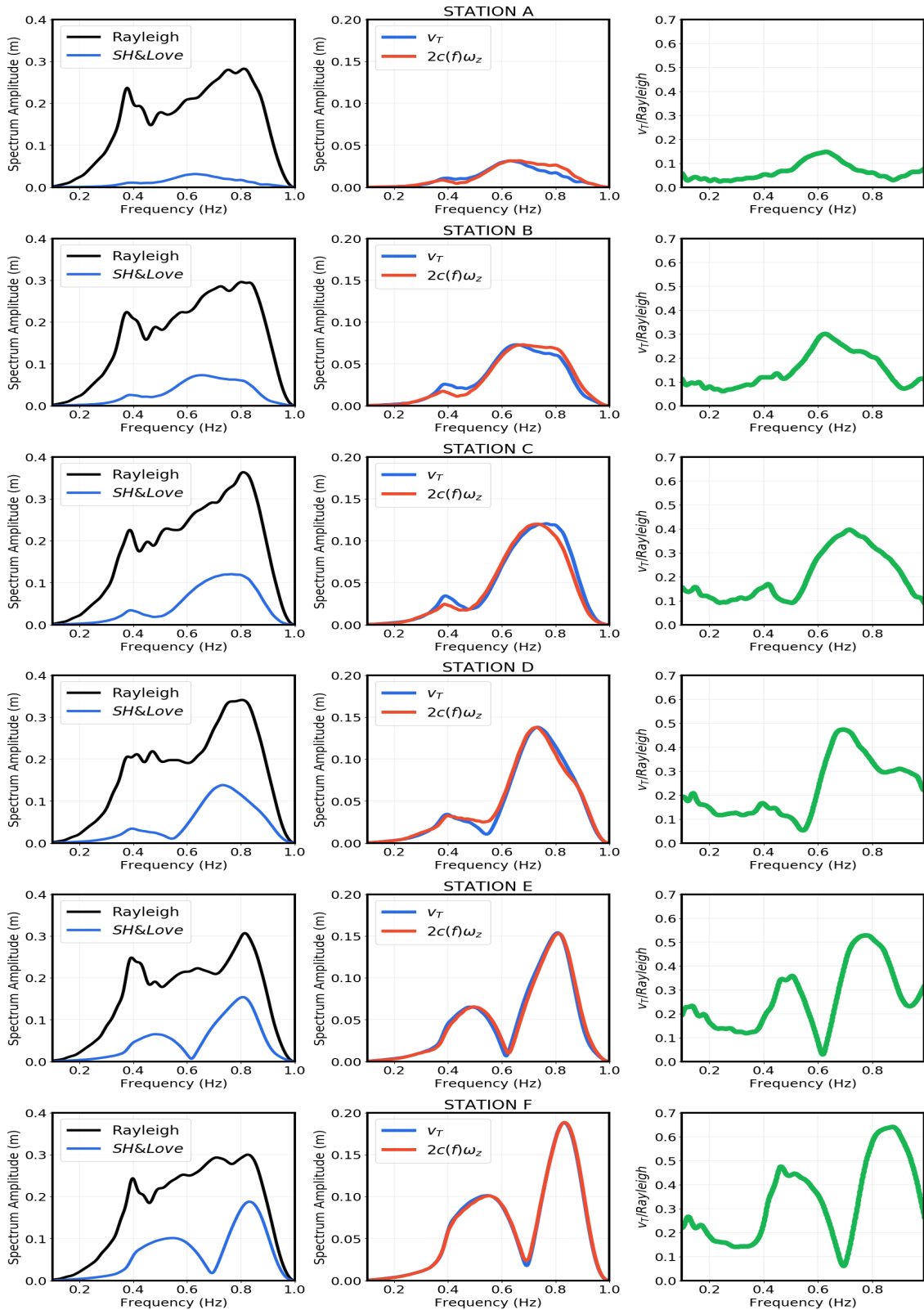


Figure 4.13 – Rayleigh vs SH/Love wave amplitude spectrum adjacent to vertical rotational rate * 2c (c: fundamental Love wave velocity from 1-D synthetics) vs transverse velocity as a function of frequency for stations A, B, C, D, E & F in model II (1 km ocean, with mantle) and source close to the ocean-continental boundary. Rayleigh wave amplitude is higher than SH wave amplitude at all stations. The far stations have relatively higher SH wave amplitude than the close stations. The similarity between the vertical rotational rate and transverse velocity indicates Love wave propagation at all frequencies.

Seismic wavefield for source far from the ocean-continental boundary

In the previous section, we showed that Love wave can be generated by a source close to the ocean-continent boundary. In order to determine whether, these Love waves are generated by source site effect or due to propagation effect, we now consider a source placed far away from the boundary (indicated as S1 in figure ??) in model II.

The source is an explosion, its magnitude is $10^{20} N$, placed at a distance of 23 km from the ocean-continental boundary, 1 m below the free ocean surface. The wave field recorded on the continent is shown in figure 4.14a, 4.14b, 4.14c representing the Z, R and T components of the seismic velocity at all stations plotted as a function of increasing y-coordinate of the station location. We observe two wave packets in the Z and R component. In figure 4.15 are shown, the amplitude spectrum of v_R, v_Z, v_T for stations A, B, C, D, E & F. We observe multiple peaks at different frequencies resulting from constructive and destructive interference of waves. v_R, v_Z amplitude decreases slightly with longer distances whereas the energy recorded on the transverse component increases with increasing source-receiver azimuth.

The horizontal particle motion in the plane R-T in the frequency band 0.1-0.15 Hz is shown in figure 4.16. We observe linear polarization with major axis aligned parallel with respect to R axis for all stations. In this frequency band, negligible Love or SH wave is generated and therefore the wave field propagates mostly as Rayleigh waves in the radial direction. For the frequency band 0-1 Hz, the particle motion is shown in figure 4.17, the polarization is elliptical for close stations whereas it becomes more complex at far stations. The complex nature of the ellipse is caused by the interference of higher modes. Considering that surface waves are generated by body wave interference, it can also be explained as follows: the P wave generated at the source is multiply reflected, transmitted and or converted in the different layers of the oceanic part of the model before reaching the ocean-continent boundary. Each multiple arrives at the boundary with a different angle and is transmitted as P and S waves. The interference of all these transmitted S waves can explain the horizontal complex polarization.

Therefore for a far source we record strong signal on the transverse component only at higher frequencies. We observe the amplitude on the transverse component is lower than that generated by the close source except at the frequency of the peaks which correspond to resonance in the water layer. We will now investigate that rotational component in the following section.

Rotational motion for source far from the ocean-continental boundary

Let us again look at the vertical rotational ω_Z computed at stations A, B, C, D, E & F, for the case of far-source and model II. On the left panel of figure 4.18, we see that the amplitude of Rayleigh waves decreases whereas the amplitude on the transverse component increases with the increasing source-receiver azimuth and distance. Higher frequencies have higher amplitude than the lower frequencies.

The middle panel shows the spectra of transverse velocity v_T and vertical rotational $2c\omega_Z$ where c is the theoretical Love wave phase velocity of the fundamental mode (refer to chapter 3, figure 3.4). We observe that the match between the two waveforms increases for stations D,E, F whereas it is less matching for stations closer to the source (A, B, C).

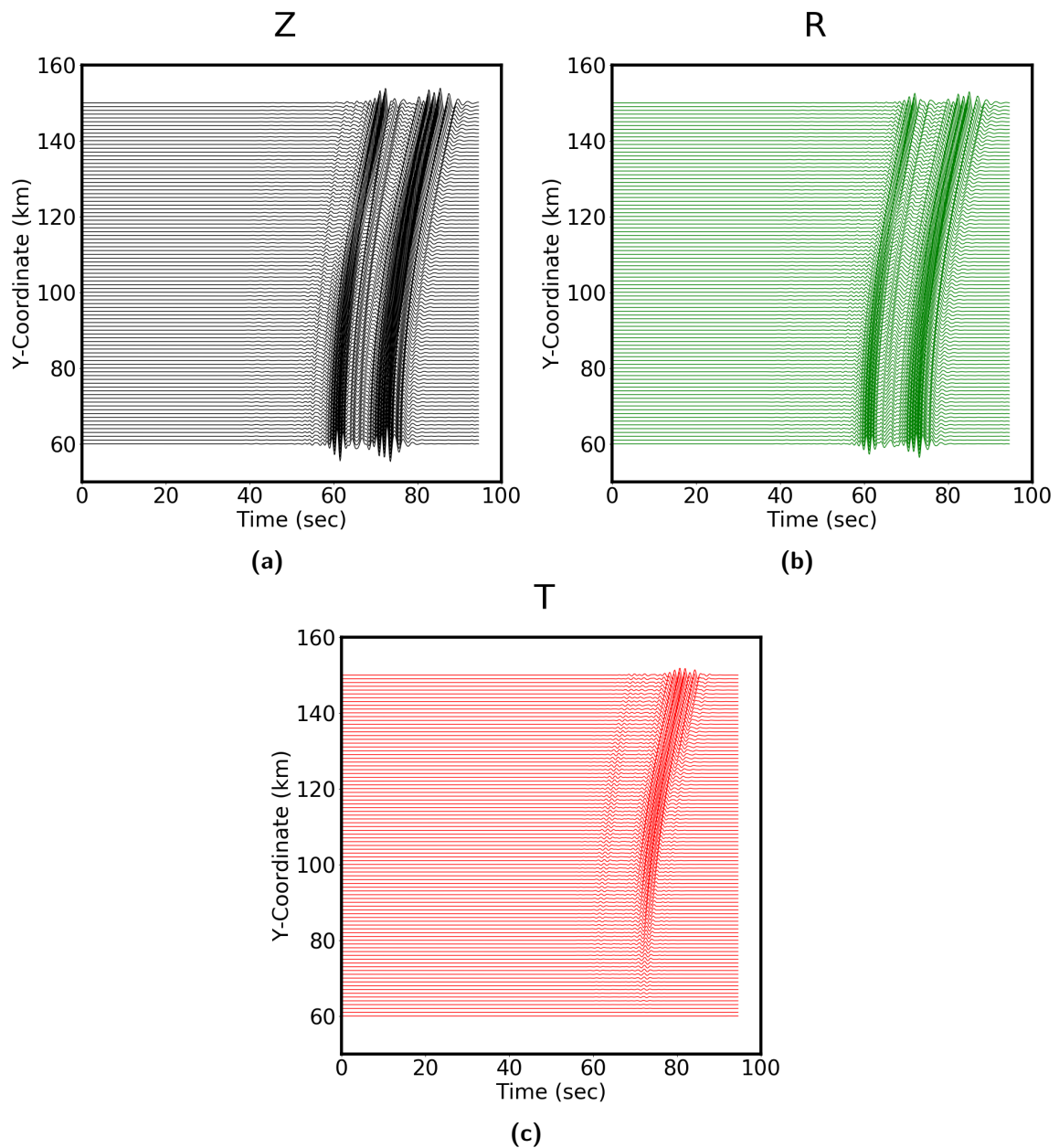


Figure 4.14 – Synthetic seismic velocity as a function of the stations y-coordinate for the a) vertical (Z), b) radial (R) and c) transverse (T) components. Seismograms are computed for model II (1 km ocean, crust, mantle) and the source (S1) located far from the ocean-continent boundary.

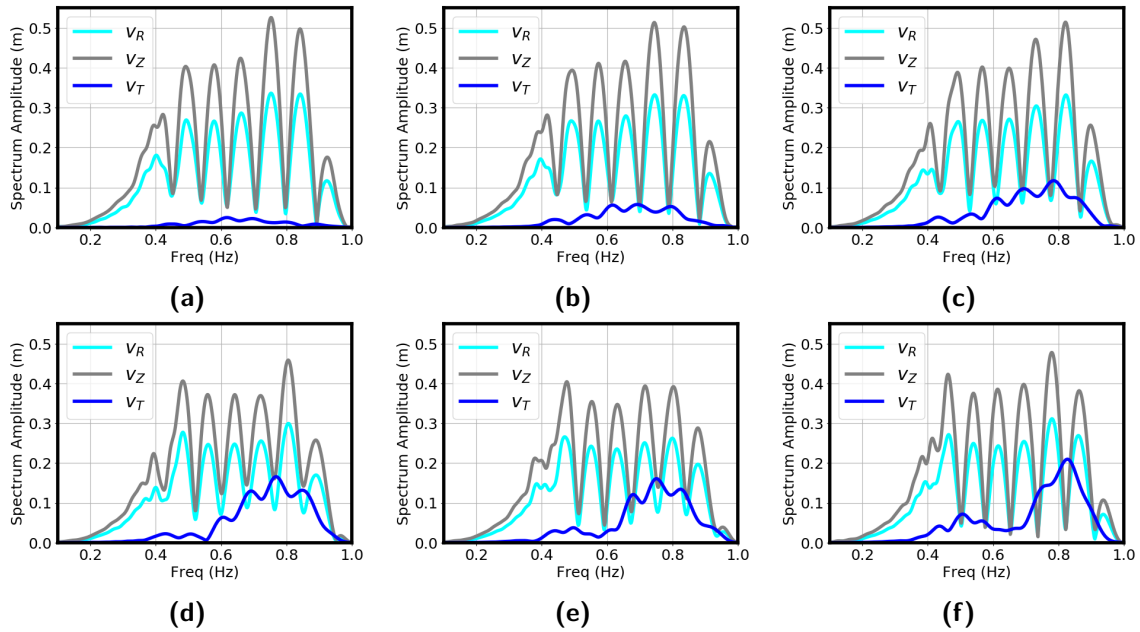


Figure 4.15 – Amplitude spectrum for stations A, B, C, D, E & F are shown in a), b), c), d), e), f) respectively for model II (1 km ocean, with mantle) and source far from the ocean-continental boundary . The signal on the transverse component becomes stronger at higher source-receiver azimuth.

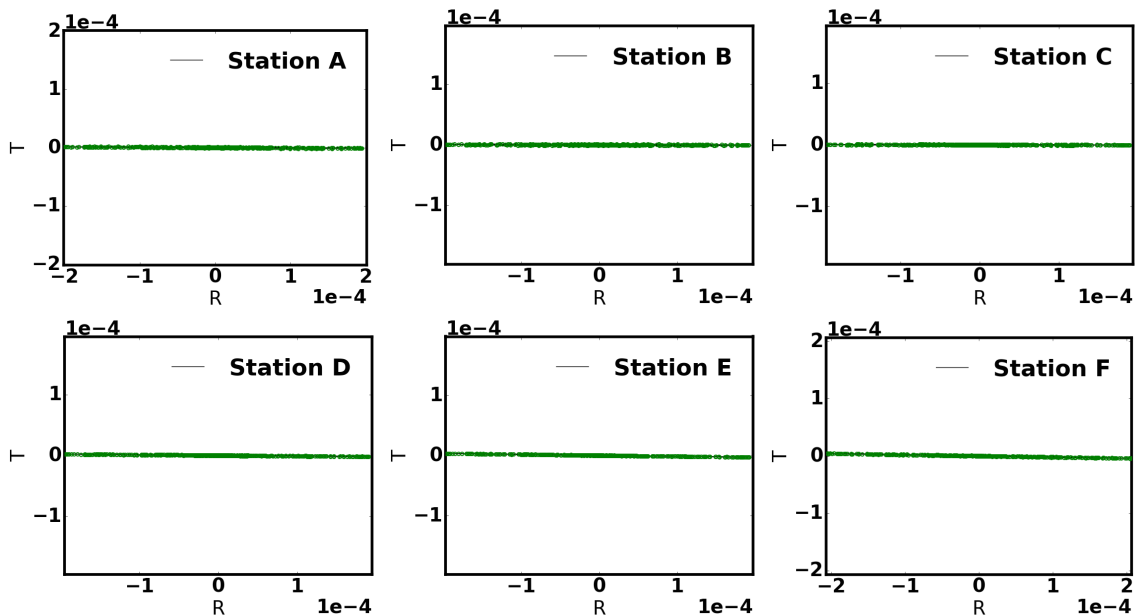


Figure 4.16 – Particle motion plots for stations A, B, C, D, E, F for model II (1 km ocean, with mantle) and source far from the ocean-continental boundary in the frequency band 0.1-0.15 Hz. The wave field is linearly polarized with the longitudinal axis aligned parallel to the radial axis.

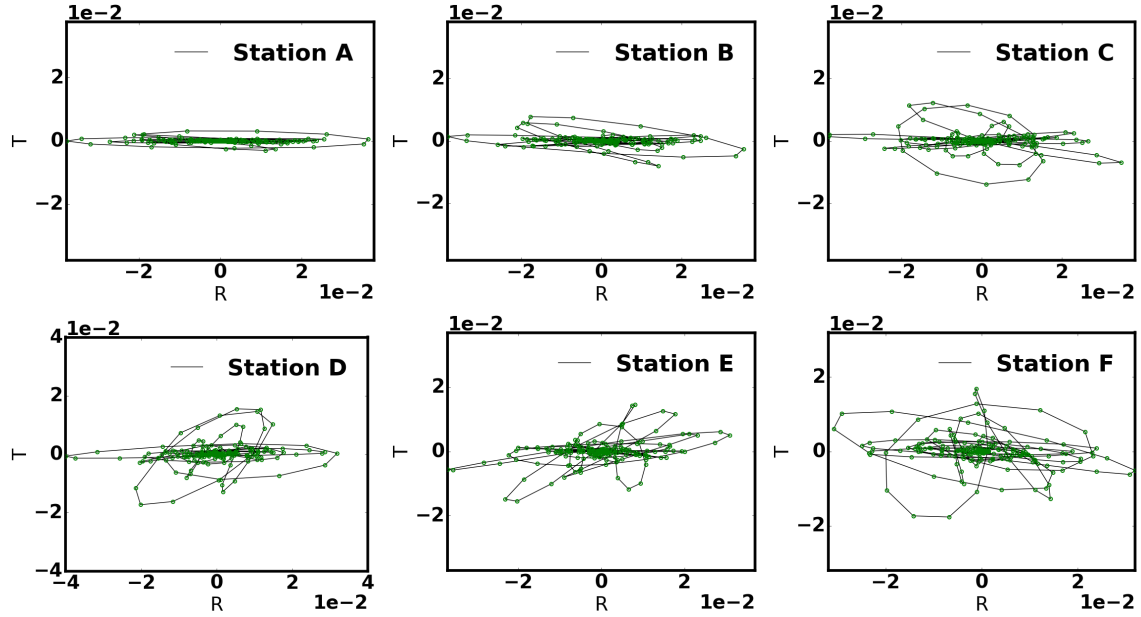


Figure 4.17 – Particle motion plots for stations A, B, C, D, E, F for model II (1 km ocean, with mantle) and source far from the ocean-continental boundary in the frequency band 0.1-1 Hz. The wave field is elliptically polarized with the longitudinal axis remaining parallel with respect to the radial axis.

The results imply that there is mere possibility of effective conversion of Rayleigh waves into Love waves at smaller source-receiver distances and azimuth whereas it increases at larger azimuth. The L/R ratio plotted in the right panel of figure 4.18 shows that the ratio increases from station A to station F. For stations A, B, C, D, E & F , the maximum L/R ratio achieved is 0.35, 0.81, 1.1, 0.9, 1.0 & 4.2 at peak frequencies 0.62, 0.7, 0.78, 0.75, 0.75, 0.82 Hz respectively.

The fit between between v_T and $2c\omega_Z$ is not perfect but it is increasing for increasing distance. In conclusion, this good fit demonstrate that Love wave can be generated even when the source is far from the boundary. The amplitude of the Love waves is smaller than when the source is close to the sloping boundary.

4.1.4 Seismic wavefield for model III (3 km ocean, crust and mantle)

In section 4.1.3, we have demonstrated that in the case of thin ocean (1 km) the L/R amplitude ratio can vary between 0.15-0.64 when source is close to the ocean-continental boundary and between 0.35- 4.2 for a far source. Now to investigate the effect of ocean thickness on the ratio, we model thicker oceans (3 km and 6 km). Firstly, we analyze the seismic wave field in a 3 km ocean model (described in section 4.1.1) combined with the source site effect. Figure 4.19 and 4.20 (left panel) show for the far and close source respectively, the resulting wave field in the form of amplitude spectrum of total Rayleigh ($\sqrt{v_R^2 + v_Z^2}$) waves and energy on T component in velocity. We observe for both close and far source that the energy recorded on the transverse component increases with the increasing source-receiver distance as seen in the frequency domain 0.1-1 Hz whereas Rayleigh waves energy decreases.

The middle panels show the comparison of vertical rotational and transverse velocity. We use the Love wave fundamental mode phase velocity at the station for the scaling of ω_Z .

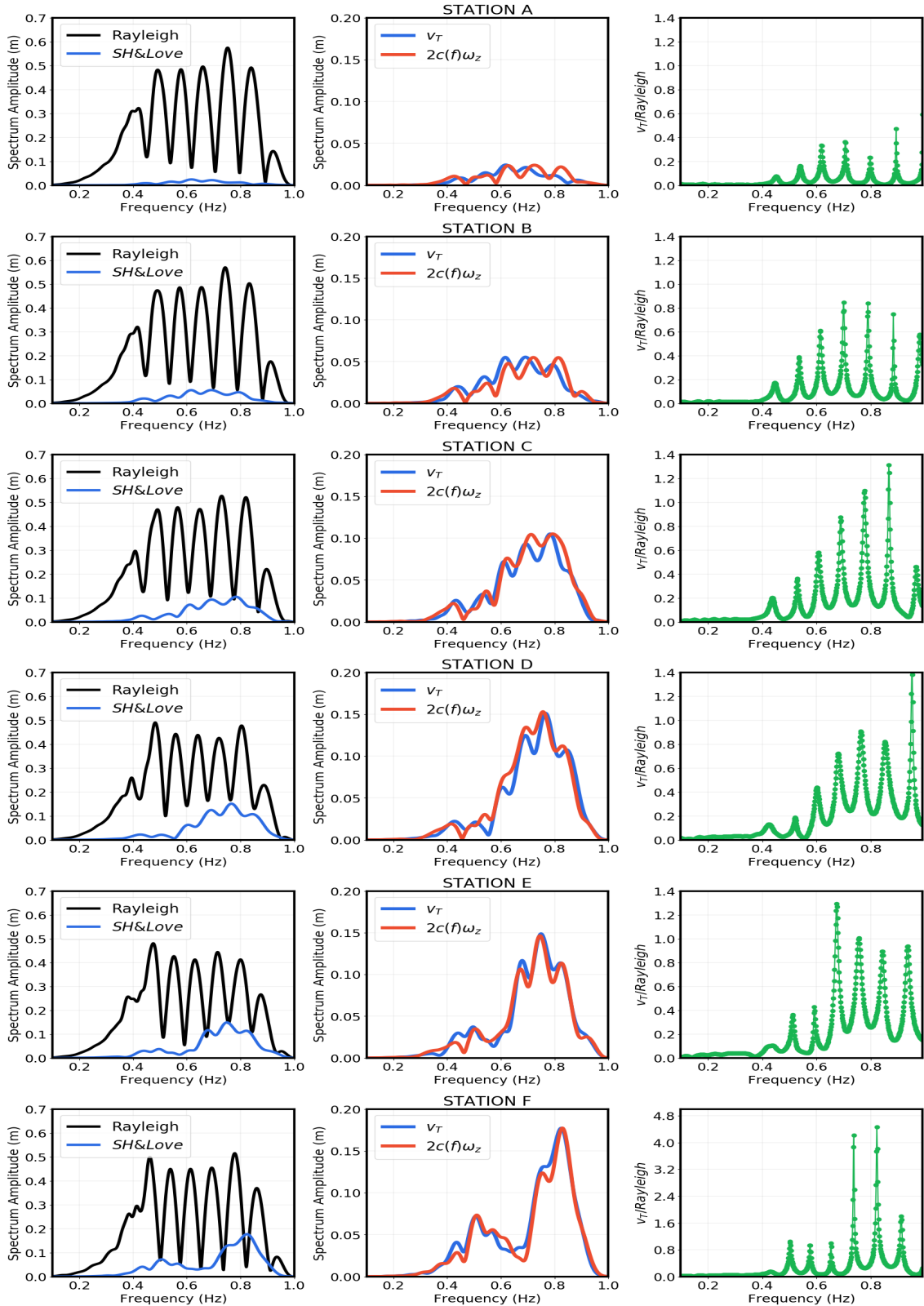


Figure 4.18 – Rayleigh vs SH/Love wave amplitude spectrum adjacent to vertical rotational rate $\times 2c$ (c : fundamental Love wave velocity from 1-D synthetics) vs transverse velocity as a function of frequency for stations A, B, C, D, E & F in model II (1 km ocean, with mantle) and source far from the ocean-continental boundary. Rayleigh wave amplitude is higher than SH wave amplitude at all stations. The far stations have relatively higher SH wave amplitude than the close stations. The similarity between the vertical rotational rate and transverse velocity indicates Love wave propagation at most frequencies.

For S2 source, we observe good fit between $2c\omega_Z$ & v_T with small amplitude difference at certain frequencies for stations A and B, and maximum amplitude fit for other stations. This good fit confirms that the signal on the transverse component is mostly Love wave fundamental mode. Similarly for source S1, the overlapping spectra of $2c\omega_Z$ and v_T at all frequencies confirm that the signal on the transverse component is mostly Love waves.

The L/R ratio plotted in the right column of 4.19 demonstrates that for synthetics corresponding to source S2, this ratio less than 1 for all source-receiver azimuths in the model. The stations at shorter propagation paths (station A, B, C) record L/R as low as 0.19 at peak frequency 0.8 Hz. For station D & E, the highest ratio recorded is 0.72 and 0.82 respectively however at peak frequencies 0.8 Hz, the ratio is 0.3. The maximum ratio is observed at station F with value 0.92 at peak frequency 0.66 Hz.

Similarly the L/R ratio is shown for synthetics generated by the far source S1 in the right column of 4.20. The peak frequencies record ratio of 0.1, 0.2, 0.23, 0.423, 0.25, 0.46 at stations A, B, C, D, E, F respectively. At 0.3 Hz, the ratio at these stations is 0.025, 0.075, 0.12, 0.145, 0.2, & 0.24. The maximum ratio is obtained for station F i.e, 1.875 at 0.25 Hz.

In summary, the effect of increased ocean thickness on the L/R amplitude ratio recorded on the continent can be stated as follows: for source close to the ocean-continental boundary, the ratio increases. It is higher than in model II (1 km ocean) for most frequencies with the highest ratio record of 0.9.

For far source, the ratio is higher than in model II at lower frequencies and vice-versa for higher frequencies, when the source is far from the boundary.

4.1.5 Seismic wavefield for model IV (6 km ocean, crust and mantle)

We then consider a deeper ocean of 6 km. We use the model configuration described in section 4.1.1. The spectra computed using a source close (S2) and far (S1) from the boundary are presented in figure 4.21 and 4.22. The left panel shows that as the ocean thickness increases, the Rayleigh wave and T component wave field energy decreases for source S2. It is lower than that in model II and III. Similarly for source S1, the Rayleigh wave amplitude decreases with increasing ocean thickness. However, the energy on the T components is higher than in model II and III for frequencies below 0.7 Hz. At frequencies greater than 0.7 Hz, it decreases.

The two waveforms $2c\omega_Z$ and v_T are shown in the middle column for both the sources. The good fit between the two curves is observed at all stations, however the maximum fit is observed at larger source-receiver distances for source S2. This similarity indicates that the signal on the T component is mostly Love waves. As compared to figure 4.21, the two waveforms are slightly less coherent for source S1. However at stations D, E, & F we observe significant fit between the two waveforms confirming the existence of Love waves on the transverse component.

Figure 4.21 (right panel) for source S2 show that the maximum L/R amplitude ratio recorded at station A, B, C, D, E & F is 0.25, 0.39, 0.35, 0.25, 0.35, & 1.07 at frequencies 0.55, 0.56, 0.56, 0.75, 0.63, & 0.7 Hz respectively. Figure 4.22 (right panel) for source S1 show that the L/R ratio recorded at these stations have values 0.1, 0.22, 1.3, 0.7, 0.57, 0.84 at peak frequencies 0.75, 0.75, 0.82, 0.82, 0.65, 0.58 Hz respectively. However the

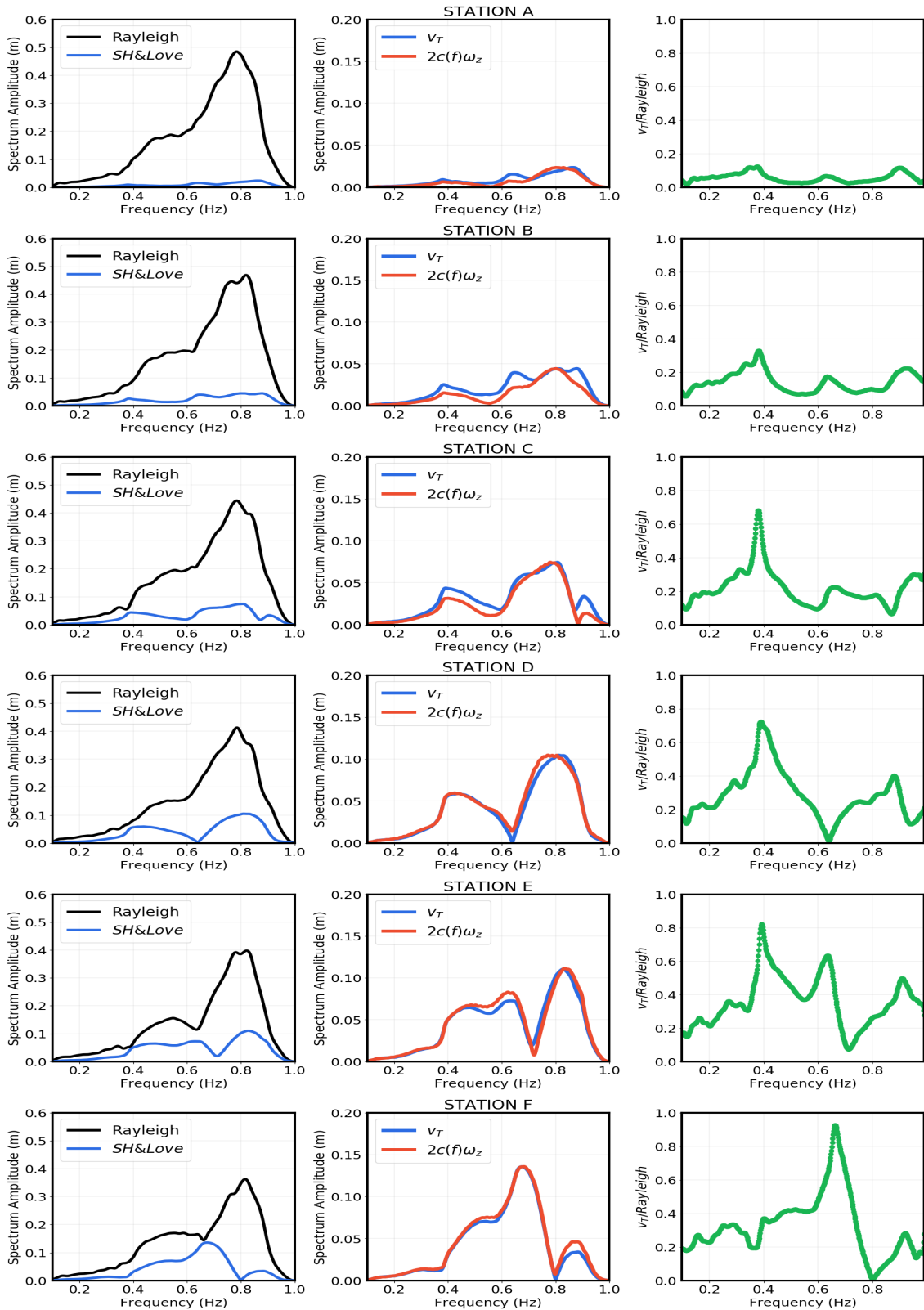


Figure 4.19 – Rayleigh vs SH/Love wave amplitude spectrum adjacent to vertical rotational rate $\times 2c$ (c : fundamental Love wave velocity from 1-D synthetics) vs transverse seismic velocity as a function of frequency for stations A, B, C, D, E& F in model III (3 km ocean, with mantle) for a source close to the ocean-continental boundary. Rayleigh wave amplitude is higher than SH wave amplitude at all stations. The far stations have relatively higher SH wave amplitude than the close stations. The similarity between $2c\omega_z$ and v_T indicates Love wave generation at all frequencies.

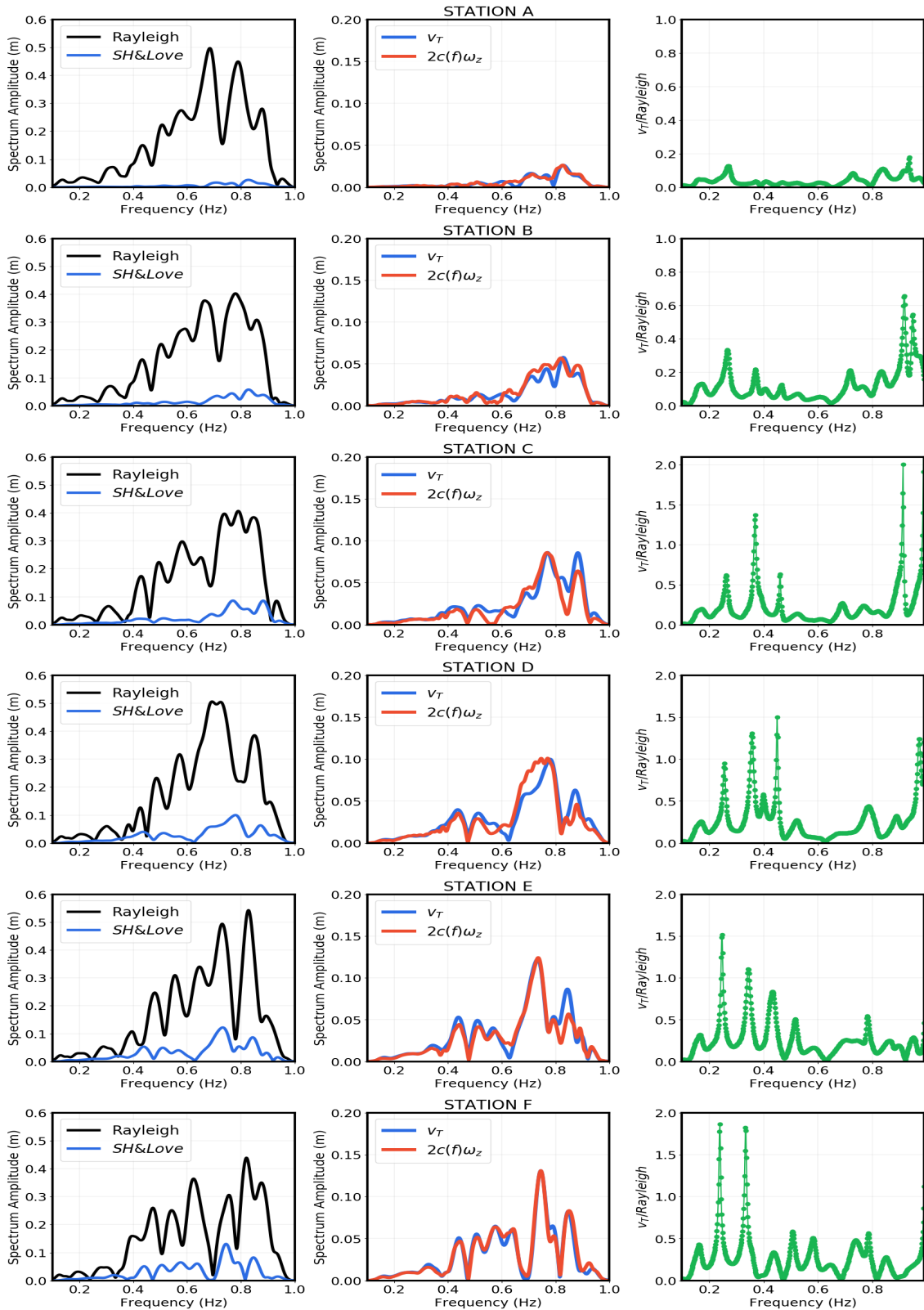


Figure 4.20 – Rayleigh vs SH/Love wave amplitude spectrum adjacent to vertical rotational rate $\times 2c$ (c : fundamental Love wave velocity from 1-D synthetics) vs transverse seismic velocity as a function of frequency for stations A,B,C,D,E& F in model III (3 km ocean, with mantle) for a source far-away from the ocean-continent boundary. Rayleigh wave amplitude is higher than SH wave amplitude at all stations. The far stations have relatively higher SH wave amplitude than the close stations. The two waveforms $2c\omega_z$ and v_T are less similar for close stations(Ab B,C) whereas good fit is observed for stations D, E, F . Therefore, Love wave propagates at all frequencies. The L/R amplitude ratio at all frequencies are also plotted.

maximum ratio is 2.5 at 0.35 Hz and 5.5 at 0.4 Hz for stations E & F respectively. The effect of 6 km thick ocean on the amplitude ratio for both sources can be summarized as: when source close to the boundary is modeled, the L/R ratio increases at lower frequencies. It is greater than in model II and III. For $f > 0.35$ Hz, it is smaller than model III but comparable with model II. The maximum L/R ratio of 1.07 is obtained. In case of far source, the amplitude ratio is greater than in model II and III for most frequencies.

4.2 Effect of sediments

In one study conducted in Australia, Gal (2017) observed strong L_Q waves energy generated from the direction that coincided with increased thickness in sea floor sediments. They proposed that L_Q waves were excited by S waves on interaction with sedimentary basins boundary leading to amplified L_Q wavefield. Thus, we study here the effect of sediments on the wave field generated from the secondary microseism noise sources. In order to do that, we modify our model IV and include the sediments on the sea floor, as shown in figure 4.23. Therefore, the model now has 6 km ocean, 3 km sediments, 6 km crust and 7 km mantle on the oceanic side and 15 km crust and 7 km mantle on the continent side. As previously, we study the effect of sediments due to far-source and close-source from the ocean-continental boundary on the T component seismic wave field.

4.2.1 Seismic wavefield for model V (6 km ocean, sediments, crust, mantle)

The Z, R & T components of the wave field for a source close to the ocean-continental boundary are plotted in figure 4.24 and for far source in figure 4.26. The spectra for source S2 (figure 4.25) and source S1 (figure 4.27) show that the amplitude of Rayleigh waves and signal on the T component both increases with longer propagation paths and become of close amplitude at stations E & F. It is higher than in model IV at all frequencies for source S2 whereas in case of source S1, it is lower for $f < 0.7$ Hz and higher at $f > 0.7$ Hz. Between the two sources, higher amplitude is recorded for source S2 than in source S1 at most frequencies.

On comparing the waveforms $2c\omega_Z$ and v_T for source S2, we observe a good fit from station C onwards. Stations E & F show maximum fit. In case of far source, we observe good fit between the two waveforms at all stations. Therefore, the signal on the T component generate by both sources is mostly Love waves.

For source S2, the ratio computed at these stations in the right column has value 0.18, 0.35, 0.33, 0.67, 1.36, 0.72 at peak frequencies 0.68, 0.69, 0.7, 0.74, 0.8, 0.83 Hz respectively. However, the maximum L/R amplitude ratio is 3.5 at 0.75 Hz for station F. For source S1, the L/R ratio ranges between 0.17 and 1.63 at peak frequencies for all stations. The maximum L/R ratio is obtained at station F i.e., 4.1 at 0.57 Hz

In conclusion, the L/R amplitude ratio in model V (with sediments) is lower than the ratio in model IV (without sediments) at lower frequencies ($f < 0.35$ Hz) and vice-versa at higher frequencies. The low velocity sedimentary layer present can entrap the P wave energy emitted from the source and act as a wave guide causing multiple reflections of the P waves before being transmitted as S waves in the continent. The localization of large

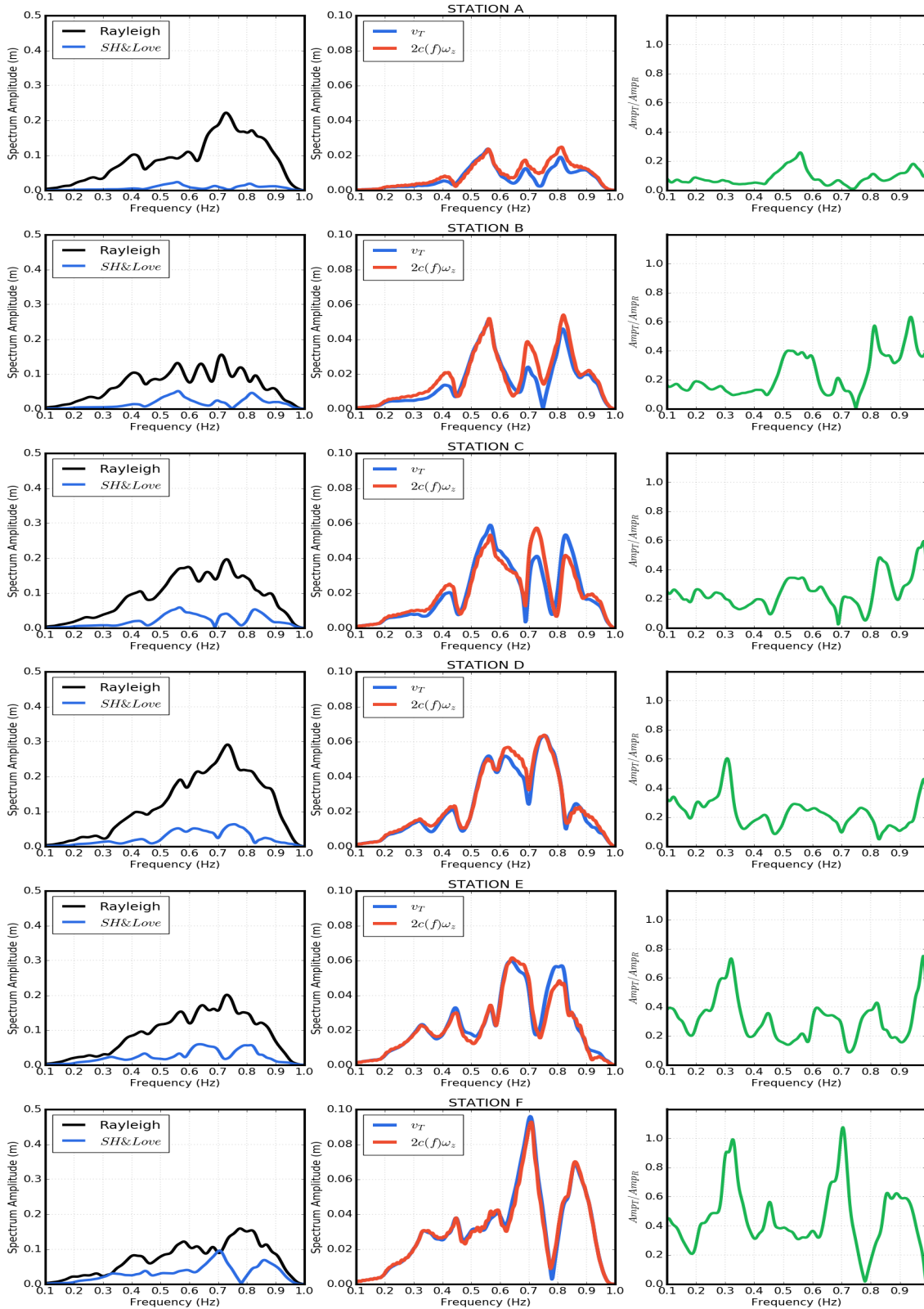


Figure 4.21 – Rayleigh vs SH/Love wave amplitude spectrum adjacent to vertical rotational rate $\times 2c$ (c : fundamental Love wave velocity from 1-D synthetics) vs transverse velocity as a function of frequency for stations A, B, C, D, E & F in model IV (6 km ocean, with mantle) when the source is placed close to the boundary. Rayleigh wave amplitude is higher than SH wave amplitude at all stations. The far stations have relatively higher SH wave amplitude than the close stations. The similarity between $2c\omega_z$ and v_T at most frequencies indicate Love wave generation. The L/R amplitude ratio at all frequencies are also plotted.

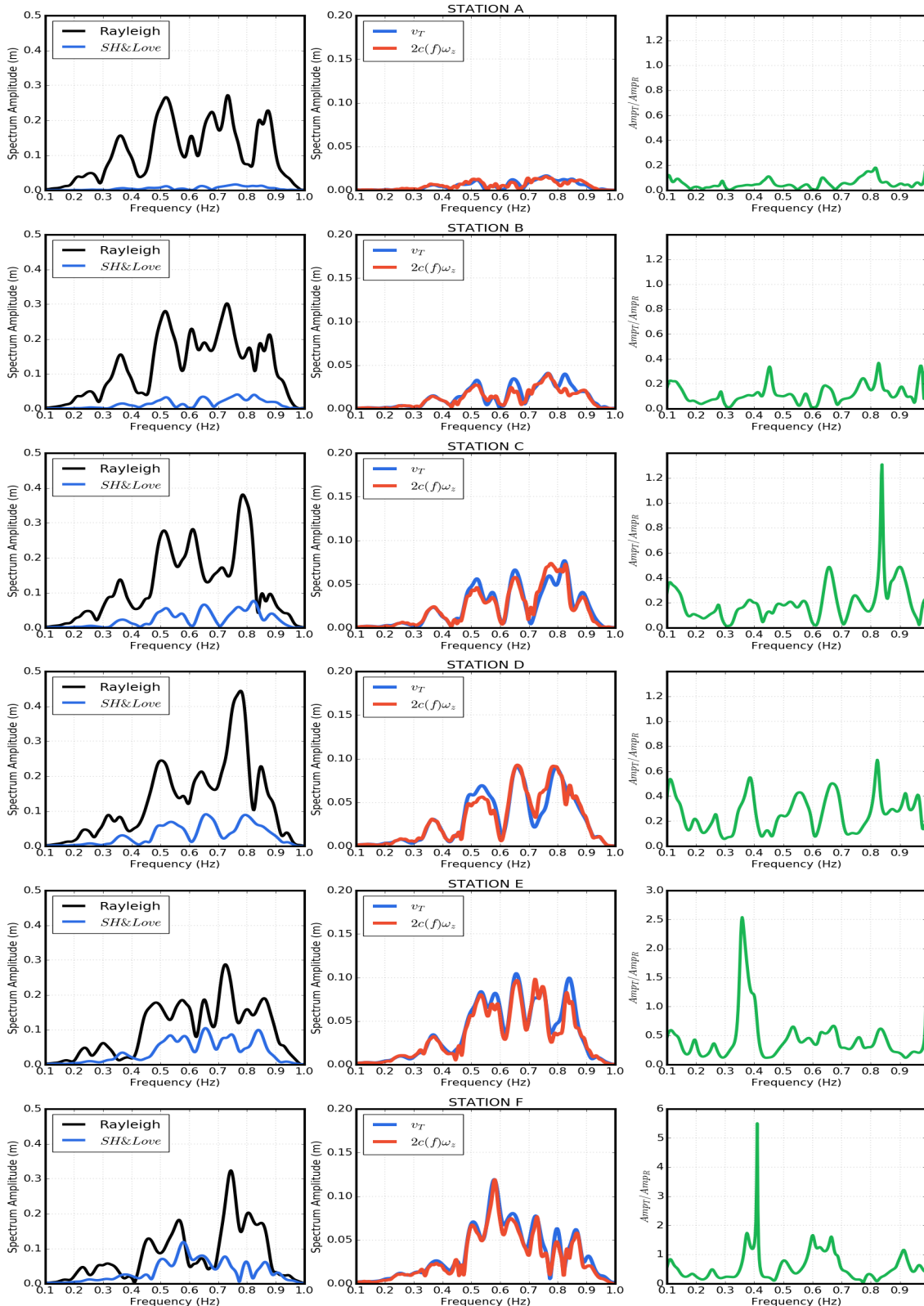


Figure 4.22 – Rayleigh vs SH/Love wave amplitude spectrum adjacent to vertical rotational rate $\times 2c$ (c : fundamental Love wave velocity from 1-D synthetics) vs transverse velocity as a function of frequency for stations A, B, C, D, E & F in model IV (6 km ocean, with mantle) when the source is placed far-away from the boundary. Rayleigh wave amplitude is higher than SH wave amplitude at all stations. The far stations have relatively higher SH wave amplitude than the close stations. The similarity between $2c\omega_z$ and v_T at most frequencies indicate Love wave generation. The L/R amplitude ratio at all frequencies are also plotted.

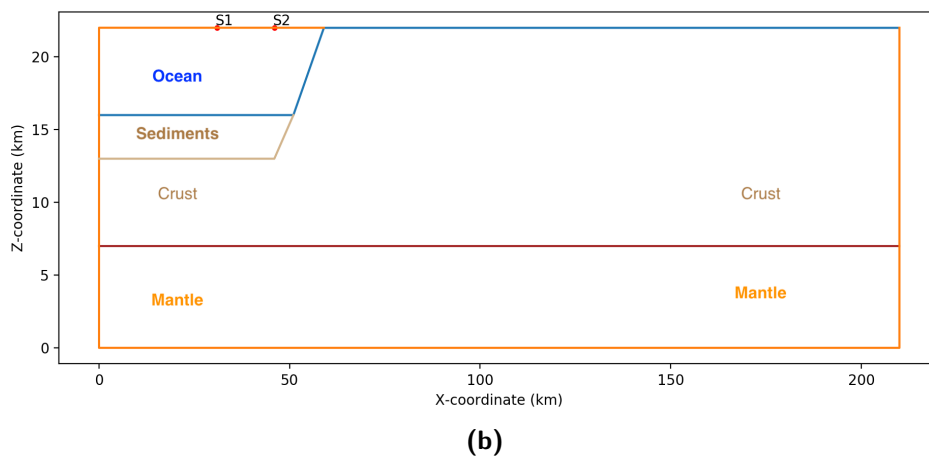
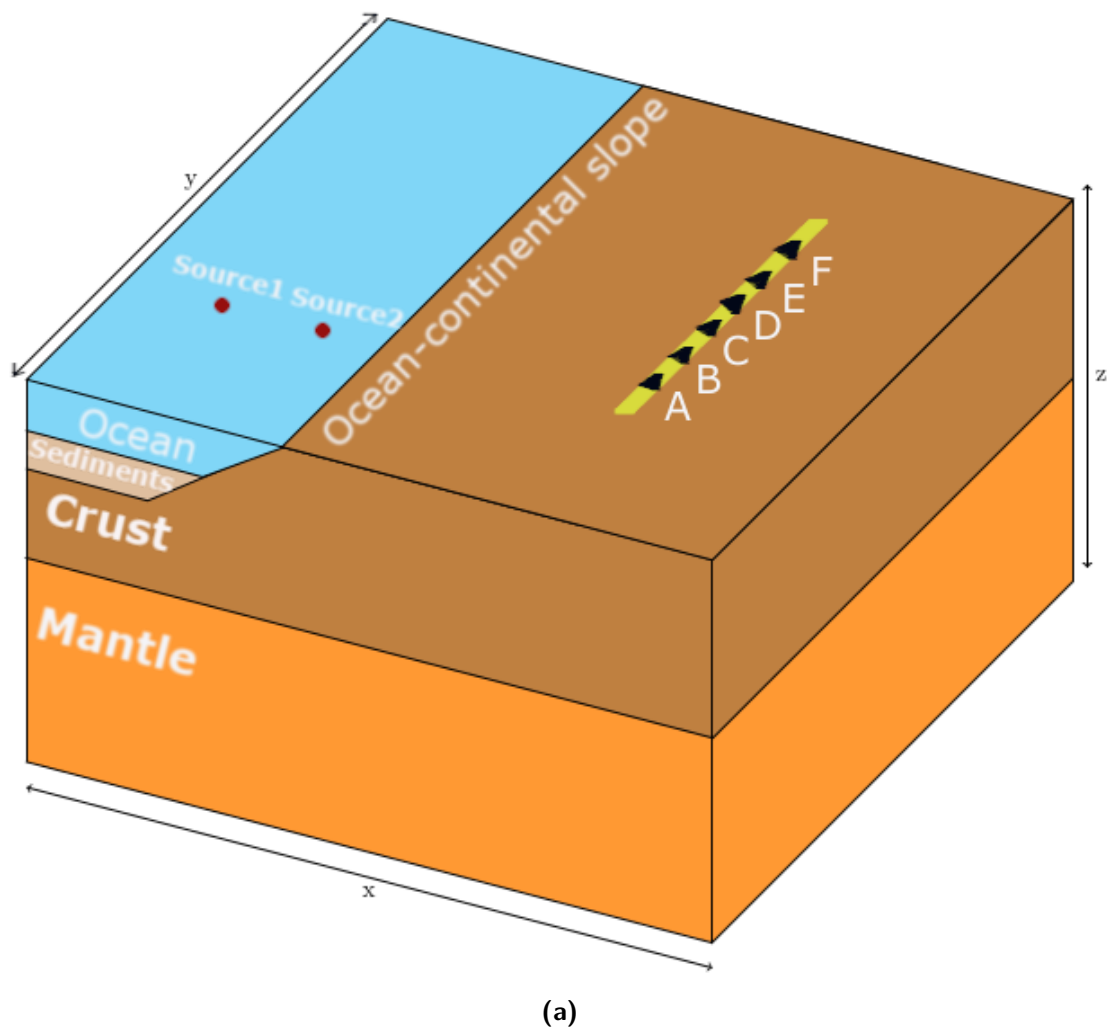


Figure 4.23 – 3D representation of the model with 6 km ocean, 3 km sediments, 6 km crust and 7 km mantle on the oceanic side, 15 km crust and 7 km mantle on the continent side. Source1 and Source2 (red dot) represents an explosion of frequency 0-1 Hz injected 1 m below the ocean surface. Source1 is placed at a distance of 20 km from the ocean-continent boundary whereas Source2 is above it. We deploy an array of 90 stations on the continent along the yellow line at a depth of 1 m below the crust. (Stations specified as A,B,C,D,E & F are used for waveform analysis). c) 2D profile of the mesh in XZ plane.

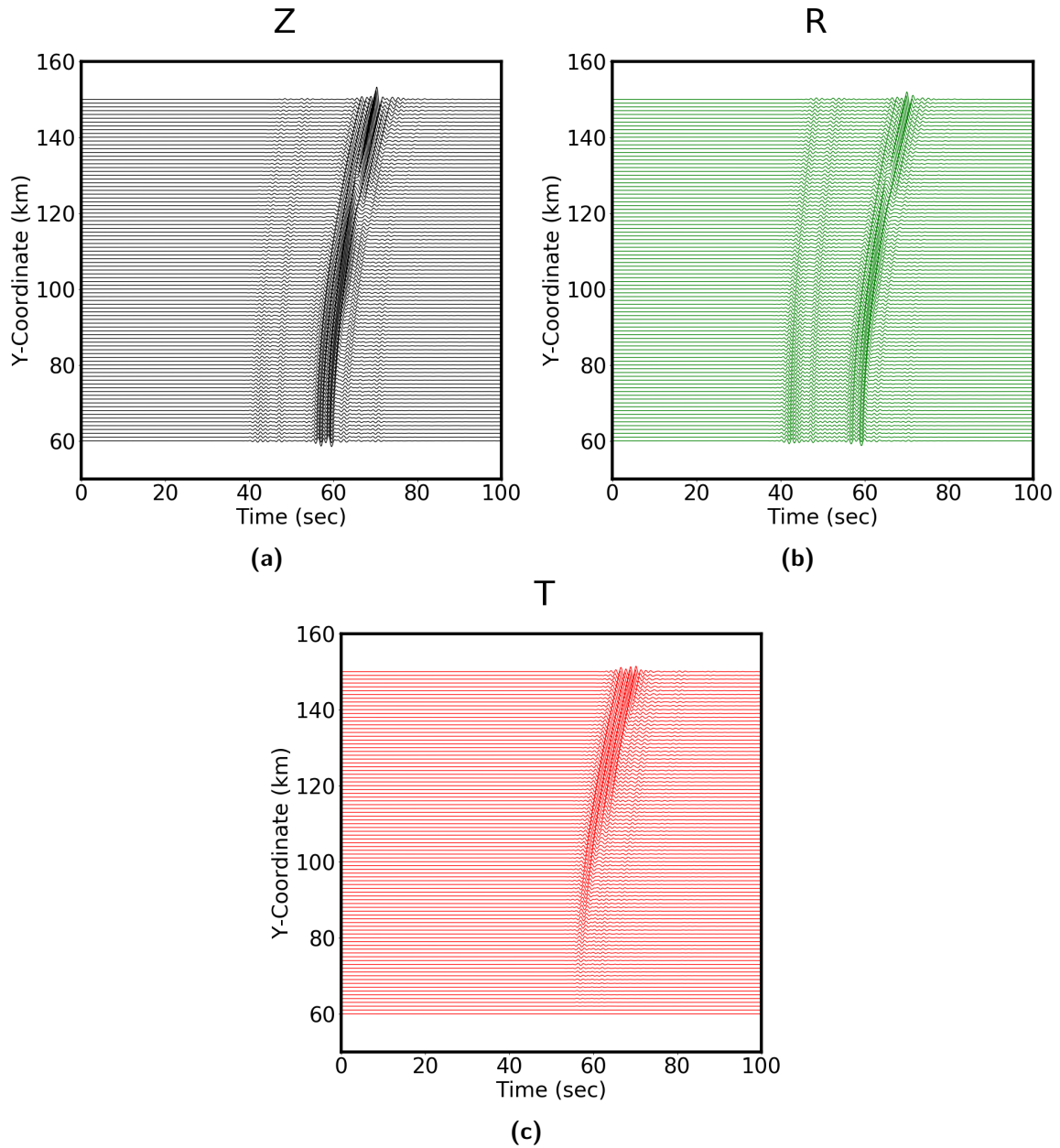


Figure 4.24 – Synthetic seismic velocity as a function of the stations y-coordinate for the a) vertical (Z), b) radial (R) and c) transverse (T) components. Seismograms are computed for model V (6 km ocean, 3 km sediments with mantle) and Source2 located close to the ocean-continent boundary is injected. The Z and R components record Rayleigh waves whereas SH waves are recorded on the T component. The signal on the transverse component becomes stronger at higher source-receiver azimuth.

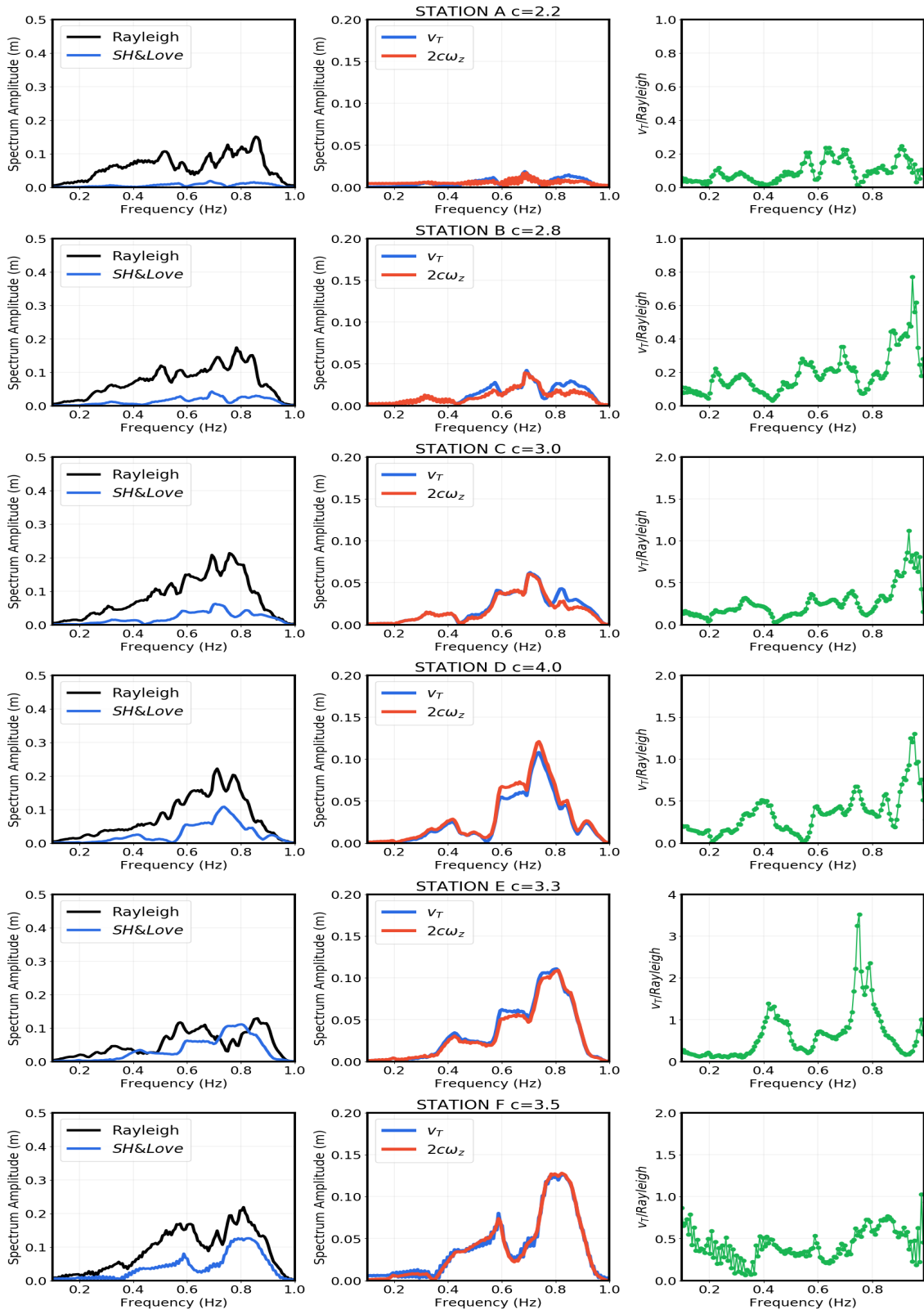


Figure 4.25 – Rayleigh vs SH/Love wave amplitude spectrum adjacent to vertical rotational rate $\times 2c$ (c : fundamental Love wave velocity from 1-D synthetics) vs transverse velocity as a function of frequency for stations A, B, C, D, E & F for model with 6 km ocean, 3 km sediments, 6 km crust and 7 km mantle (figure 3.24) with source close to the ocean-continental boundary. Rayleigh wave amplitude is higher than SH wave amplitude at all stations. The far stations have relatively higher SH wave amplitude than the close stations. The similarity between the vertical rotational rate and transverse velocity indicates Love wave propagation at all frequencies. The L/R amplitude ratio at all frequencies are also plotted.

Models			
Model number	Oceanic side	Continental side	Ocean-continent slope angle
Model I	1 km ocean, 16 km crust	17 km crust	32°
Model II	1 km ocean, 6 km crust, 10 km mantle	7 km crust, 10 km mantle	32°
Model III	3 km ocean, 6 km crust, 10 km mantle	9 km crust, 10 km mantle	32°
Model IV	6 km ocean, 6 km crust, 10 km mantle	12 km crust, 10 km mantle	32°
Model V	6 km ocean, 3 km sediments, 6 km crust, 7 km mantle	15 km crust, 7 km mantle	32°
Model VI	3 km ocean, 6 km crust, 10 km mantle	9 km crust, 10 km mantle	10°

Table 4.3 – Different 3D model configurations used in this study to model the effect of ocean-continent slope on the transverse energy using both a source close and far from the ocean-continent boundary.

amplitude on energy can explain the high L/R amplitude ratio.

4.3 Effect of the ocean-continent slope

Till now, we investigated the effect of the ocean thickness and the presence of sediment on the Love wave generation. Here we analyze the effect of the ocean continent slope. We modify model III by changing the angle of the ocean continent slope to 10°. Our model constitute of three layers: 3 km ocean , 6 km crust and 10 km mantle in the oceanic side and two layers of 9 km crust and 10 km mantle on the continental side. The mesh volume is same as in model III. T component seismic wave field for close source and far source is discussed in the following section.

4.3.1 Seismic wavefield for model VI (3 km ocean, crust, mantle) slope 10°

The Z, R, T components of the seismic wave field computed for a source close to the ocean-continent boundary is represented in figure 4.28. We record weaker signal on the T component as compared to bigger slope. Figure 4.29 and 4.30 show the amplitude spectra for source close and far, respectively. We observe that the amplitude on the transverse component is close to 0 for station A and increases but is still weak for station F. Higher amplitude is observed for source S1 than in source S2 for $f > 0.6$ Hz.

The two waveforms $2c\omega_Z$ and v_T show maximum fit at station F for both sources. The maximum L/R ratio obtained for close source is 0.625 at 0.75 Hz and 0.76 for far source. The reduction in the slope angle (from 32° to 10°) of the ocean-continent boundary show ($\approx 50\%$) decrease in the L/R amplitude ratio.

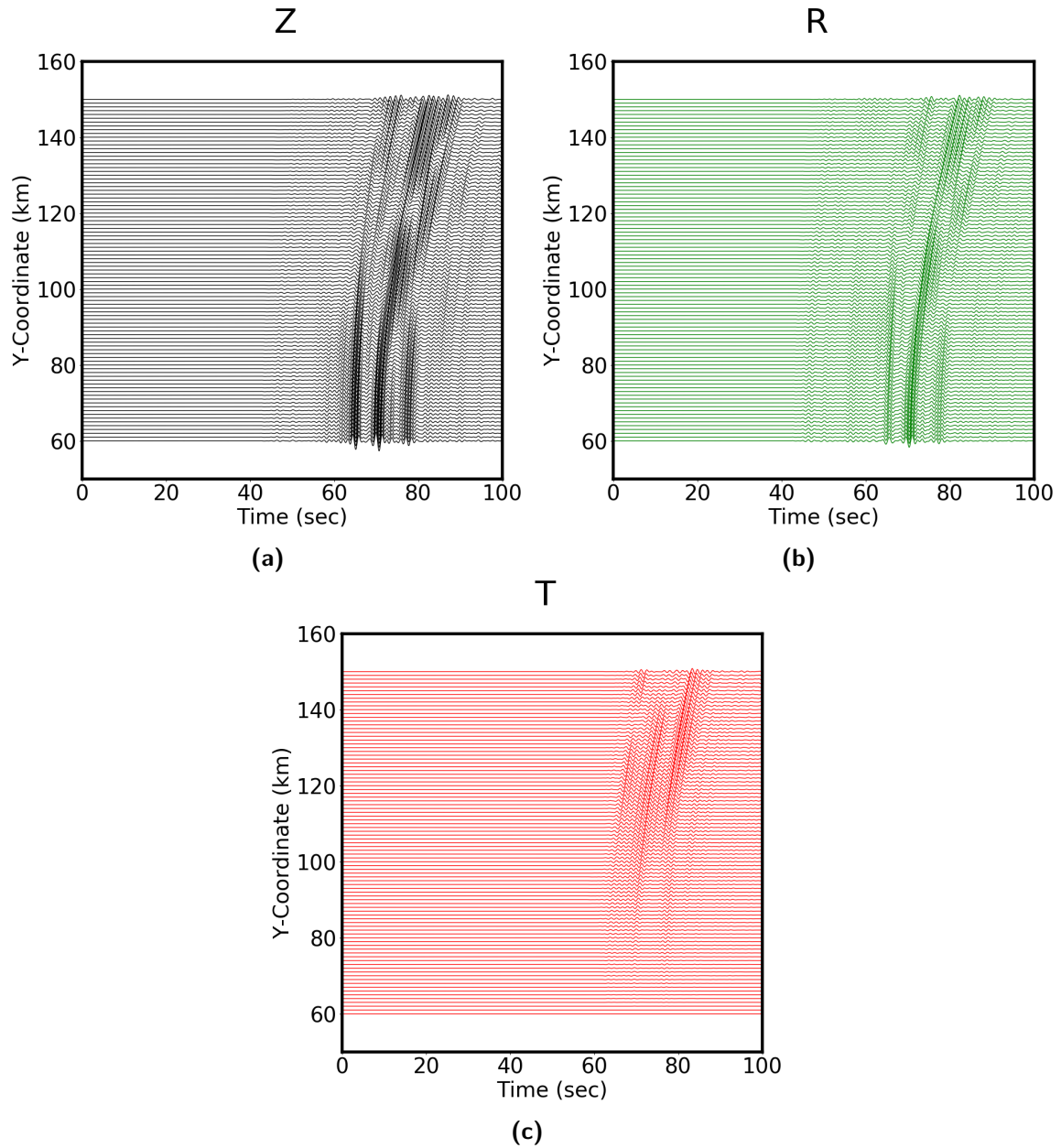


Figure 4.26 – Synthetic seismic velocity as a function of the stations y-coordinate for the a) vertical (Z), b) radial (R) and c) transverse (T) components. Seismograms are computed for model V (6 km ocean, 3 km sediments with mantle) and Source1 far from the ocean-continent boundary is injected. The Z and R components record Rayleigh waves whereas SH waves are recorded on the T component. The signal on the transverse component becomes stronger at higher source-receiver azimuth.

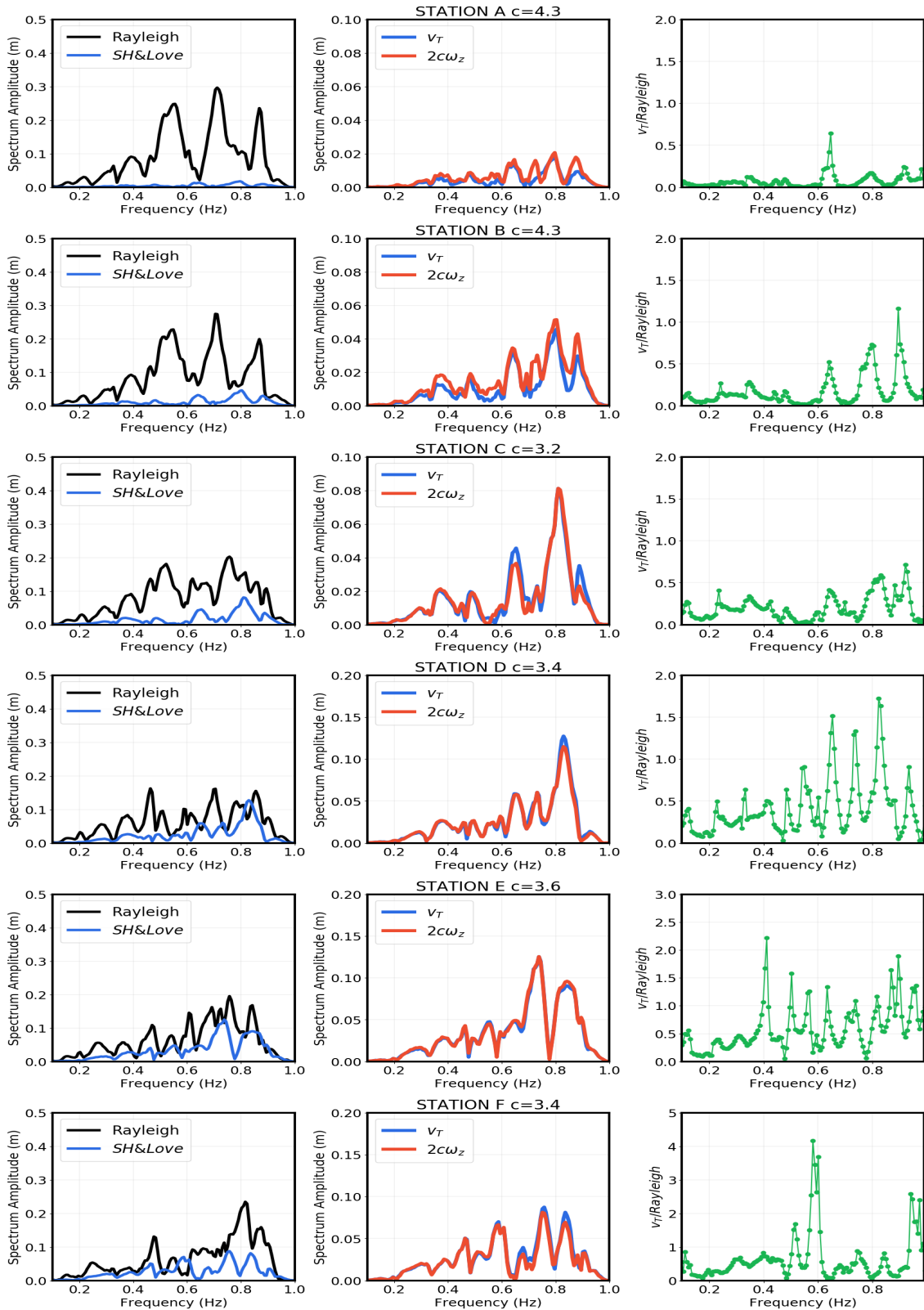


Figure 4.27 – Rayleigh vs SH/Love wave amplitude spectrum adjacent to vertical rotational rate $\times 2c$ (c : fundamental Love wave velocity from 1-D synthetics) vs transverse velocity as a function of frequency for stations A, B, C, D, E & F for model with 6 km ocean, 3 km sediments, 6 km crust and 7 km mantle (figure 3.24) with source far-away from the ocean-continental boundary. Rayleigh wave amplitude is higher than SH wave amplitude at all stations. The far stations have relatively higher SH wave amplitude than the close stations. The similarity between the vertical rotational rate and transverse velocity indicates Love wave propagation at all frequencies. The L/R amplitude ratio at all frequencies are also plotted.

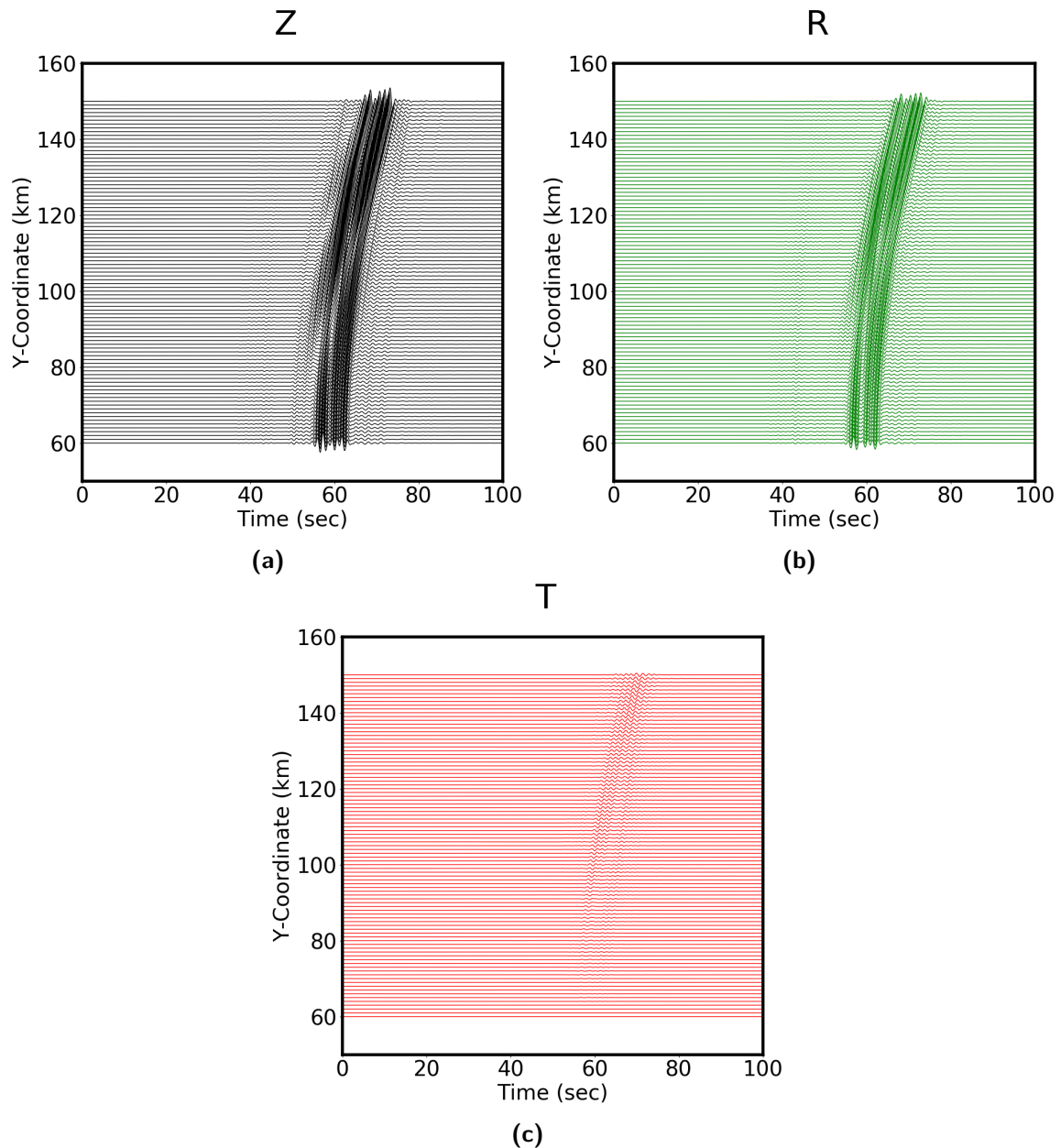


Figure 4.28 – Synthetic seismic velocity as a function of the stations y-coordinate for the a) vertical (Z), b) radial (R) and c) transverse (T) components. Seismograms are computed for model with 3 km ocean, 6 km crust, 10 km mantle with the slope making an angle of 10° with the horizontal and Source2 (i.e., located close to the ocean-continent boundary) injected. The Z and R components record Rayleigh waves whereas SH waves are recorded on the T component. The signal on the transverse component becomes stronger at higher source-receiver azimuth.

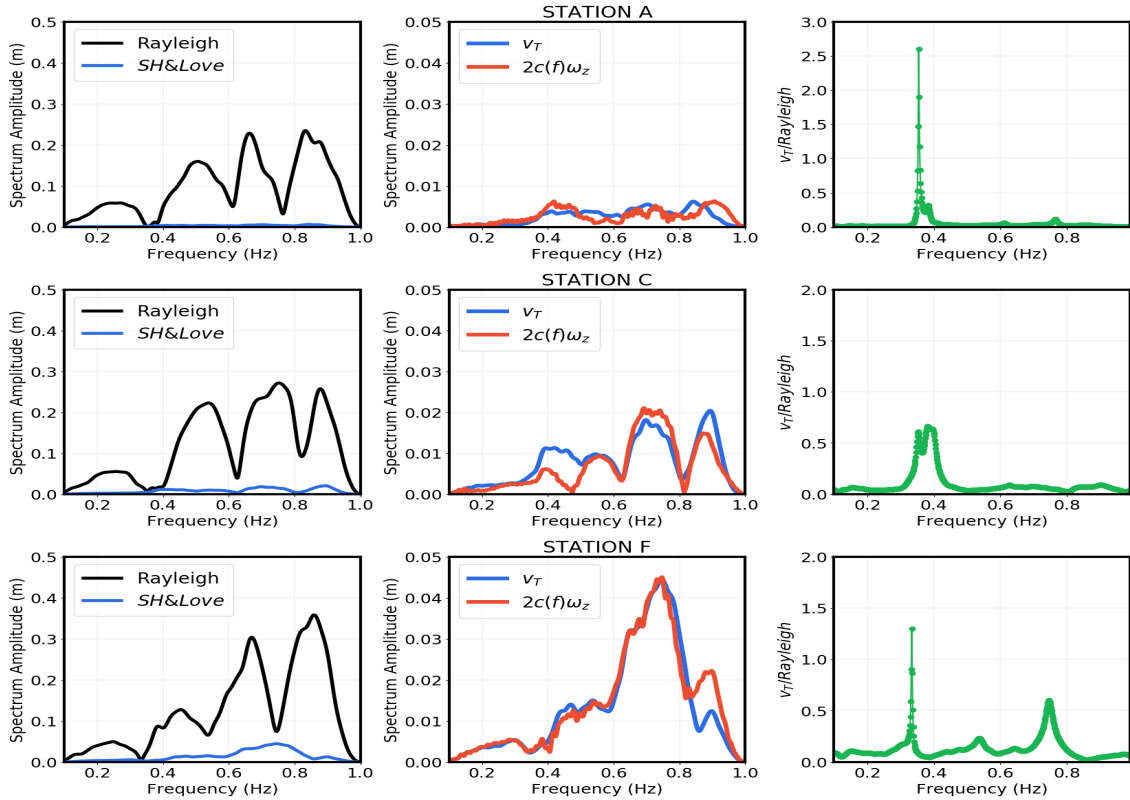


Figure 4.29 – Rayleigh vs SH/Love wave amplitude spectrum adjacent to vertical rotational rate $\ast 2c$ (c : fundamental Love wave velocity from 1-D synthetics) vs transverse velocity as a function of frequency for stations A, B, C, D, E & F in 3 km ocean model, slope 10° when the source is placed close to the boundary. Rayleigh wave amplitude is higher than SH wave amplitude at all stations. The far stations have relatively higher SH wave amplitude than the close stations. The similarity between ω_z and v_T at certain frequencies indicate Love wave generation. The L/R amplitude ratio at all frequencies are also plotted.

4.4 Results summary

In this chapter, we have proven that Love waves can be generated at the ocean continent boundary. For different models listed in Table 4.3, we estimated Rayleigh to Love conversion and found that L/R ratio varies between 0.1-3.5 for source close to the boundary and between 0.1-4.2 for far source. Here we summarize our results of the above analysis. A detailed comparison of the effect of ocean thickness, sediments and slope angle on the seismic wave field is shown to determine the model parameters that enable to obtain the largest L/R ratio. Since these multiple effects have strong frequency dependence: the effect has a maximum at some frequency and diminishes/increases at lower and higher frequencies depending on the model. Hence, it is complicated to derive one conclusion for all frequencies. We therefore present in the different frequency bands.

Effect of ocean thickness in the frequency band 0.1-0.3 Hz

In figure 4.31, we first compare the Rayleigh wave (left) and Love wave (right) spectrum at one station (station E) for both sources. Figure 4.32 shows the zoomed Rayleigh and Love wave spectra at station E in the frequency 0.1-0.3 Hz. For a close source, the Rayleigh wave amplitude in model III (3 km ocean) is higher than in model II (1 km ocean) and

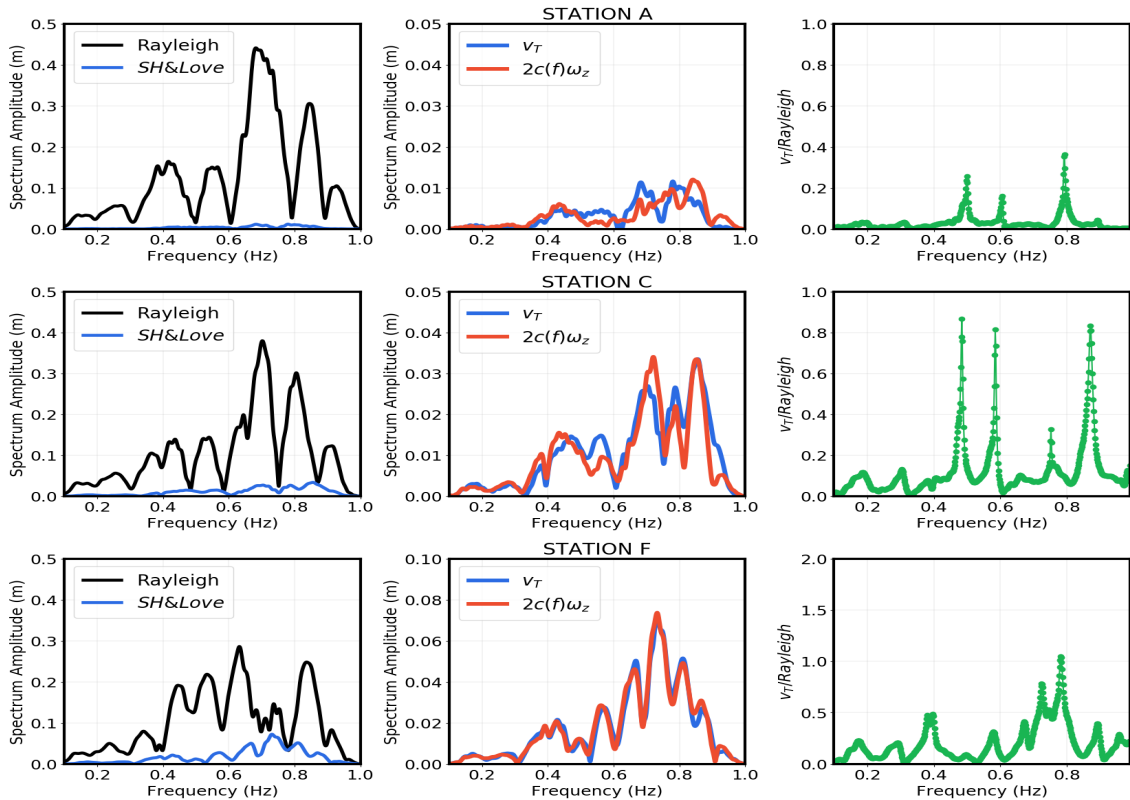


Figure 4.30 – Rayleigh vs SH/Love wave amplitude spectrum adjacent to vertical rotational rate $\ast 2c$ (c : fundamental Love wave velocity from 1-D synthetics) vs transverse velocity as a function of frequency for stations A, B, C, D, E & F in 3 km ocean model, slope 10° when the source is placed far from the boundary. Rayleigh wave amplitude is higher than SH wave amplitude at all stations. The far stations have relatively higher SH wave amplitude than the close stations. The similarity between ω_z and v_T at certain frequencies indicate Love wave generation. The L/R amplitude ratio at all frequencies are also plotted.

IV (6 km ocean) which have similar amplitudes at frequencies below 0.2 Hz (figure 4.32a). Above 0.2 Hz, the effect of increased ocean thickness lead to decrease in Rayleigh wave amplitude. Similar effects are observed in case of far source (Figure 4.31 bottom left), the Rayleigh wave amplitude is highest for model III at frequencies below 0.2 Hz (4.32c. Above 0.2 Hz, it decreases with increasing ocean thickness. On comparing the Love waves spectra for models with different ocean thickness (figure 4.32b), the Love wave amplitude increases for increasing ocean thickness i.e., model IV has higher amplitude than model II and III in case of close source, whereas model III and IV have similar amplitudes for far source which is higher than in model II.

Effect of ocean thickness in the frequency band 0.3-0.7 Hz

At 0.3 Hz $<f < 0.7$ Hz, the ocean thickness has a similar effect on the Rayleigh wave amplitude for both sources (figure 4.31 left). It continues to decrease with increasing ocean thickness. The maximum is obtained for model II (maximum value 0.25 m in case of close source and 0.48 m for far source). Specifically, many peaks are evident in the Rayleigh wave spectra for all the models in case of far source. The Love wave amplitude for close source (figure 4.31 top right) is similar for model II and III whereas it decreases for model IV. In case of far source, thicker oceans have higher Love wave amplitude.

Effect of ocean thickness in the frequency band 0.7-1 Hz

For frequencies above 0.7 Hz, model III has the maximum Rayleigh wave amplitude (0.45 m) followed by model II (0.35 m) and then model IV (0.22 m) (figure 4.31 top left). For far source, the highest amplitude for model III is 0.65 m followed by model II (0.47 m) and then model IV (0.3 m) (figure 4.31 bottom left). The Love wave amplitude in this frequency band has an inverse relation with the ocean thickness.

Effect of ocean-continent slope angle in the frequency band 0.1-1 Hz

We compare the Rayleigh wave and Love wave amplitude for models with same ocean thickness but different slopes. Model III (slope 32°) has higher amplitude than model VI (slope 10°) at all frequencies irrespective of source position.

Effect of sediments in the frequency band 0.1-1 Hz

For most frequencies, the Rayleigh wave amplitude is lower in model with sediments (model V) than model without sediments (model IV) for both sources. On analyzing Love wave amplitude at $f < 0.7$ Hz, model IV and V have similar amplitudes for close source, whereas model V has lower amplitude than model IV. The Love wave amplitude increases due to sediments for frequencies above 0.7 Hz.

L/R amplitude ratio in the frequency band 0.1-1 Hz

Figure 4.33a and 4.33b shows the L/R ratio as a function of frequency for all the models (without sediments) at station E for source at the ocean-continental boundary and source far-away from the boundary, respectively. In the left figure, for $f < 0.35$ Hz, we observe the highest ratio of 0.75 for model with thickest ocean, in our case model IV (6 km ocean). The ratio decreases with decreasing ocean thickness i.e, model III (3 km ocean) has the second highest ratio and model II (1 km ocean) the third. On comparing the models with same ocean thickness (3 km ocean) but with different slopes of ocean-continent boundary (32° & 10°), L/R ratio is greater for bigger slope than the smaller slope. For $0.35 \text{ Hz} < f < 0.65 \text{ Hz}$, model III (3 km ocean) has the highest ratio. Model IV and model II gives the same amplitude ratio which is lower than model III. For $f > 0.65$ Hz, we observed model II has highest L/R ratio followed by model IV and then model III . Even at higher frequencies, model with smaller slope has the smallest L/R ratio.

When the source is far away (figure 4.33b), for $f < 0.35$ Hz, we observe similar pattern: the ratio decreases with decreasing ocean thickness. For $f > 0.35$ Hz, except at peak frequencies, the highest ratio is obtained for model IV (6 km ocean), followed by model III (3 km ocean) and model II (1 km ocean). The lowest ratio is observed for model VI(3 km ocean and slope 10°).

We also note that we observe many L/R peaks in case of source far-away from the boundary than closer to it. For $f < 0.35$ Hz, the peaks are observed due to the small amplitude of Rayleigh and Love waves as seen in figure 4.31. For $f > 0.35$ Hz, the maximas are observed at frequencies corresponding to the minimas of Rayleigh wave spectrum. On an average, higher L/R ratio is obtained for close source than far-source at lower frequencies and vice-versa for higher frequencies.

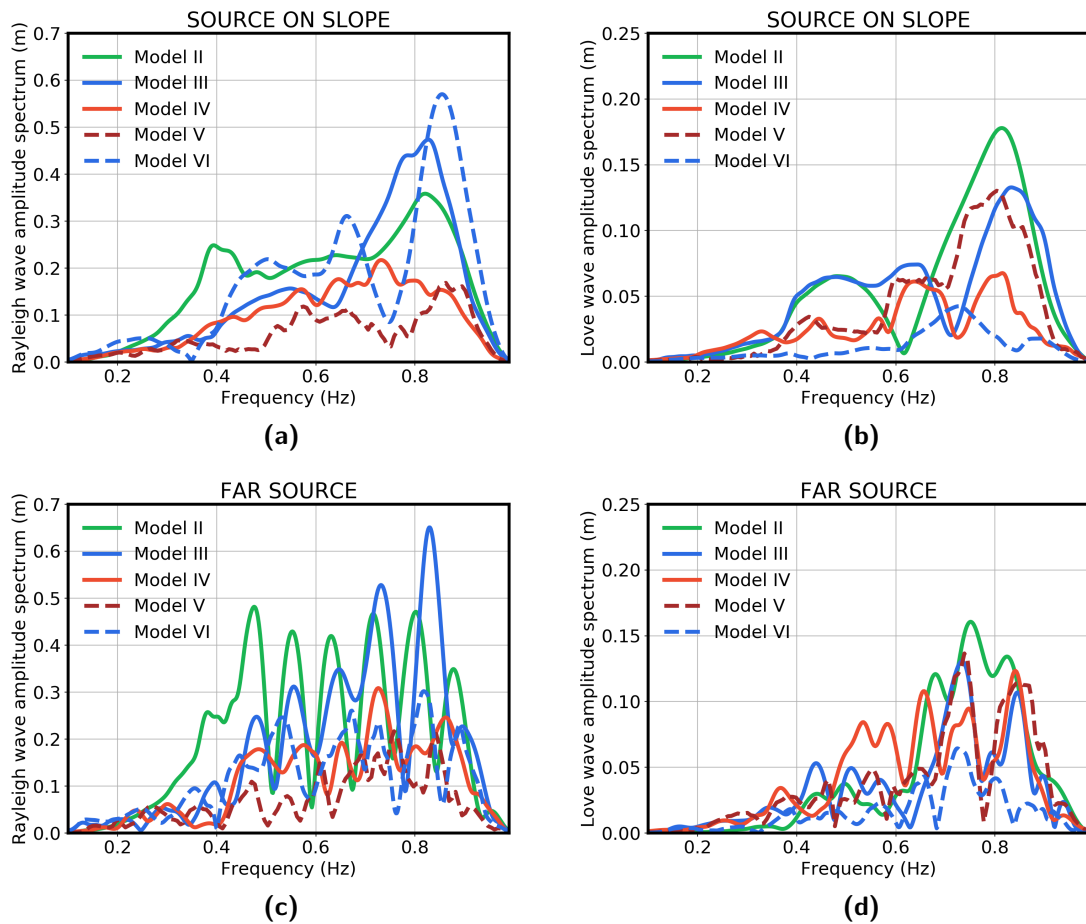


Figure 4.31 – Top: Rayleigh and Love wave amplitude as a function of frequency at station E obtained for source close to the ocean-continental boundary in the frequency band 0.1-1 Hz are shown in a) & b) respectively. Bottom: Similarly for source far-away from the boundary shown in c) & d) respectively. As the ocean thickness increases, Rayleigh wave amplitude decreases for both sources whereas the Love wave amplitude decreases for source close to the boundary and increases for far source.

In figure 4.33c and 4.33d, we estimate the effect of sediment and compare the L/R ratio at station E for model IV (without sediments) and model V (with sediments) for source at the ocean-continental boundary and source far-away from it, respectively. For $f < 0.35$ Hz, we obtain higher ratio for model IV than model V for close source whereas similar ratios are obtained for far source. At $f > 0.35$ Hz, model V generates higher L/R ratio than model IV for both sources. However, many peaks are observed for far-source. Between the two source locations, higher ratios are observed for close source than the far-source. From this study, we conclude that the model with sediments causes maximum excitation of Love waves irrespective of the source location.

Therefore, in addition to providing a measure of the frequency-dependence of L/R amplitude ratio, the effect of ocean-continental slope is useful for studying the physics behind conversion of incident wave energy from secondary microseisms into Rayleigh and Love waves.

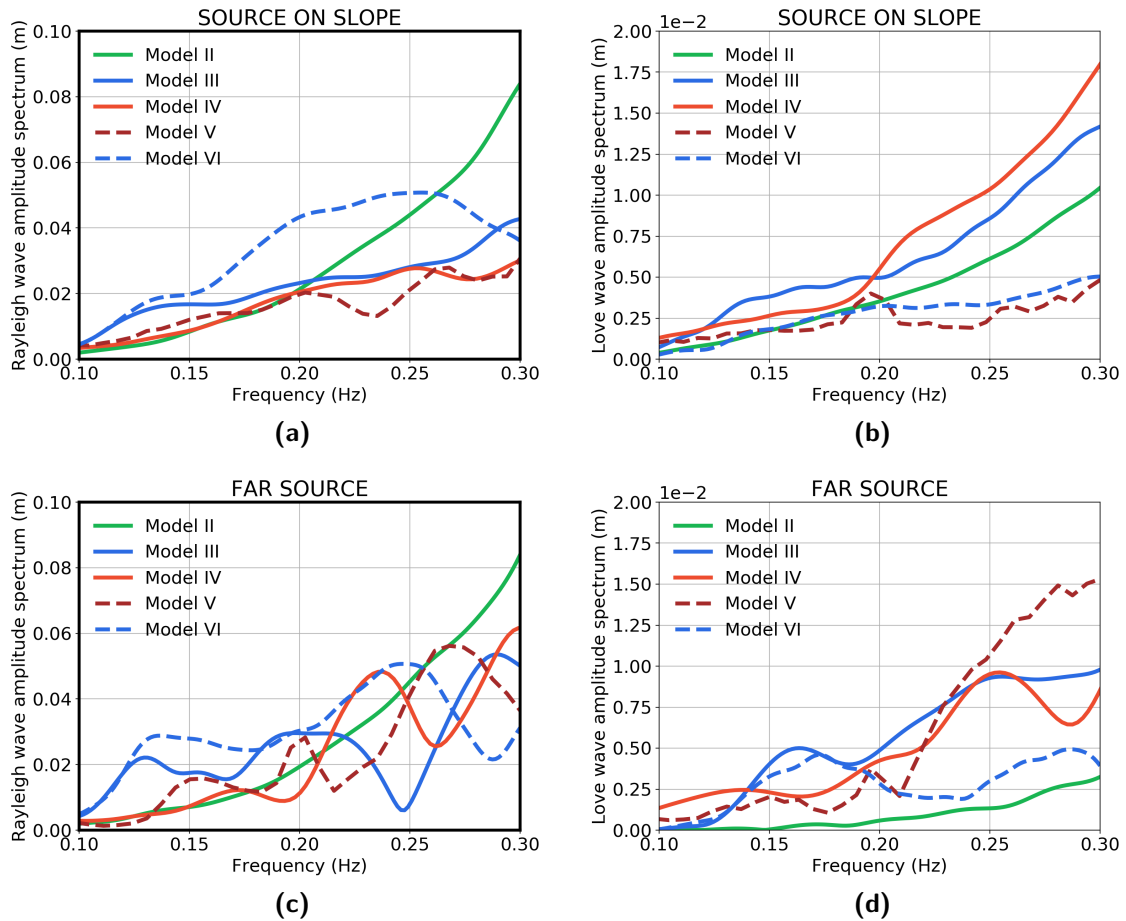


Figure 4.32 – Top: Rayleigh and Love wave amplitude as a function of frequency at station E obtained for source close to the ocean-continental boundary in the frequency band 0.1-0.3 Hz are shown in a) & b) respectively. Bottom: Similarly for source far-away from the boundary shown in c) & d) respectively. In this narrow frequency band, Rayleigh wave amplitude decreases with increasing ocean thickness for source close and have similar amplitudes for far source. The Love wave amplitude is higher in models with thicker oceans for source close and far from the boundary.

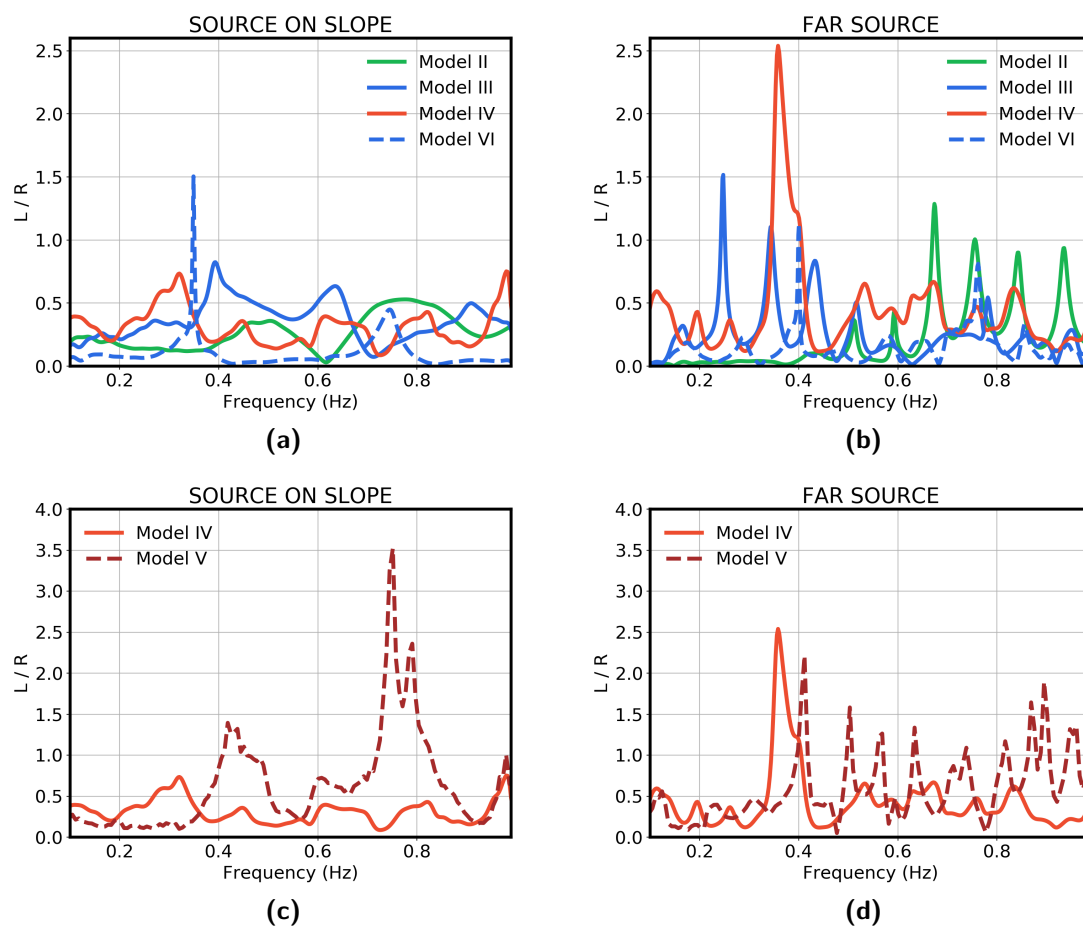


Figure 4.33 – Comparison of L/R ratio at station E (a,b) for all the models without sediments (model II: 1 km ocean, slope 32° ; model III: 3 km ocean, slope 32° ; model IV: 6 km ocean, slope 32° ; model VI : 3 km ocean, slope 10°) where (a) is for source at the ocean-continental boundary and (b) source far-away from the ocean-continental boundary. (c,d) for models with and without sediments (model IV: 6 km ocean, slope 32° , model V: 6 km ocean, 3 km sediments, slope 32°) where (c) is for source at the ocean-continental boundary and (d) source far-away from the ocean-continental boundary.

Chapter 5

Conclusion and future perspectives

In this thesis, we have modeled the effect of ocean-continental slope on the secondary microseism wave field and discussed several factors that affect the seismic wave amplitude and eventually, the L/R amplitude ratio. We present briefly the theory of secondary microseisms that explains how seismic noise can be generated in the ocean. It is due to the non-linear interaction of two oppositely traversing waves that generates secondary microseisms. A detailed discussion of the structure of spectral element method and its implementation is shown which allowed us to numerically model the seismic wave field propagation in 3D media.

A short example utilizing the data acquired by a seismic network to show the propagation of different surface waves using the beamforming technique is illustrated. We observed the propagation of not only Rayleigh waves in the data but also Love waves propagating at higher velocity than the Rayleigh waves at frequency 0.125 Hz.

Some insights on the different modes of Rayleigh and Love wave that can propagate in 1 D Earth models are provided. We show that on increasing the ocean thickness, the possibility of interference of fundamental mode and higher overtones increases and by computing the synthetic seismograms, we show the modulation of shape and amplitude of different modes of the wave field and similarly for continental models. Including the sediments further enhance the interference from the higher modes and as a result even more complex wave form is observed. The analysis is useful for interpreting the complex seismic wave field recorded in a 3D medium.

Because the noise sources originate in the ocean, the excitation of Love waves seemed impossible. Therefore, one of the factors we investigated in this thesis that may contribute to the Love wave excitation is the effect of ocean-continental slope boundary. We confirm that Love waves can be generated due to the boundary. The conversion of incident energy into Love wave energy is higher at large source-receiver distances and greater azimuths. The relative amplitude of Rayleigh and Love waves recorded on the vertical and horizontal components respectively, are analyzed as a result of the influence from different parameters: the increasing ocean thickness, source location close to the boundary and far from the boundary, the smaller ocean-continent slope angle and the presence of sediments.

Noise sources are generated beneath the surface of shallow and deep oceans, therefore bathymetry (ocean thickness) is an important parameter to investigate as it also modulates the noise amplitude differently, as illustrated in 1D modeling. In 3D, we show that when the P waves from the secondary microseism travel through the ocean, they are converted to P and S waves at the crust and mantle layer. All these waves then interact with the ocean-continental boundary and Love waves are generated and recorded on the transverse component. Considering Rayleigh waves, we observe the following for both source close and far from the boundary.

- 1) In general, we observe lower amplitude of Rayleigh waves generated in thicker oceans.
- 2) In a 3 km ocean model, Rayleigh wave amplitude is lower than in 1 km ocean model at $f < 0.7$ Hz and higher at $f > 0.7$ Hz.
- 3) And, the Rayleigh wave amplitude for a 6 km deep ocean is lower than in a 3 km ocean at most frequencies.
- 4) For similar ocean thickness, the influence of source-site on the amplitude and frequency content of seismic wave field shows that at resonant frequencies in the ocean, higher amplitude Rayleigh waves are recorded on the continent for source offshore than source close to the boundary. At other frequencies, source close to the boundary generates higher amplitude Rayleigh waves.

For the Love wave amplitude:

- 1) It decreases with increasing ocean thickness only when the source is close to the ocean-continental boundary. For far source, the Love wave amplitude increases at frequencies below 0.7 Hz and vice-versa at higher frequencies.
- 2) The source-site has a similar effect on the Love wave amplitude. At resonant frequencies in the ocean, it is higher when the source is far from the coast than close to the boundary. At other frequencies, source close to the boundary generates higher amplitude Love waves. Therefore shallow ocean with source close to the boundary have the highest Love wave amplitude.

As a consequence, the resulting L/R amplitude ratios:

- 1) They are lower in thicker oceans than in shallow ocean for source close to the boundary and higher for source far from the coast.
- 2) Except at resonant frequencies, higher ratios are observed for close source than for source offshore in similar oceans.

Therefore we conclude that shallow ocean with source close to the boundary generates the highest L/R amplitude ratio.

Adding sedimentary layer between the ocean and crust in a 6 km ocean model diminishes the Rayleigh wave amplitude irrespective of source site whereas Love wave amplitude is amplified at most frequencies for close source and only at higher frequencies for source far from the boundary. This leads to higher L/R amplitude ratios for both sources than in model without sediments.

The reduction of slope angle by 70 % increases the Rayleigh wave amplitude and diminishes the Love wave amplitude for close source whereas both the amplitudes are reduced for far source. The resulting L/R amplitude ratios are lower for small slope.

Perspectives In this thesis, we have shown that the amplitude of Rayleigh and Love wave is different for varying ocean thickness and the source location as different modes are

excited and their amplification is distance dependent. However, the L/R amplitude ratios obtained are lower than the field observations except some higher ratios were obtained due to presence of sediments. In reality, the Earth is more complex and our models are comprised of homogeneous layers. For future investigations, a heterogeneous model with a realistic Earth profile can be adapted to simulate seismic wave field using spectral element method to measure its effect along with the ocean-continental slope boundary on the seismic noise amplitude. For our study, we simulated the seismic wave field from secondary microseisms using a single source, however the study can be extended by using multiple sources acting on the sea floor. Many other field observations have also reported the excitation of Love waves in the frequency band of primary microseisms which is not addressed in this thesis. We can use the similar methods to understand the underlying mechanism and model the L/R amplitude ratios for primary microseisms.

Bibliography

PhD thesis.

- Ardhuin, F., Gualtieri, L., and Stutzmann, E. (2015). How ocean waves rock the earth: Two mechanisms explain microseisms with periods 3 to 300 s. *Geophysical Research Letters*, 42(3):765–772.
- Ardhuin, F., Stutzmann, E., Schimmel, M., and Mangeney, A. (2011). Ocean wave sources of seismic noise. *Journal of Geophysical Research: Oceans*, 116(9):1–21.
- Backus, M., Burg, J., Baldwin, D., and Bryan, E. (1964). Wide-band extraction of mantle p waves from ambient noise. *Geophysics*, 29(5):672–692.
- Bernard, P. and Martel, L. (1990). A possible origin of 26 s microseisms. *Physics of the Earth and Planetary Interiors*, 63(3-4):229–231.
- Bromirski, P. D. (2002). The near-coastal microseism spectrum: Spatial and temporal wave climate relationships. *Journal of Geophysical Research*, 107(B8):1–20.
- Bromirski, P. D. (2009). Earth vibrations. *Science*, 324(5930):1026–1027.
- Capon, J. (1973). Analysis of microseismic noise at lasa, norsar and alpa. *Geophysical Journal International*, 35(1-3):39–54.
- Chaljub, E., Komatitsch, D., Vilotte, J.-P., Capdeville, Y., Valette, B., and Festa, G. (2007). Spectral-element analysis in seismology. *Advances in geophysics*, 48:365–419.
- Cupillard, P., Delavaud, E., Burgos, G., Festa, G., Vilotte, J.-P., Capdeville, Y., and Montagner, J.-P. (2012). Regsem: a versatile code based on the spectral element method to compute seismic wave propagation at the regional scale. *Geophysical Journal International*, 188(3):1203–1220.
- Faccioli, E., Maggio, F., Paolucci, R., and Quarteroni, A. (1997). 2d and 3d elastic wave propagation by a pseudo-spectral domain decomposition method. *Journal of seismology*, 1(3):237–251.
- Friedrich, A., Krueger, F., and Klinge, K. (1998). Ocean-generated microseismic noise located with the gräfenberg array. *Journal of Seismology*, 2(1):47–64.
- Fukao, Y., Nishida, K., and Kobayashi, N. (2010). Seafloor topography, ocean infragravity waves, and background love and rayleigh waves. *Journal of Geophysical Research: Solid Earth*, 115(B4).

- Gal, M. (2017). Journal of Geophysical Research : Solid Earth Full wavefield decomposition of high-frequency secondary microseisms reveals distinct arrival azimuths for Rayleigh and Love waves. pages 4660–4675.
- Gal, M., Reading, A. M., Ellingsen, S. P., Koper, K. D., Burlacu, R., and Gibbons, S. J. (2016). Deconvolution enhanced direction of arrival estimation using one- and three-component seismic arrays applied to ocean induced microseisms. *Geophysical Journal International*, 206(1):345–359.
- Gerstoft, P., Shearer, P. M., Harmon, N., and Zhang, J. (2008). Global p, pp, and pkp wave microseisms observed from distant storms. *Geophysical Research Letters*, 35(23).
- Gerstoft, P. and Tanimoto, T. (2007). A year of microseisms in southern California. *Geophysical Research Letters*, 34(20):1–6.
- Gutenberg, B. (1931). Microseisms in north america. *Bulletin of the Seismological Society of America*, 21(1):1–24.
- Gutenberg, B. (1958). Microseisms. In *Advances in Geophysics*, volume 5, pages 53–92. Elsevier.
- Hadziioannou, C., Gaebler, P., Schreiber, U., Wassermann, J., and Igel, H. (2012). Examining ambient noise using colocated measurements of rotational and translational motion. *Journal of seismology*, 16(4):787–796.
- Hasselmann, K. (1963). A statistical analysis of the generation of microseisms. *Reviews of Geophysics*, 1(2):177–210.
- Haubrich, R., Munk, W., and Snodgrass, F. (1963). Comparative spectra of microseisms and swell. *Bulletin of the Seismological Society of America*, 53(1):27–37.
- Haubrich, R. A. and McCamy, K. (1969). Microseisms: Coastal and pelagic sources. *Reviews of Geophysics*, 7(3):539–571.
- Herrmann, R. Computer programs in earthquake seismology. volume 2: Surface wave program.
- Kedar, S., Longuet-Higgins, M., Webb, F., Graham, N., Clayton, R., and Jones, C. (2008). The origin of deep ocean microseisms in the North Atlantic Ocean. *Proceedings of the Royal Society A: Mathematical, Physical and Engineering Sciences*, 464(2091):777–793.
- Kobayashi, N. and Nishida, K. (1998). Continuous excitation of planetary free oscillations by atmospheric disturbances. *Nature*, 395(6700):357.
- Komatitsch, D., Barnes, C., and Tromp, J. (2000). Wave propagation near a fluid-solid interface: A spectral-element approach. *Geophysics*, 65(2):623–631.
- Komatitsch, D. and Tromp, J. (1999). Introduction to the spectral element method for three-dimensional seismic wave propagation. *Geophysical journal international*, 139(3):806–822.

- Komatitsch, D. and Vilotte, J.-P. (1998). The spectral element method: an efficient tool to simulate the seismic response of 2d and 3d geological structures. *Bulletin of the seismological society of America*, 88(2):368–392.
- Koper, K. D., de Foy, B., and Benz, H. (2009). Composition and variation of noise recorded at the yellowknife seismic array, 1991–2007. *Journal of Geophysical Research: Solid Earth*, 114(B10).
- Longuet-Higgins, M. S. (1950). A theory of the origin of microseisms. *Philosophical Transactions of the Royal Society of London. Series A, Mathematical and Physical Sciences*, 243(857):1–35.
- Meschede, M., Stutzmann, É., Farra, V., Schimmel, M., and Arduin, F. (2017). The Effect of Water Column Resonance on the Spectra of Secondary Microseism P Waves. *Journal of Geophysical Research: Solid Earth*, 122(10):8121–8142.
- Miche, M. (1944). Mouvements ondulatoires de la mer en profondeur constante ou décroissante. *Annales de Ponts et Chaussées, 1944, pp (1) 26-78, (2) 270-292, (3) 369-406*.
- Nawa, K., Suda, N., Fukao, Y., Sato, T., Aoyama, Y., and Shibuya, K. (1998). Incessant excitation of the earth’s free oscillations. *Earth, planets and space*, 50(1):3–8.
- Nishida, K. (2013). Earth’s background free oscillations. *Annual Review of Earth and Planetary Sciences*, 41.
- Nishida, K. (2014). Source spectra of seismic hum. *Geophysical Journal International*, 199(1):416–429.
- Nishida, K., Kawakatsu, H., Fukao, Y., and Obara, K. (2008a). Background Love and Rayleigh waves simultaneously generated at the Pacific Ocean floors. *Geophysical Research Letters*, 35(16):1–5.
- Nishida, K., Kawakatsu, H., Fukao, Y., and Obara, K. (2008b). Background love and rayleigh waves simultaneously generated at the pacific ocean floors. *Geophysical Research Letters*, 35(16).
- Nishida, K., Montagner, J.-P., and Kawakatsu, H. (2009). Global surface wave tomography using seismic hum. *Science*, 326(5949):112–112.
- Obrebski, M., Arduin, F., Stutzmann, E., and Schimmel, M. (2013). Detection of microseismic compressional (p) body waves aided by numerical modeling of oceanic noise sources. *Journal of Geophysical Research: Solid Earth*, 118(8):4312–4324.
- Ramirez, J. E. (1940). An experimental investigation of the nature and origin of microseisms at st. louis, missouri: part one. *Bulletin of the Seismological Society of America*, 30(1):35–84.
- Rhie, J. and Romanowicz, B. (2004). Excitation of earth’s continuous free oscillations by atmosphere–ocean–seafloor coupling. *Nature*, 431(7008):552.

- Rost, S. and Thomas, C. (2002). Array seismology: Methods and applications. *Reviews of Geophysics*, 40(3).
- Sato, H., Fehler, M. C., and Maeda, T. (2012). *Seismic wave propagation and scattering in the heterogeneous earth*, volume 496. Springer.
- Schimmel, M. and Gallart, J. (2007). Frequency-dependent phase coherence for noise suppression in seismic array data. *Journal of Geophysical Research: Solid Earth*, 112(B4).
- Schimmel, M. and Paulssen, H. (1997). Noise reduction and detection of weak, coherent signals through phase-weighted stacks. *Geophysical Journal International*, 130(2):497–505.
- Schimmel, M., Stutzmann, E., and Gallart, J. (2011). Using instantaneous phase coherence for signal extraction from ambient noise data at a local to a global scale. *Geophysical Journal International*, 184(1):494–506.
- Scholte, J. (1943). Ouer het verband tussen zeegolven en microseismen: I. *Proceedings of the Section of Sciences/Koninklijke Nederlandsche Akademie van Wetenschappen*, 52:669–683.
- Seriff, A., Velzeboer, C., and Haase, R. (1965). Possible p-wave observations in short-period seismic noise. *Geophysics*, 30(6):1187–1190.
- Shapiro, N. M., Campillo, M., Stehly, L., and Ritzwoller, M. H. (2005). High-resolution surface-wave tomography from ambient seismic noise. *Science*, 307(5715):1615–1618.
- Stutzmann, E., Roult, G., and Astiz, L. (2000). Geoscope station noise levels. *Bulletin of the Seismological Society of America*, 90(3):690–701.
- Suda, N., Nawa, K., and Fukao, Y. (1998). Earth’s background free oscillations. *Science*, 279(5359):2089–2091.
- Tanimoto, T., Hadziioannou, C., Igel, H., Wasserman, J., Schreiber, U., and Gebauer, A. (2015a). Estimate of rayleigh-to-love wave ratio in the secondary microseism by colocated ring laser and seismograph. *Geophysical Research Letters*, 42(8):2650–2655.
- Tanimoto, T., Hadziioannou, C., Igel, H., Wasserman, J., Schreiber, U., and Gebauer, A. (2015b). Estimate of Rayleigh-to-Love wave ratio in the secondary microseism by colocated ring laser and seismograph. pages 2650–2655.
- Tanimoto, T., Um, J., Nishida, K., and Kobayashi, N. (1998). Earth’s continuous oscillations observed on seismically quiet days. *Geophysical Research Letters*, 25(10):1553–1556.
- Toksöz, M. N. and Lacoss, R. T. (1968). Microseisms: Mode structure and sources. *Science*, 159(3817):872–873.
- Webb, S. C. (1998). Broadband seismology and noise under the ocean. *Reviews of Geophysics*, 36(1):105–142.

Zhang, J., Gerstoft, P., and Shearer, P. M. (2009). High-frequency p-wave seismic noise driven by ocean winds. *Geophysical Research Letters*, 36(9).

Ziane, D. and Hadziioannou, C. (2019). The contribution of multiple scattering to love wave generation in the secondary microseism. *Geophysical Journal International*, 217(2):1108–1122.